



저작자표시-비영리-변경금지 2.0 대한민국

이용자는 아래의 조건을 따르는 경우에 한하여 자유롭게

- 이 저작물을 복제, 배포, 전송, 전시, 공연 및 방송할 수 있습니다.

다음과 같은 조건을 따라야 합니다:



저작자표시. 귀하는 원저작자를 표시하여야 합니다.



비영리. 귀하는 이 저작물을 영리 목적으로 이용할 수 없습니다.



변경금지. 귀하는 이 저작물을 개작, 변형 또는 가공할 수 없습니다.

- 귀하는, 이 저작물의 재이용이나 배포의 경우, 이 저작물에 적용된 이용허락조건을 명확하게 나타내어야 합니다.
- 저작권자로부터 별도의 허가를 받으면 이러한 조건들은 적용되지 않습니다.

저작권법에 따른 이용자의 권리는 위의 내용에 의하여 영향을 받지 않습니다.

이것은 [이용허락규약\(Legal Code\)](#)을 이해하기 쉽게 요약한 것입니다.

[Disclaimer](#)

공학박사학위논문

**Pure Strain-Rate Effect on Concrete
Compressive Strength in Confined
Split Hopkinson Pressure Bar Test**

구속 Split Hopkinson Pressure Bar 실험에서의
콘크리트 압축강도에 대한 순수 변형속도 효과

2022 년 8 월

서울대학교 대학원

건설환경공학부

이 상 호

Pure Strain-Rate Effect on Concrete Compressive Strength in Confined Split Hopkinson Pressure Bar Test

구속 Split Hopkinson Pressure Bar 실험에서의
콘크리트 압축강도에 대한 순수 변형속도 효과

지도 교수 조 재 열

이 논문을 공학박사 학위논문으로 제출함
2022 년 5 월

서울대학교 대학원
건설환경공학부
이 상 호

이상호의 공학박사 학위논문을 인준함
2022 년 6 월

위 원 장 _____ (인)

부위원장 _____ (인)

위 원 _____ (인)

위 원 _____ (인)

위 원 _____ (인)

ABSTRACT

Pure Strain-Rate Effect on Concrete Compressive Strength in Confined Split Hopkinson Pressure Bar Test

Lee, Sangho

Department of Civil & Environmental Engineering

The Graduate School

Seoul National University

The dynamic compressive properties of concrete should be considered to accurately evaluate the behavior of concrete structures under extreme loadings and to economically design the structures since concrete compressive strength is enhanced at high strain rates. Dynamic increase factor (DIF), which is generally defined as the ratio of dynamic strength to static strength, has been employed to consider the strain-rate effect in the analysis on concrete structures under extreme loadings, and DIF has been investigated using the split Hopkinson pressure bar (SHPB) test technique.

However, it is difficult to apply DIF that is obtained from SHPB tests to finite element analysis (FEA). This is because the information about strain rate and stress is not sufficient. In conventional SHPB tests, strain and stress in the lateral directions, as well as those in the axial direction, are generated due to the Poisson effect. However, only the axial strain rate and stress are measured in the conventional SHPB tests, and the apparent DIF is acquired as

a function of the axial strain rate. On the other hand, most concrete constitutive models for three-dimensional FEA consider the DIF a function of six strain rate components in all directions, such as a function of the effective strain rate or effective deviatoric strain rate. Moreover, the DIF is assumed to be the pure rate DIF that is based on the uniaxial stress state. Consequently, the apparent DIF–axial strain rate relationship that is obtained from the conventional SHPB tests cannot be applied to FEA, and the pure rate DIF–effective strain rate relationship should be obtained for FEA by acquiring the information of all strain rate and stress components.

The confined SHPB test technique can be an alternative to solving the problem of the conventional SHPB test. The confined SHPB test is an experimental technique to investigate the dynamic properties of materials in multi-axial stress states, and all strain rate and stress components can be measured in the confined SHPB test. However, there are few research cases to investigate the pure rate DIF of concrete through the confined SHPB test so far, and the methodology to assess the pure rate DIF has not been also established.

The objectives of this study are to suggest the methodology for evaluating the strength enhancement due to the strain-rate effect using the confined SHPB test and to develop the pure rate DIF model. For these objectives, this study conducted a series of numerical and experimental work. First of all, the dynamic compressive behavior of concrete subjected to lateral constraints was investigated through numerical analysis. Based on the results, the methodology for obtaining the pure rate DIF in the confined SHPB test was proposed and verified. Secondly, the confined SHPB test was performed

to obtain the pure rate DIF data, and the conventional SHPB test was also conducted for the purpose of comparison. The apparent DIF obtained from the conventional SHPB test showed higher values than the pure rate DIF from the confined SHPB test, which implied that the use of the apparent DIF for the design or analysis of structures under extreme loadings leads to unsafe results. In addition, the pure rate DIF model was suggested through regression analysis on the confined SHPB test data. Lastly, numerical analysis was conducted to verify and apply the suggested pure rate DIF model. FEA on the conventional SHPB tests was performed considering the apparent and pure rate DIFs. Furthermore, FEA on the drop-weight impact tests on reinforced concrete beams was also conducted with DIFs of concrete compressive strength as a variable. The FEA results indicated that FEA with the suggested pure rate DIF predicted appropriately dynamic behavior of concrete specimens and impact behavior of concrete structures. In conclusion, it was confirmed that the suggested methodology and pure rate DIF model were valid.

Keywords: dynamic increase factor, strain-rate effect, inertial effect, uniaxial strain state, split Hopkinson pressure bar, concrete dynamic compressive strength

Student Number: 2017-39671

TABLE OF CONTENTS

LIST OF TABLES	ix
----------------------	----

LIST OF FIGURES	x
-----------------------	---

NOTATIONS	xx
-----------------	----

1. Introduction	1
-----------------------	---

1.1. Research background	1
--------------------------------	---

1.2. Research objectives and scope	7
--	---

1.3. Outline	9
--------------------	---

2. Literature Review	11
----------------------------	----

2.1. Split Hopkinson pressure bar test	11
--	----

2.1.1. Introduction of SHPB test	11
--	----

2.1.2. Limitations of implementing DIF obtained from SHPB test ·	14
--	----

2.1.2.1. <i>Insufficient strain rate information</i>	14
--	----

2.1.2.2. <i>Insufficient stress information</i>	16
---	----

2.2. Previous studies on implementation of DIF	20
--	----

2.2.1. Fang and Wu (2017)	20
---------------------------------	----

2.2.2. Lu and Li (2011)	21
-------------------------------	----

2.2.3. Xu and Wen (2013)	22
--------------------------------	----

2.2.4. Lee et al. (2018)	23
--------------------------------	----

2.2.5. Liu and Li (2019)	24
2.3. Previous studies on confined SHPB test	26
2.3.1. Gong and Malvern (1990)	27
2.3.2. Forquin et al. (2008)	28
2.3.3. Forquin et al. (2010)	30
2.3.4. Forquin et al. (2015)	31
2.3.5. Piotrowska et al. (2016)	32
2.4. Concluding remarks	34
3. Methodology for Evaluation of Pure Rate DIF	36
3.1. Numerical analysis on confined SHPB test	36
3.1.1. Establishment of numerical model	36
3.1.1.1. <i>Modeling part and boundary conditions</i>	36
3.1.1.2. <i>Concrete specimen</i>	37
3.1.2. Data-processing procedure	40
3.1.3. Numerical analysis results	41
3.1.3.1. <i>Strain-rate-independent case</i>	41
3.1.3.2. <i>Strain-rate-dependent case</i>	43
3.2. Methodology for evaluation of pure rate DIF	45
3.3. Concluding remarks	49
4. SHPB Test Program	50
4.1. Test variables	50
4.2. Specimen preparation	51

4.3. Test procedures	54
4.3.1. Conventional SHPB test	54
4.3.1.1. <i>Test procedure</i>	54
4.3.1.2. <i>Measurement and data-processing procedure</i>	56
4.3.2. Static confined compressive test	61
4.3.2.1. <i>Design of steel ring and disks</i>	61
4.3.2.2. <i>Test procedure</i>	66
4.3.2.3. <i>Measurement, data-processing procedure and test results</i>	67
4.3.3. Confined SHPB test	71
4.3.3.1. <i>Test procedure</i>	71
4.3.3.2. <i>Measurement and data-processing procedure</i>	73
4.4. Test results and discussion	77
4.4.1. Assessment of dynamic stress equilibrium	77
4.4.2. Comparison between conventional and confined SHPB tests	78
4.4.3. Suggestion of pure rate DIF model	79
4.5. Concluding remarks	83
 5. Verification and Application of Suggested DIF	85
5.1. Numerical analysis on SHPB test	85
5.1.1. Establishment of numerical model	85
5.1.1.1. <i>Modeling part and boundary conditions</i>	85
5.1.1.2. <i>Concrete specimen</i>	86
5.1.2. Data acquisition and processing procedure	92

Appendix B	170
-------------------------	------------

국문초록	199
-------------------	------------

LIST OF TABLES

Table 1.1 Application of DIF in representative concrete constitutive models	6
Table 3.1 Concrete model parameter details (unit: ton, mm, sec)	39
Table 3.2 Default yield scale factor (η)–damage function (λ) relationship	39
Table 3.3 EOS model parameters	40
Table 3.4 Estimation of the pure rate DIF	48
Table 4.1 Mix proportion of concrete specimens	51
Table 4.2 Static material properties	53
Table 4.3 Characteristics of bar components	54
Table 4.4 Material properties of the steel ring and disks	61
Table 5.1 Concrete model parameter details (unit: ton, mm, sec)	90
Table 5.2 $\eta - \lambda$ relationship proposed by Markovich et al. (2011)	91
Table 5.3 EOS model parameters	92
Table 5.4 Distribution characteristics of the apparent strength ratio	100
Table 5.5 Test variables of the drop-weight impact tests (Ahn, 2021)	103
Table 5.6 Static material properties of concrete	104
Table 5.7 Static material properties of reinforcing bars	105
Table 5.8 Concrete model parameter details (unit: ton, mm, sec)	122
Table 5.9 EOS model parameters	123
Table 5.10 Elastic linear material properties of reinforcing bars	123
Table 5.11 Material properties of the drop-weight	126
Table 5.12 Material properties of the upper and bottom supports	126
Table 5.13 Mean and COV values of the maximum deflection ratios	136
Table 5.14 Mean and COV values of the residual deflection ratios	137

LIST OF FIGURES

Figure 1.1 Strain rate for various loadings (fib Bulletin 66, 2012)·····	1
Figure 1.2 Typical static and dynamic axial stress–strain relationships ·····	2
Figure 1.3 Various DIF models of concrete compressive strength ·····	3
Figure 1.4 SHPB test setup·····	4
Figure 2.1 Application of DIF to constitutive models; (a) Enhancement of failure surface; (b) Overstress added to inviscid stress ·····	19
Figure 2.2 Overestimated dynamic failure surface with the apparent DIF ···	19
Figure 2.3 Apparent DIF correction procedure proposed by Lu and Li (2011) ·····	22
Figure 2.4 DIF versus stress triaxiality (Liu and Li, 2019)·····	25
Figure 2.5 Strength enhancement along uniaxial stress and strain paths based on Drucker-Prager model (Liu and Li, 2019) ·····	25
Figure 2.6 Specimens, steel disks and steel ring (Forquin et al., 2015)·····	27
Figure 2.7 Test configuration of Gong and Malvern (1990) ·····	28
Figure 2.8 Specimen cell configuration of Forquin et al. (2008) ·····	29
Figure 2.9 Test results of Forquin et al. (2008) ·····	29
Figure 2.10 Test results of Forquin et al. (2010); (a) Dried specimens; (b) Water-saturated specimens ·····	31
Figure 2.11 Test results of Forquin et al. (2015)·····	32
Figure 2.12 Test results of Piotrowska et al. (2016); (a) Concrete with siliceous aggregates; (b) Concrete with limestone aggregates ····	33
Figure 3.1 Specimen model and boundary conditions ·····	37
Figure 3.2 Prescribed nodal velocity in the x-axis direction on the loaded end ·····	37
Figure 3.3 FEA results of the strain-rate-independent case (V10); (a) Axial stress–strain relationship; (b) Loading path ·····	43

Figure 3.4 FEA results of the strain-rate-dependent case (V10); (a) Axial stress–strain relationship; (b) Loading path	44
Figure 3.5 Procedure for evaluating the pure rate DIF	46
Figure 3.6 FEA results of the strain-rate-dependent case with the failure point (V10); (a) Axial stress–strain relationship; (b) Loading path	47
Figure 3.7 Comparison of the estimated DIF with the input DIF curve	48
Figure 4.1 Designation of test cases	50
Figure 4.2 Seamless molds for specimens of confined tests	52
Figure 4.3 Fabricated specimens	52
Figure 4.4 SHPB apparatus	55
Figure 4.5 Conventional SHPB test setup; (a) Pulse shaper; (b) Lubricated specimen; (c) Mounted specimen	56
Figure 4.6 Typical test results of the conventional SHPB test (Conv-V10-1); (a) Stress waves; (b) Strain of a specimen	58
Figure 4.7 Typical failure pattern of a specimen at the peak stress point (Conv-V10-1)	58
Figure 4.8 Typical axial stress–strain relationship and axial strain rate history in the conventional SHPB test (Conv-V10-1)	60
Figure 4.9 Schematic diagram of the steel ring (unit: mm)	62
Figure 4.10 Steel ring models	63
Figure 4.11 Loading conditions; (a) Loaded segments; (b) Internal pressure history	64
Figure 4.12 Internal pressure estimated from the circumferential strain data	65
Figure 4.13 Cross-sectional drawing of the specimen cell	65
Figure 4.14 Manufactured steel ring and specimen	66
Figure 4.15 Static confined compressive test setup; (a) Lubrication using PTFE grease; (b) Mounted specimen cell	66

Figure 4.16 Measurement of strain of the steel ring; (a) Strain gauge positions; (b) Typical external circumferential strain of the steel ring (Conf-S-1)	68
Figure 4.17 Loading path of specimens in the static confined compressive test	69
Figure 4.18 Static maximum failure surface	71
Figure 4.19 Confined SHPB test setup; (a) Drawing; (b) Lubricated specimen cell; (c) Mounted specimen cell	72
Figure 4.20 Typical test results of the confined SHPB test (Conf-V17-1); (a) Stress waves; (b) External circumferential strain of the steel ring	74
Figure 4.21 Typical test results of the confined SHPB test (Conf-V17-1); (a) Axial stress–strain relationship and axial strain rate history; (b) Loading path and dynamic failure surface	76
Figure 4.22 Assessment of dynamic stress equilibrium of specimens	78
Figure 4.23 DIF–effective deviatoric strain rate relationships	79
Figure 4.24 Proposed DIF models	81
Figure 4.25 Comparison of the suggested pure rate DIF model with the existing pure rate DIF models	82
Figure 5.1 Specimen model and boundary conditions	86
Figure 5.2 Deformation velocities of specimens in the conventional SHPB test	86
Figure 5.3 DIF models of compressive strength	87
Figure 5.4 DIF model of tensile strength	88
Figure 5.5 Failure surfaces	89
Figure 5.6 $\eta - \lambda$ relationships	91
Figure 5.7 Typical axial stress–strain relationships in the FEA; (a) Pure rate DIF case; (b) Apparent DIF case; (c) No DIF case	94
Figure 5.8 Numerical model to validate the KCC model and model parameters	96

Figure 5.9 Comparison of static stress–strain relationship	96
Figure 5.10 Comparison of dynamic stress–strain relationship; (a) Conv-V6; (b) Conv-V8; (c) Conv-V10; (d) Conv-V12; (e) Conv-V14	98
Figure 5.11 Apparent strength ratio	100
Figure 5.12 Apparent DIF–effective deviatoric strain rate relationships	101
Figure 5.13 Drop-weight impact tests for RC beams of Ahn (2021)	103
Figure 5.14 Drawings of RC beams (Ahn, 2021)	104
Figure 5.15 Crack patterns of RC beams (Ahn, 2021)	106
Figure 5.16 Measurement in the drop-weight impact tests (Ahn, 2021)	107
Figure 5.17 Force time histories of Ahn (2021); (a) E30-FS1; (b) E50-FS1; (c) E30-FS2; (d) E50-FS2; (e) E30-FS3; (f) E50-FS3	110
Figure 5.18 Central deflection time histories of Ahn (2021); (a) E30-FS1; (b) E50-FS1; (c) E30-FS2; (d) E50-FS2; (e) E50-FS3	112
Figure 5.19 Typical force time history in the FEA using pure rate DIF (a) Force time history; (b) Dynamic equilibrium assessment	114
Figure 5.20 Dynamic equilibrium assessment; (a) E30-FS1; (b) E50-FS1; (c) E30-FS2; (d) E50-FS2; (e) E30-FS3; (f) E50-FS3	117
Figure 5.21 Modeling parts and boundary conditions	118
Figure 5.22 DIF models of compressive strength	120
Figure 5.23 Failure surfaces	121
Figure 5.24 Strain-hardening models of reinforcing bars	124
Figure 5.25 DIF models of reinforcing bars	125
Figure 5.26 SDM contours of the FEA with the pure rate DIF	127
Figure 5.27 Comparison of SDM contours (a) E30-FS1; (b) E50-FS1; (c) E30-FS2; (d) E50-FS2; (e) E30-FS3; (f) E50-FS3	131
Figure 5.28 Central deflection time history (a) E30-FS1; (b) E50-FS1; (c) E30-FS2; (d) E50-FS2; (e) E30-FS3; (f) E50-FS3	134
Figure 5.29 Distribution of deflection ratios; (a) Maximum deflection ratio; (b) Residual deflection ratio	136

Figure A.1 Test results of Conv-V6-1; (a) Stress waves; (b) Axial stress–strain curve	155
Figure A.2 Test results of Conv-V6-2; (a) Stress waves; (b) Axial stress–strain curve	155
Figure A.3 Test results of Conv-V6-3; (a) Stress waves; (b) Axial stress–strain curve	156
Figure A.4 Test results of Conv-V6-4; (a) Stress waves; (b) Axial stress–strain curve	156
Figure A.5 Test results of Conv-V6-5; (a) Stress waves; (b) Axial stress–strain curve	157
Figure A.6 Test results of Conv-V6-6; (a) Stress waves; (b) Axial stress–strain curve	157
Figure A.7 Test results of Conv-V8-1; (a) Stress waves; (b) Axial stress–strain curve	158
Figure A.8 Test results of Conv-V8-2; (a) Stress waves; (b) Axial stress–strain curve	158
Figure A.9 Test results of Conv-V8-3; (a) Stress waves; (b) Axial stress–strain curve	159
Figure A.10 Test results of Conv-V8-4; (a) Stress waves; (b) Axial stress–strain curve	159
Figure A.11 Test results of Conv-V8-5; (a) Stress waves; (b) Axial stress–strain curve	160
Figure A.12 Test results of Conv-V8-6; (a) Stress waves; (b) Axial stress–strain curve	160
Figure A.13 Test results of Conv-V10-1; (a) Stress waves; (b) Axial stress–strain curve	161
Figure A.14 Test results of Conv-V10-2; (a) Stress waves; (b) Axial stress–strain curve	161

Figure A.15 Test results of Conv-V10-3; (a) Stress waves; (b) Axial stress– strain curve	162
Figure A.16 Test results of Conv-V10-4; (a) Stress waves; (b) Axial stress– strain curve	162
Figure A.17 Test results of Conv-V10-5; (a) Stress waves; (b) Axial stress– strain curve	163
Figure A.18 Test results of Conv-V10-6; (a) Stress waves; (b) Axial stress– strain curve	163
Figure A.19 Test results of Conv-V12-1; (a) Stress waves; (b) Axial stress– strain curve	164
Figure A.20 Test results of Conv-V12-2; (a) Stress waves; (b) Axial stress– strain curve	164
Figure A.21 Test results of Conv-V12-3; (a) Stress waves; (b) Axial stress– strain curve	165
Figure A.22 Test results of Conv-V12-4; (a) Stress waves; (b) Axial stress– strain curve	165
Figure A.23 Test results of Conv-V12-5; (a) Stress waves; (b) Axial stress– strain curve	166
Figure A.24 Test results of Conv-V12-6; (a) Stress waves; (b) Axial stress– strain curve	166
Figure A.25 Test results of Conv-V14-1; (a) Stress waves; (b) Axial stress– strain curve	167
Figure A.26 Test results of Conv-V14-2; (a) Stress waves; (b) Axial stress– strain curve	167
Figure A.27 Test results of Conv-V14-3; (a) Stress waves; (b) Axial stress– strain curve	168
Figure A.28 Test results of Conv-V14-4; (a) Stress waves; (b) Axial stress– strain curve	168

Figure A.29 Test results of Conv-V14-5; (a) Stress waves; (b) Axial stress–strain curve	169
Figure A.30 Test results of Conv-V14-6; (a) Stress waves; (b) Axial stress–strain curve	169
Figure B.1 Test results of Conf-V10-1; (a) Stress waves; (b) Circumferential strain of steel ring; (c) Axial stress–strain curve; (d) Loading path and dynamic failure surface	171
Figure B.2 Test results of Conf-V10-2; (a) Stress waves; (b) Circumferential strain of steel ring; (c) Axial stress–strain curve; (d) Loading path and dynamic failure surface	172
Figure B.3 Test results of Conf-V10-3; (a) Stress waves; (b) Circumferential strain of steel ring; (c) Axial stress–strain curve; (d) Loading path and dynamic failure surface	173
Figure B.4 Test results of Conf-V10-4; (a) Stress waves; (b) Circumferential strain of steel ring; (c) Axial stress–strain curve; (d) Loading path and dynamic failure surface	174
Figure B.5 Test results of Conf-V10-5; (a) Stress waves; (b) Circumferential strain of steel ring; (c) Axial stress–strain curve; (d) Loading path and dynamic failure surface	175
Figure B.6 Test results of Conf-V12-1; (a) Stress waves; (b) Circumferential strain of steel ring; (c) Axial stress–strain curve; (d) Loading path and dynamic failure surface	176
Figure B.7 Test results of Conf-V12-2; (a) Stress waves; (b) Circumferential strain of steel ring; (c) Axial stress–strain curve; (d) Loading path and dynamic failure surface	177
Figure B.8 Test results of Conf-V12-3; (a) Stress waves; (b) Circumferential strain of steel ring; (c) Axial stress–strain curve; (d) Loading path and dynamic failure surface	178

Figure B.9 Test results of Conf-V12-4; (a) Stress waves; (b) Circumferential strain of steel ring; (c) Axial stress–strain curve; (d) Loading path and dynamic failure surface	179
Figure B.10 Test results of Conf-V12-5; (a) Stress waves; (b) Circumferential strain of steel ring; (c) Axial stress–strain curve; (d) Loading path and dynamic failure surface	180
Figure B.11 Test results of Conf-V12-6; (a) Stress waves; (b) Circumferential strain of steel ring; (c) Axial stress–strain curve; (d) Loading path and dynamic failure surface	181
Figure B.12 Test results of Conf-V14-1; (a) Stress waves; (b) Circumferential strain of steel ring; (c) Axial stress–strain curve; (d) Loading path and dynamic failure surface	182
Figure B.13 Test results of Conf-V14-2; (a) Stress waves; (b) Circumferential strain of steel ring; (c) Axial stress–strain curve; (d) Loading path and dynamic failure surface	183
Figure B.14 Test results of Conf-V14-3; (a) Stress waves; (b) Circumferential strain of steel ring; (c) Axial stress–strain curve; (d) Loading path and dynamic failure surface	184
Figure B.15 Test results of Conf-V14-4; (a) Stress waves; (b) Circumferential strain of steel ring; (c) Axial stress–strain curve; (d) Loading path and dynamic failure surface	185
Figure B.16 Test results of Conf-V14-5; (a) Stress waves; (b) Circumferential strain of steel ring; (c) Axial stress–strain curve; (d) Loading path and dynamic failure surface	186
Figure B.17 Test results of Conf-V14-6; (a) Stress waves; (b) Circumferential strain of steel ring; (c) Axial stress–strain curve; (d) Loading path and dynamic failure surface	187

Figure B.18 Test results of Conf-V16-1; (a) Stress waves; (b) Circumferential strain of steel ring; (c) Axial stress–strain curve; (d) Loading path and dynamic failure surface	188
Figure B.19 Test results of Conf-V16-2; (a) Stress waves; (b) Circumferential strain of steel ring; (c) Axial stress–strain curve; (d) Loading path and dynamic failure surface	189
Figure B.20 Test results of Conf-V16-3; (a) Stress waves; (b) Circumferential strain of steel ring; (c) Axial stress–strain curve; (d) Loading path and dynamic failure surface	190
Figure B.21 Test results of Conf-V16-4; (a) Stress waves; (b) Circumferential strain of steel ring; (c) Axial stress–strain curve; (d) Loading path and dynamic failure surface	191
Figure B.22 Test results of Conf-V16-5; (a) Stress waves; (b) Circumferential strain of steel ring; (c) Axial stress–strain curve; (d) Loading path and dynamic failure surface	192
Figure B.23 Test results of Conf-V16-6; (a) Stress waves; (b) Circumferential strain of steel ring; (c) Axial stress–strain curve; (d) Loading path and dynamic failure surface	193
Figure B.24 Test results of Conf-V17-1; (a) Stress waves; (b) Circumferential strain of steel ring; (c) Axial stress–strain curve; (d) Loading path and dynamic failure surface	194
Figure B.25 Test results of Conf-V17-2; (a) Stress waves; (b) Circumferential strain of steel ring; (c) Axial stress–strain curve; (d) Loading path and dynamic failure surface	195
Figure B.26 Test results of Conf-V17-3; (a) Stress waves; (b) Circumferential strain of steel ring; (c) Axial stress–strain curve; (d) Loading path and dynamic failure surface	196

Figure B.27 Test results of Conf-V17-4; (a) Stress waves; (b) Circumferential strain of steel ring; (c) Axial stress–strain curve; (d) Loading path and dynamic failure surface 197

Figure B.28 Test results of Conf-V17-5; (a) Stress waves; (b) Circumferential strain of steel ring; (c) Axial stress–strain curve; (d) Loading path and dynamic failure surface 198

NOTATIONS

Symbol	Definition and description
A_b	Cross-sectional area of bar components
A_d	Cross-sectional area of steel disks
A_s	Cross-sectional area of a specimen
a_0, a_1, a_2	Maximum failure surface parameters in Karagozian and Case concrete model
a_{0y}, a_{1y}, a_{2y}	Yield failure surface parameters in Karagozian and Case concrete model
a_{1f}, a_{2f}	Residual failure surface parameters in Karagozian and Case concrete model
b_1, b_2, b_3	Damage scaling factors in Karagozian and Case concrete model
$c_{1,b}$	Wave propagation velocity of bar components
d_s	Initial diameter of a specimen
E_b	Elastic modulus of bar components
E_d	Elastic modulus of steel disks
E_{ring}	Elastic modulus of a steel ring
$\dot{\epsilon}$	Deviatoric strain rate
$\dot{\epsilon}_0$	Reference deviatoric strain rate
$\dot{\epsilon}_{eff}$	Effective deviatoric strain rate
$\dot{\epsilon}_{eff}^p$	Effective plastic deviatoric strain rate

$\dot{\epsilon}_{ij}$	Deviatoric strain rate tensor
$\dot{\epsilon}_{ij}^p$	Plastic deviatoric strain rate tensor
F_{back}	Nodal force on the back end of a specimen
F_{front}	Nodal force on the front end of a specimen
F_{Impact}	Impact force in the drop-weight impact tests
$F_{Inertial}$	Inertial force in the drop-weight impact tests
F_m	The upper limit of dynamic increase factor model
$F_{Reaction}$	Reaction force in the drop-weight impact tests
f_c	Static compressive strength of concrete
f_d	Dynamic compressive strength of concrete
$f_{d,app}$	Apparent dynamic compressive strength
$f_{d,rate}$	Dynamic compressive strength based on uniaxial stress state
f_t	Static tensile strength of concrete
f_y	Yield strength of reinforcing bar
G_{max}	The maximum coarse aggregate size
K_u	Unloading bulk modulus
k_1	Coefficient related to the strain-rate effect
k_2	Coefficient related to the lateral inertial effect
k_3	Coefficient related to the axial inertial effect
l_d	Initial length of steel disks
l_s	Initial length of a specimen

N_{element}	The number of elements of a specimen
N_{node}	The number of nodes on an end of a specimen
p	Pressure
p_f	Pressure value at a failure point
R	R-value (an indicator of dynamic stress equilibrium)
R_{AS}	Apparent strength ratio
$R_{d,\max}$	Ratio of the maximum deflection in a finite element analysis to that in a drop-weight impact test
$R_{d,\text{residual}}$	Ratio of a residual deflection in a finite element analysis to that in a drop-weight impact test
$r_{i,\text{ring}}$	Radius of an inner surface of a steel ring
$r_{o,\text{ring}}$	Radius of an outer surface of a steel ring
S	Coefficient related to the slope of dynamic increase factor model
S_{ij}	Deviatoric stress tensor
t	Time
u_{back}	Nodal displacement on the back end of a specimen
u_{front}	Nodal displacement on the front end of a specimen
v_{back}	Particle velocity on the interface between a transmitted bar and a specimen
v_d	Deformation velocity of a specimen
v_{front}	Particle velocity on the interface between an incident bar and a specimen
W_x	Coefficient related to the location of the inflection point in dynamic increase factor model

W_y	Coefficient related to the lower limit of dynamic increase factor model
w_{lz}	Localization width in Karagozian and Case concrete model
β	Hardening or softening parameter
γ	Dynamic increase factor
γ_{ACI349}	Dynamic increase factor of compressive strength in ACI 349-13
$\gamma_{ACI370R}$	Dynamic increase factor of compressive strength in ACI 370R-14
γ_{app}	Apparent dynamic increase factor
$\gamma_{estimated}$	Estimation of dynamic increase factor
γ_{fib}	Dynamic increase factor of compressive strength in fib MC2010
γ_{input}	Input dynamic increase factor
γ_{rate}	Pure rate dynamic increase factor
γ_t	Dynamic increase factor of tensile strength
γ_y	Dynamic increase factor of yield strength of reinforcing bar
$\Delta_{FEA,max}$	The maximum deflection of a reinforced concrete beam in a finite element analysis
$\Delta_{FEA,residual}$	Residual deflection of a reinforced concrete beam in a finite element analysis
$\Delta_{test,max}$	The maximum deflection of a reinforced concrete beam in a drop-weight impact test
$\Delta_{test,residual}$	Residual deflection of a reinforced concrete beam in a drop-weight impact test

$\Delta f_{inertial}$	Strength enhancement due to inertial effects
Δt	Constant time step between the i-th and (i+1)-th steps
$\Delta \sigma$	Principal stress difference
$\Delta \sigma_d$	Dynamic failure surface (or dynamic stress point)
$\Delta \sigma_s$	Static failure surface
δ	Scaled damage measure in Karagozian and Case concrete model
δ_{ij}	Kronecker delta
$\varepsilon_{incident}$	Incident strain wave
ε_r	Radial strain of a specimen
$\varepsilon_{r,i}$	Radial strain at the i-th time step
ε_r^{eng}	Engineering radial strain of a specimen
$\varepsilon_{reflect}$	Reflected strain wave
$\varepsilon_{total}^{eng}$	Total strain including the deformation of a specimen and steel disks
$\varepsilon_{transmitted}$	Transmitted strain wave
ε_v	Volumetric strain
ε_x	Axial strain of a specimen
$\varepsilon_{x,i}$	Axial strain at the i-th time step
ε_x^{eng}	Engineering axial strain of a specimen
ε_θ	Circumferential strain of a specimen
$\varepsilon_{\theta,ring}$	Circumferential strain at the center on an external surface of a steel ring
$\dot{\varepsilon}$	Strain rate matrix

$\dot{\epsilon}$	Strain rate
$\dot{\epsilon}_0$	Reference strain rate
$\dot{\epsilon}_{eff}$	Effective strain rate
$\dot{\epsilon}_{eff}^p$	Effective plastic strain rate
$\dot{\epsilon}_{ij}$	Strain rate tensor
$\dot{\epsilon}_{ij}^p$	Plastic strain rate tensor
$\dot{\epsilon}_{max}$	The maximum principal strain rate
$\dot{\epsilon}_{min}$	The minimum principal strain rate
$\dot{\epsilon}_r$	Radial strain rate
$\dot{\epsilon}_{r,i}$	Radial strain rate at the i-th time step
$\dot{\epsilon}_{total}^{eng}$	Total strain rate including the deformation of a specimen and steel disks
$\dot{\epsilon}_v$	Volumetric strain rate
$\dot{\epsilon}_x$	Axial strain rate
$\dot{\epsilon}_{x,i}$	Axial strain rate at the i-th time step
$\dot{\epsilon}_x^{eng}$	Engineering axial strain rate of a specimen
$\dot{\epsilon}_\theta$	Circumferential strain rate
$\dot{\epsilon}_x^{eng}$	Engineering axial strain acceleration of a specimen
η	Yield scale factor in Karagozian and Case concrete model
λ	Damage function in Karagozian and Case concrete model
λ_m	Damage function value corresponding to $\eta = 1$
ν	Poisson's ratio

ν_{ring}	Poisson's ratio of a steel ring
ν_s	Poisson's ratio of a specimen
ξ	Slope of Drucker-Prager model
ρ_s	Density of a specimen
σ	Stress matrix
σ_{over}	Overstress
σ_r	Radial stress of a specimen
σ_x	Axial stress of a specimen
$\sigma_{x,back}$	Axial stress on the interface between a transmitted bar and a specimen (back stress)
$\sigma_{x,front}$	Axial stress on the interface between an incident bar and a specimen (front stress)
σ_x^{eng}	Engineering axial stress of a specimen
σ_θ	Circumferential stress of a specimen
ψ	Tensile-to-compressive meridian ratio in Karagozian and Case concrete model
ω	Associativity parameter

1. Introduction

1.1. Research background

Recently, the extended design life of social infrastructures has increased the probability that the structures experience extreme events during their design life, and the enlargement of the structures has increased the risk of loss of life and property in the event of a structure collapse. For these reasons, the safety of structures from extreme events has become more important than in the past, and extreme loadings, in addition to traditional loadings, have been considered in infrastructure design.

The extreme loadings are time-dependent loadings with very large amplitude for a very short duration, and impact and blast loadings are typical extreme loadings. Under these extreme loadings, structures experience high-rate deformation above the strain rate of 10 s^{-1} , as shown in Figure 1.1. Therefore, the dynamic material properties in high strain rate ranges should be investigated for accurate analysis and economical design of structures subjected to extreme loadings.

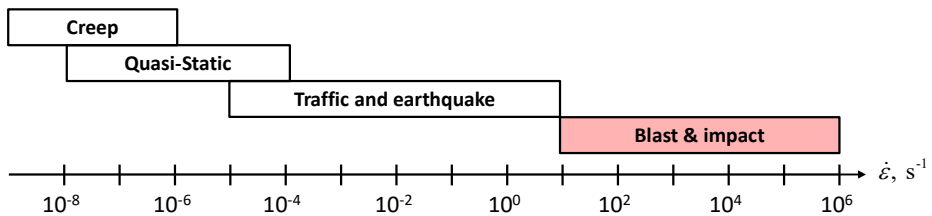


Figure 1.1 Strain rate for various loadings (fib Bulletin 66, 2012)

Concrete, one of the most widely used construction materials, is a strain-rate-dependent material. As shown in Figure 1.2, concrete compressive strength is enhanced as the strain rate increases, and this strength enhancement is called the rate effect, or strain-rate effect on the concrete compressive strength. Currently, the dynamic increase factor (DIF), which is generally defined as the ratio of dynamic compressive strength to static compressive strength, is widely used to consider the strain-rate effect in design and analysis of concrete structures subjected to extreme loadings. Various DIF models have been suggested based on dynamic material tests, and they have been adopted in design codes and guidelines such as ACI 349-13, ACI 370R-14, fib MC2010, and UFC 3-340-02. Figure 1.3 shows the DIF models of design codes and guidelines.

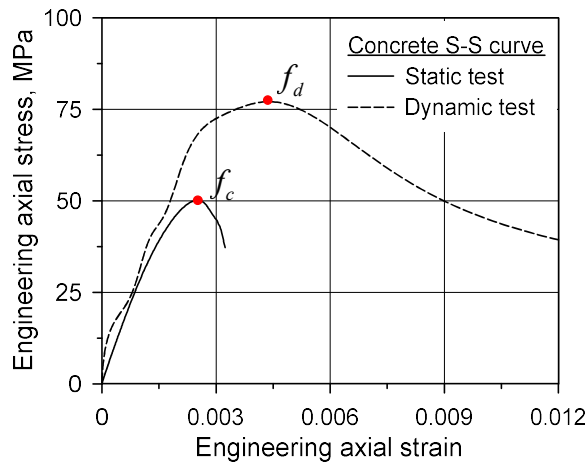


Figure 1.2 Typical static and dynamic axial stress–strain relationships

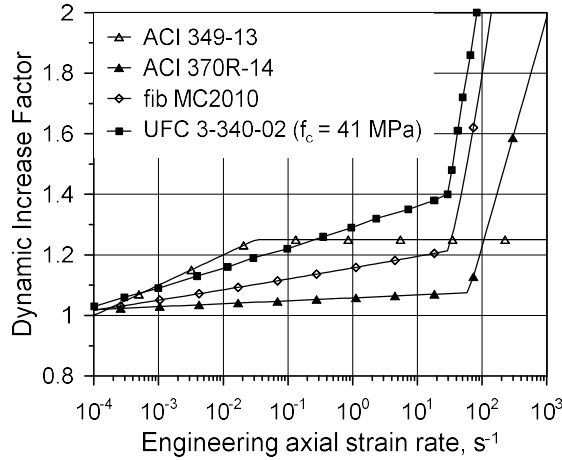


Figure 1.3 Various DIF models of concrete compressive strength

Among dynamic material test techniques, the split Hopkinson pressure bar (SHPB) test is the most popular test technique, and the DIF of concrete has been investigated and suggested through the SHPB tests (Ross et al., 1995; Grote et al., 2001; Zhang et al., 2009; Hao et al., 2013; Lee et al., 2018; Kim et al., 2019; Kim et al., 2022). Figure 1.4 shows the SHPB test setup. In the SHPB test, a specimen is sandwiched between the incident and transmitted bars. Then, the specimen is loaded by the incident stress wave that is generated by collisions of the striker bar with the incident bar (or a pulse shaper at the impact end of the incident bar). At this process, the axial strains of the bar components are measured, and they are converted to the dynamic axial stress–strain curve and axial strain rate history of the specimen using the one-dimensional stress wave theory. As a final result, the DIF–strain rate relationship is obtained.

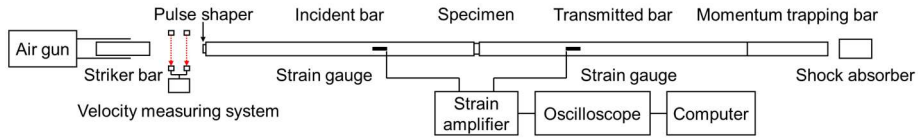


Figure 1.4 SHPB test setup

However, there is an issue concerning the implementation of the DIF obtained from a conventional SHPB test: insufficient information about strain rate and stress. In the conventional SHPB test, a specimen is dilated in the lateral directions due to the Poisson effect, and strains and strain rates in the lateral directions are generated. Furthermore, the lateral stresses due to lateral inertial effects are also generated, and the specimen is at the triaxial stress state. Nevertheless, only the axial stress and strain rate are measured in the conventional SHPB test, and consequently, the apparent DIF–axial strain rate relationship is obtained as test results. On the other hand, most concrete constitutive models for three-dimensional finite element analysis (FEA) consider the DIF a function of the effective strain rate (or the effective deviatoric strain rate) that is determined from six strain rate components in all directions, as shown in Table 1.1. Here, $\dot{\epsilon}_{ij}$, $\dot{\epsilon}_{ij}^p$, and $\dot{\epsilon}_{ij}^d$ denote strain rate, plastic strain rate, and deviatoric strain rate tensors, respectively; $\dot{\epsilon}_v$ means volumetric strain rate; δ_{ij} indicates Kronecker delta; and $\dot{\epsilon}_{\max}$ and $\dot{\epsilon}_{\min}$ denote maximum and minimum principal strain rates, respectively. Moreover, most constitutive models assume the input DIF as the pure rate DIF that is based on the uniaxial stress state, not including any inertial effect. Accordingly, using the apparent DIF including lateral inertial effects might lead to unsafe design or analysis for concrete structures subjected to extreme

loadings by overestimating the actual concrete dynamic resistance. In conclusion, not the apparent DIF–axial strain rate relationship but the pure rate DIF–effective strain rate relationship should be obtained for FEA, and it is necessary to assess the pure rate DIF–effective strain rate relationship by acquiring all strain rate and stress components.

The confined SHPB test technique can be an alternative to solving the problem of the conventional SHPB test. The confined SHPB test is an experimental technique to investigate the dynamic behavior of materials in multi-axial stress states, and in the confined SHPB test, all strain rate and stress components can be measured (Gong and Malvern, 1990; Forquin et al., 2008; Forquin et al., 2010; Forquin et al., 2015; Piotrowska et al., 2016). However, there are few research cases to figure out the pure rate DIF of concrete through the confined SHPB test so far, and the methodology to assess the pure rate DIF has not been established.

Therefore, this study conducted the numerical and experimental work on the confined SHPB tests for concrete specimens to suggest the methodology for evaluating the strength enhancement due to the strain-rate effect and to develop the pure rate DIF model. Moreover, the verification and application of the suggested pure rate DIF were also performed using FEA on the material- and member-level impact tests.

Table 1.1 Application of DIF in representative concrete constitutive models

Material model	Reference	Applying strain rate	Assumed stress state
Karagozian and Case concrete (KCC) model	Malvar et al. (1997) Wu and Crawford (2015) Kong et al. (2017)	$\sqrt{\frac{2}{3}\dot{\epsilon}_{ij}\dot{\epsilon}_{ij}}$	Uniaxial stress state
Winfrith model	Ottosen (1977) Schwer (2011)	$\sqrt{\frac{2}{3}\dot{\epsilon}_{ij}\dot{\epsilon}_{ij}}$	Uniaxial stress state
Johnson-Holmquist-Cook (JHC) model	Holmquist et al. (1993)	Unclear	Neither uniaxial stress nor uniaxial strain state
Continuous surface cap (CSC) model	Murray (2007) Murray et al. (2007)	$\sqrt{\frac{2}{3}\sum_{j=1}^3\sum_{i=1}^j(\dot{\epsilon}_{ij}-\delta_{ij}\dot{\epsilon}_v)^2}$	Uniaxial stress state
Riedel-Hiermaier-Thoma (RHT) model	Riedel et al. (2009) Borrvall and Riedel (2011)	$\sqrt{\frac{2}{3}\dot{\epsilon}_{ij}^p\dot{\epsilon}_{ij}^p}$	Uniaxial stress state
Concrete damage plastic (CDP) model	Grassl and Jirásek (2006) Grassl et al. (2011) Grassl et al. (2013)	$\dot{\epsilon}_{\max}$ for tension $\dot{\epsilon}_{\min}$ for compression	Unclear

1.2. Research objectives and scope

There were two main objectives in this study: (1) suggesting the methodology for evaluating the pure rate DIF of concrete compressive strength in the confined SHPB test, and (2) developing the pure rate DIF model that can be used for FEA through the suggested methodology.

For these objectives, this study consisted of three parts. The first part is a numerical investigation into the confined SHPB test for a concrete specimen. The dynamic compressive behavior of concrete subjected to lateral constraints was investigated through numerical analysis, and the methodology for obtaining the pure rate DIF in the confined SHPB test was proposed and verified based on the numerical analysis results.

The second part is an experimental study to develop the pure rate DIF model. The confined SHPB test was performed to obtain the pure rate DIF data, and the conventional SHPB test was also conducted for the purpose of comparison. The pure rate DIF model was suggested through regression analysis on the confined SHPB test data.

The last part is numerical analysis for verification and application of the suggested pure rate DIF model. For verification, FEA on the conventional SHPB test of this study was performed considering the apparent and pure rate DIFs. For application, FEA on the drop-weight impact tests for reinforced concrete (RC) beams by Ahn (2021) was conducted with DIFs of concrete compressive strength as a variable. The results of FEA were compared with

respective test results, and the validity of the suggested methodology and pure rate DIF model was discussed.

1.3. Outline

Chapter 1 shows the introduction of this study; the background, objectives, scope, and outline of this study are described.

Chapter 2 explains the introduction and limitation of the conventional SHPB test, and presents the literature review on two kinds of previous studies: (1) studies intending to implement DIF, and (2) studies conducting concrete or mortar confined SHPB tests. The necessity of this study was drawn from the literature review.

Chapter 3 describes the numerical investigation into the confined SHPB test for a concrete specimen to propose the methodology for evaluating pure rate DIF. The modeling procedure and FEA results are included in Chapter 3, and the methodology was suggested based on the FEA results.

Chapter 4 shows the test program of conventional SHPB tests, static confined compressive tests, and confined SHPB tests, including the test procedure, data-processing procedure, and test results. The results of confined SHPB tests were compared with those of conventional SHPB tests in this chapter. Moreover, the pure rate DIF model was suggested through the regression analysis on the confined SHPB test data.

Chapter 5 presents the numerical analysis programs for the conventional SHPB test of this study and the drop-weight impact test for RC beams by Ahn (2021). It includes the modeling procedure, FEA results, and comparison with

corresponding test results. Based on the results, the validity of the suggested pure rate DIF was discussed.

Lastly, Chapter 6 summarizes the conclusions and findings of this study. The recommendations for further research are also described in Chapter 6.

Appendices A and B show all experimental data that was not shown in Chapter 4 for brevity. The results of the conventional and confined SHPB tests are listed in Appendices A and B, respectively.

2. Literature Review

2.1. Split Hopkinson pressure bar test

Since this study intended to overcome the limitations of the conventional SHPB test and to develop a new pure rate DIF model that can be applied to FEA, it was necessary to introduce the conventional SHPB test technique and to discuss its limitation first. Therefore, a brief description and the limitations of the conventional SHPB test technique were presented in this section.

2.1.1. Introduction of SHPB test

The SHPB test technique was developed by Kolsky (1949) to investigate dynamic compressive behavior of materials in the axial direction, and it has been widely used to obtain the dynamic stress–strain relationship of various materials including cementitious materials at intermediate and high strain rate ranges (Ross et al., 1995; Grote et al., 2001; Lok et al., 2002; Zhang et al., 2009; Hao et al., 2013; Lee et al., 2018; Kim et al., 2019; Chun et al., 2021; Kim et al., 2022).

As shown in Figure 1.4, SHPB consists of three parts: loading device, bar components, and data-acquisition system (Chen and Song, 2010). The loading device includes the striker bar and air gun to launch it. Furthermore, a pulse shaper is often used to generate a desirable incident stress wave that prevents dynamic non-equilibrium of a specimen. The bar components are composed of an incident bar and a transmitted bar. The incident bar has a role to transfer stress waves to the specimen, and the transmitted bar is responsible

for receiving the stress waves from the specimen. Generally, the striker, incident and transmitted bars have the same cross-sectional area, and they are made of the same materials for convenience. The data-acquisition system includes the strain gauges attached to the bar components to measure strain wave signals of the bar components.

As briefly explained in Section 1.1, the specimen is sandwiched between the bar components. Then, the striker bar is accelerated by the air gun and collides with the incident bar (or the pulse shaper). As a result of the collision, an incident stress wave is generated and propagated along the incident bar. When the incident stress wave reaches the interface between the incident bar and the specimen, a part of the incident stress wave is transmitted to the specimen and the transmitted bar, and the other part is reflected back into the incident bar, because of the difference in the impedances between the specimen and the bar components.

In the above process, the stress waves vibrate particles of the bar components. The particles on the interfaces between the bar components and the specimen also move with velocities expressed using Equations (2.1) and (2.2), according to one-dimensional stress wave theory (Chen and Song, 2010).

$$v_{front} = c_{1,b} (\varepsilon_{incident} - \varepsilon_{reflect}) \quad (2.1)$$

$$v_{back} = c_{1,b} \varepsilon_{transmitted} \quad (2.2)$$

where v_{front} and v_{back} denote the particle velocities on the interfaces between the incident bar and the specimen and between the transmitted bar and the specimen, respectively; $\varepsilon_{incident}$, $\varepsilon_{reflect}$, and $\varepsilon_{transmitted}$ denote the incident, reflected, and transmitted strain waves, respectively; and $c_{1,b}$ means the wave propagation velocity of the bar components. The engineering axial strain rate and strain of the specimen can be obtained using Equations (2.3) and (2.4), respectively, as follows;

$$\dot{\varepsilon}_x^{eng} = \frac{v_{front} - v_{back}}{l_s} \quad (2.3)$$

$$\varepsilon_x^{eng} = \int_0^t \dot{\varepsilon}_x^{eng}(\tau) d\tau \quad (2.4)$$

where ε_x^{eng} and $\dot{\varepsilon}_x^{eng}$ denote the engineering axial strain and strain rate of the specimen, respectively; l_s denotes the initial length of the specimen; and t means time. The stresses on the interfaces between the bar components and the specimen are expressed using Equations (2.5) and (2.6), respectively, as follows;

$$\sigma_{x,front} = \frac{A_b}{A_s} E_b (\varepsilon_{incident} + \varepsilon_{reflect}) \quad (2.5)$$

$$\sigma_{x,back} = \frac{A_b}{A_s} E_b \varepsilon_{transmitted} \quad (2.6)$$

where $\sigma_{x,front}$ and $\sigma_{x,back}$ denote the stresses on the interfaces between the incident bar and the specimen (front stress) and between the transmitted bar and the specimen (back stress), respectively; A_b and A_s denote cross-sectional areas of the bar components and the specimen, respectively; and E_b is elastic modulus of the bar components. Then, the axial stress of the specimen (σ_x) can be obtained as an average of the front and back stresses of the specimen using Equation (2.7), as follows;

$$\sigma_x = \frac{\sigma_{x,front} + \sigma_{x,back}}{2} \quad (2.7)$$

Finally, the dynamic axial stress–strain relationship and axial strain rate history of the specimen are obtained as final test results, and the DIF is obtained using the peak axial stress in the dynamic axial stress–strain curve.

2.1.2. Limitations of implementing DIF obtained from SHPB test

As mentioned in Section 1.1, even though many DIF models on concrete compressive strength have been proposed based on SHPB tests, these DIF models cannot be directly applied to FEA because of insufficient information about strain rate and stress. This issue is discussed in detail in this section.

2.1.2.1. Insufficient strain rate information

In an SHPB test, a specimen is dilated in the radial and circumferential directions due to the Poisson effect, and the strain rate state of the specimen is expressed using Equation (2.8).

$$\dot{\boldsymbol{\varepsilon}} = \begin{bmatrix} \dot{\varepsilon}_x & 0 & 0 \\ 0 & \dot{\varepsilon}_r & 0 \\ 0 & 0 & \dot{\varepsilon}_\theta \end{bmatrix} \quad (2.8)$$

where $\dot{\boldsymbol{\varepsilon}}$ means strain rate matrix of the specimen; and $\dot{\varepsilon}_x$, $\dot{\varepsilon}_r$, and $\dot{\varepsilon}_\theta$ denote the axial, radial, and circumferential strain rates, respectively. However, as described in Section 2.1.1, the only axial strain rate is measured in the SHPB test, and any information about the lateral strain rates is not obtained. Therefore, in the conventional SHPB test, the DIF model is obtained using Equation (2.9), a function of axial strain rate of the specimen.

$$\gamma(\dot{\varepsilon}_x) = f_d(\dot{\varepsilon}_x) / f_c \quad (2.9)$$

where f_c and f_d denote static and dynamic compressive strengths of concrete, respectively; and γ is DIF.

Meanwhile, since strains in all six directions are generated in general three-dimensional FEA models, the DIF is considered a function of all six strain rates in most concrete constitutive models (Fang and Wu, 2017), as shown in Equations (2.10)–(2.14).

$$\gamma = \gamma(\dot{\varepsilon}_{eff}), \gamma(\dot{\varepsilon}_{eff}^p), \gamma(\dot{\varepsilon}_{eff}) \text{ or } \gamma(\dot{\varepsilon}_{eff}^p) \quad (2.10)$$

$$\dot{\varepsilon}_{eff} = \sqrt{\frac{2}{3} \dot{\varepsilon}_{ij} \dot{\varepsilon}_{ij}} \quad (2.11)$$

$$\dot{\varepsilon}_{eff}^p = \sqrt{\frac{2}{3} \dot{\varepsilon}_{ij}^p \dot{\varepsilon}_{ij}^p} \quad (2.12)$$

$$\dot{\epsilon}_{eff} = \sqrt{\frac{2}{3} \dot{\epsilon}_{ij} \dot{\epsilon}_{ij}} \quad (2.13)$$

$$\dot{\epsilon}_{eff}^p = \sqrt{\frac{2}{3} \dot{\epsilon}_{ij}^p \dot{\epsilon}_{ij}^p} \quad (2.14)$$

where $\dot{\epsilon}$ and $\dot{\epsilon}$ denote strain rate and deviatoric strain rate, respectively; the superscript p means ‘plastic’; the subscript eff means ‘effective’; and the subscript ij denotes the i -th row and j -th column component in a matrix. Indeed, except for the JHC model and CDP model, all constitutive models in Table 1.1 require all six strain rate components to apply the DIF model.

Consequently, the discrepancy between the strain rate of the conventional SHPB test and that of constitutive models makes it difficult to appropriately consider the DIF in FEA, which adversely affects the predictive accuracy of FEA.

2.1.2.2. *Insufficient stress information*

In the conventional SHPB test, the lateral dilatation of a specimen induces the lateral inertial effects in the specimen, thereby resulting in the generation of radial and circumferential stresses (Li and Meng, 2003; Zhang et al., 2009; Li et al., 2009; Kim et al., 2010; Magallanes et al., 2010; Lu and Li, 2011; Xu and Wen, 2013; Fang and Wu, 2017; Lee et al., 2018; Liu and Li, 2019). Accordingly, the stress state of the specimen is expressed using Equation (2.15), as follows;

$$\boldsymbol{\sigma} = \begin{bmatrix} \sigma_x & 0 & 0 \\ 0 & \sigma_r & 0 \\ 0 & 0 & \sigma_\theta \end{bmatrix} \quad (2.15)$$

where $\boldsymbol{\sigma}$ means stress matrix of the specimen; and σ_x , σ_r , and σ_θ denote the axial, radial, and circumferential stresses, respectively. If the axial stress reaches the peak value and the circumferential stress is equal to the radial stress, the stress matrix can be expressed using Equation (2.16), as follows;

$$\boldsymbol{\sigma} = \begin{bmatrix} f_{d,app} & 0 & 0 \\ 0 & \sigma_r & 0 \\ 0 & 0 & \sigma_r \end{bmatrix} \quad (2.16)$$

where $f_{d,app}$ denotes the apparent dynamic compressive strength that is the peak value of the axial stress of the specimen. Nevertheless, the only axial stress is measured in the conventional SHPB test, so the DIF is obtained as the apparent DIF (γ_{app}) that includes the inertial effects, as shown in Equation (2.17).

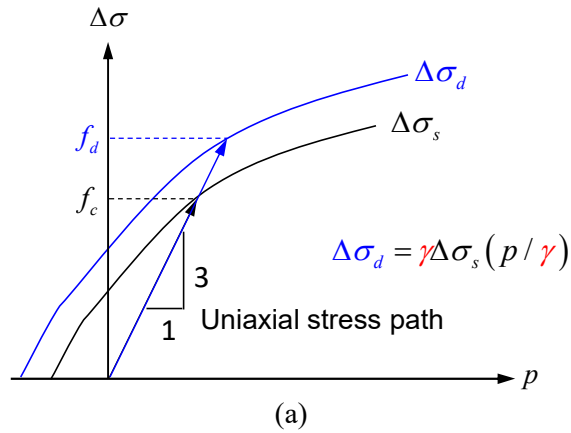
$$\gamma_{app} = f_{d,app} / f_c \quad (2.17)$$

Meanwhile, the DIF model is generally applied to concrete constitutive models for FEA in three ways: enhancement of failure surface (Figure 2.1 (a)), overstress added to inviscid stress (Figure 2.1 (b)), and delay in damage accumulation. In Figure 2.1, p and $\Delta\sigma$ mean pressure and principal stress difference; $\Delta\sigma_s$ and $\Delta\sigma_d$ denote static failure surface and dynamic failure

surface (or dynamic stress point), respectively; and σ_{over} means overstress. It is worth noting that the dynamic failure surface or dynamic stress point is calculated along the uniaxial stress path, which is also indicated in Table 1.1. In other words, most constitutive models consider an input DIF as the DIF purely caused by the strain-rate effect (i.e., the pure rate DIF) rather than the apparent DIF, as shown in Equation (2.18).

$$\gamma_{\text{rate}} = f_{d,\text{rate}} / f_c \quad (2.18)$$

where γ_{rate} and $f_{d,\text{rate}}$ denote the pure rate DIF and dynamic compressive strength based on uniaxial stress state, respectively.



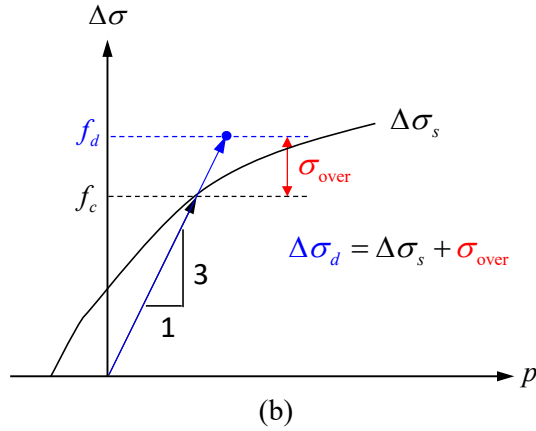


Figure 2.1 Application of DIF to constitutive models; (a) Enhancement of failure surface; (b) Overstress added to inviscid stress

Therefore, if the apparent DIF is used for FEA, the inertial effects are misinterpreted as the strain-rate effect, which leads to the overestimation of dynamic failure surface as shown in Figure 2.2. In order to consider appropriately the strain-rate effect, the uniaxial dynamic strength should be evaluated by assessing the lateral stresses and their effects.

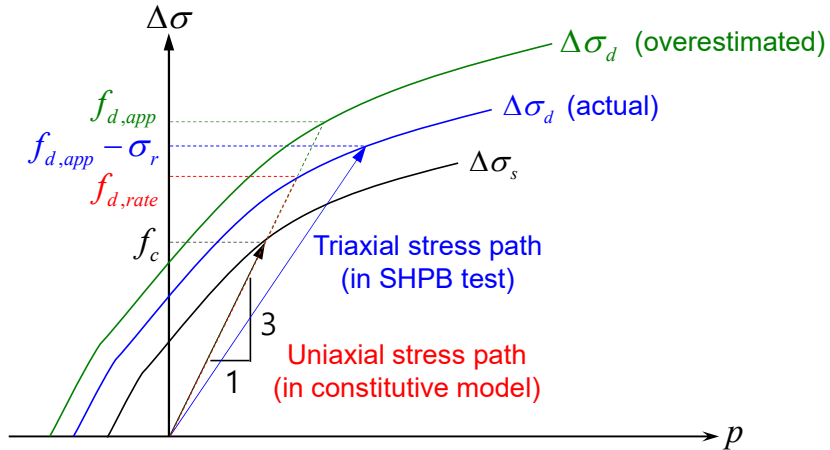


Figure 2.2 Overestimated dynamic failure surface with the apparent DIF

2.2. Previous studies on implementation of DIF

Some previous studies intended to solve the problem of the conventional SHPB tests. In this section, these studies were reviewed, and their limitations were discussed.

2.2.1. Fang and Wu (2017)

Fang and Wu (2017) systematically reviewed recent studies about concrete structures subjected to projectile and aircraft impacts in their book. In the chapter about numerical simulations, they pointed out that the strain rate for a DIF model in dynamic material tests differs from that in constitutive models, and suggested conversion factors of axial strain rate to effective strain rates using Equations (2.19)–(2.22). In the deriving process, Drucker-Prager model and fractionally associated flow rule were assumed.

$$\frac{\dot{\epsilon}_{eff}}{\dot{\epsilon}_x} = \sqrt{\frac{2}{3} \left[1 + 2 \left\{ (1 - \beta) \left(\frac{-3 - 2\omega\xi}{6 - 2\omega\xi} \right) - \nu\beta \right\}^2 \right]} \quad (2.19)$$

$$\frac{\dot{\epsilon}_{eff}^p}{\dot{\epsilon}_x} = \sqrt{\frac{2}{3} \left[1 + 2 \left(\frac{-3 - 2\omega\xi}{6 - 2\omega\xi} \right)^2 \right]} (1 - \beta) \quad (2.20)$$

$$\frac{\dot{\epsilon}_{eff}}{\dot{\epsilon}_x} = \frac{2}{3} \left[1 - \left\{ (1 - \beta) \left(\frac{-3 - 2\omega\xi}{6 - 2\omega\xi} \right) - \nu\beta \right\} \right] \quad (2.21)$$

$$\frac{\dot{\epsilon}_{eff}^p}{\dot{\epsilon}_x} = \frac{2}{3} \left[1 - \left(\frac{-3 - 2\omega\xi}{6 - 2\omega\xi} \right) \right] (1 - \beta) \quad (2.22)$$

where β is hardening or softening parameter; ν is Poisson's ratio; ξ denotes the slope of Drucker-Prager model; and ω means associativity parameter.

However, the uniaxial stress state was assumed for deriving the above conversion factors, but the assumption is violated in the SHPB test due to inertial effects. Therefore, it is difficult to apply these conversion factors to DIF models obtained from conventional SHPB tests. Moreover, these factors have a limitation that they can be only used for a linear failure surface model that is effective in a narrow pressure region.

2.2.2. Lu and Li (2011)

Lu and Li (2011) conducted a numerical study to suggest correction methodology of the apparent DIF. They performed FEA on SHPB tests for mortar, concrete and limestone specimens, and compared the FEA results with test results. Then, the input DIF was adjusted for the predictive accuracy to be improved. This procedure was iteratively conducted until the discrepancy between the analysis and test results became acceptable, as shown in Figure 2.3. However, this methodology has limitations: it is a too time-consuming procedure and an indirect method using FEA that essentially needs various assumptions about other material behaviors.

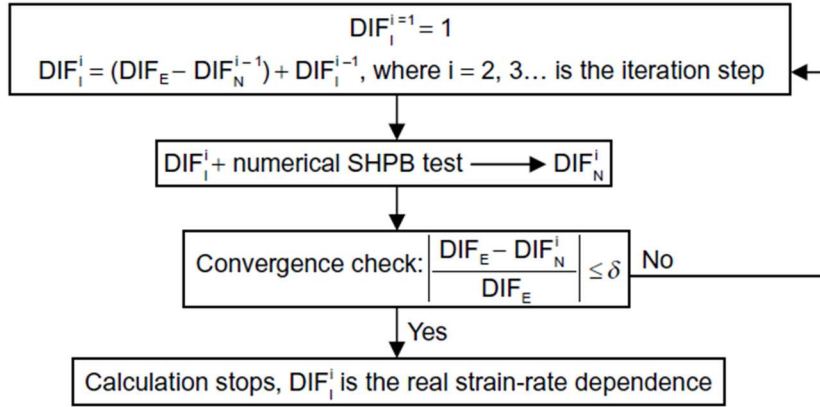


Figure 2.3 Apparent DIF correction procedure proposed by Lu and Li (2011)

2.2.3. Xu and Wen (2013)

Xu and Wen (2013) proposed semi-empirical formula of the pure rate DIF. First of all, the tensile DIF model was suggested based on the DIF data of tensile strength, considering that the dynamic tensile strength enhancement is inherent material property rather than structural effects such as inertial effects, as shown in Equation (2.23).

$$\gamma_t = \left\{ \left[\tanh \left(\left(\log_{10} \frac{\dot{\varepsilon}}{\dot{\varepsilon}_0} - W_x \right) S \right) \right] \left[\frac{F_m}{W_y} - 1 \right] + 1 \right\} W_y \quad (2.23)$$

where γ_t denotes the tensile DIF; $F_m = 10$ is the upper limit of the DIF model; $W_y = (F_m + 1) / 2$ is a coefficient related to the lower limit; $W_x = 1.6$ is a coefficient related to the location of the inflection point; $S = 0.8$ is a coefficient related to the slope; and $\dot{\varepsilon}_0 = 1 \text{ s}^{-1}$ is a reference strain rate. Then, they assumed that the enhancement of compressive strength due to the strain-

rate effect is equal to that of tensile strength. With the assumption, the pure rate DIF model can be expressed using Equation (2.24).

$$\gamma_{rate} = (\gamma_t - 1) \frac{f_t}{f_c} + 1 \quad (2.24)$$

where f_t denotes static tensile strength.

However, the assumption of the same strength enhancement in compression and tension was not verified, and any basis was not provided. Therefore, further investigations are necessary regarding the assumption.

2.2.4. Lee et al. (2018)

Lee et al. (2018) suggested a correction methodology of the conventional SHPB test data and proposed the pure rate DIF model. Firstly, they investigated key factors inducing inertial effects using a linear elastic analytical model, and suggested the inertial effects using Equation (2.25), as follows;

$$\Delta f_{inertial} = k_2 \rho_s d_s^2 \ddot{\epsilon}_x^{eng} + k_3 \rho_s l_s^2 \ddot{\epsilon}_x^{eng} \quad (2.25)$$

where $\Delta f_{inertial}$ is the strength enhancement due to inertial effects; k_2 and k_3 denote coefficients related to lateral and axial inertial effects, respectively; d_s and l_s mean initial diameter and length of a specimen; ρ_s is a density of a specimen; and $\ddot{\epsilon}_x^{eng}$ is engineering axial strain acceleration of a specimen. Then, they suggested the apparent DIF model using Equation (2.26); here, a

power function was selected as the pure rate DIF model, as shown in Equation (2.27).

$$\gamma_{app} = \gamma_{rate} + k_2 \frac{\rho_s d_s^2 \ddot{\epsilon}_x^{eng}}{f_c} + k_3 \frac{\rho_s l_s^2 \ddot{\epsilon}_x^{eng}}{f_c} \quad (2.26)$$

$$\gamma_{rate} = \left(\frac{\dot{\epsilon}_x^{eng}}{\dot{\epsilon}_0} \right)^{k_1} \quad (2.27)$$

where k_1 is a coefficient related to the strain-rate effect. The reference strain rate ($\dot{\epsilon}_0$) was 10^{-5} s^{-1} . From regression analysis, the coefficients were determined: $k_1 = 0.0147$, $k_2 = 0.3501$ and $k_3 = 0.4100$.

However, this methodology has some limitations. First, the linear elastic model was used for the derivation of inertial effects, but there is a gap between this assumption and a real concrete specimen. Furthermore, specimens of various sizes should be tested to accurately assess the coefficients related to inertial effects, which is sometimes difficult due to the aggregate size or apparatus size. Most of all, even though the regression analysis results strongly depend on the selected pure rate DIF model, it is difficult to assess how the pure rate DIF data is distributed from the conventional SHPB test.

2.2.5. Liu and Li (2019)

Liu and Li (2019) performed a numerical study to investigate the triaxiality of specimens in the SHPB tests and its effect on the test results. As

seen in Figure 2.4, they showed that the confining effect is responsible for the dynamic strength enhancement. Based on the results, they suggested that the static and dynamic strengths should be evaluated based on the uniaxial strain path to obtain the pure rate DIF, as indicated from the line OB in Figure 2.5. However, the experimental work was not conducted, and the pure rate DIF data of concrete compressive strength was not provided.

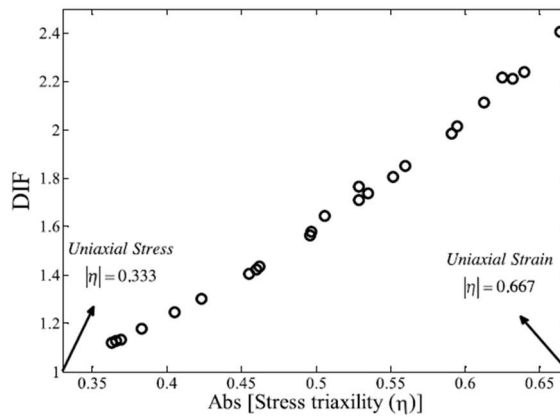


Figure 2.4 DIF versus stress triaxiality (Liu and Li, 2019)

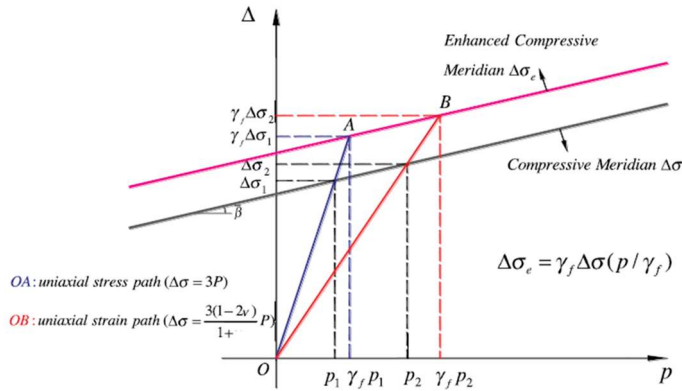


Figure 2.5 Strength enhancement along uniaxial stress and strain paths based on Drucker-Prager model (Liu and Li, 2019)

2.3. Previous studies on confined SHPB test

The confined SHPB test is the dynamic quasi-uniaxial strain test, also known as the dynamic quasi-oedometric test, and it has been employed to investigate the dynamic behavior of materials subjected to multi-axial stress states. In this test, a specimen is loaded in the axial direction within a confining steel ring that has the inner diameter same as the specimen diameter. Figure 2.6 shows specimens, steel disks (compression plugs) and the steel ring for the confined SHPB test of Forquin et al. (2015). During the test, the specimen is passively confined by the steel ring, and the lateral deformation is minimized, thereby being able to neglect the inertial effects (Forquin et al., 2008). Therefore, the strain rate and stress states are expressed using Equations (2.28) and (2.29) with the assumption of the circumferential stress equal to radial stress.

$$\dot{\boldsymbol{\epsilon}} = \begin{bmatrix} \dot{\epsilon}_x & 0 & 0 \\ 0 & 0 & 0 \\ 0 & 0 & 0 \end{bmatrix} \quad (2.28)$$

$$\boldsymbol{\sigma} = \begin{bmatrix} \sigma_x & 0 & 0 \\ 0 & \sigma_r & 0 \\ 0 & 0 & \sigma_r \end{bmatrix} \quad (2.29)$$

In the test, strain gauges are attached to the external surface of the steel ring to measure circumferential strain, and the strain signals of the steel ring are converted to the radial stress of the specimen. Therefore, all strain rate and

stress components can be measured in the confined SHPB test, which makes it possible to solve the problem of the conventional SHPB test.

In this section, the previous studies performing confined SHPB tests for concrete or mortar specimens were reviewed, and their limitations were discussed.



Figure 2.6 Specimens, steel disks and steel ring (Forquin et al., 2015)

2.3.1. Gong and Malvern (1990)

Using the confined SHPB test technique, Gong and Malvern (1990) investigated permanent deformation and residual static strength of concrete experiencing dynamic multi-axial loadings. Figure 2.7 shows the test setup of Gong and Malvern (1990). Firstly, the confined SHPB tests were performed with concrete specimens, and subsequently, static compressive tests were conducted with impact-damaged specimens. Against expectation, the test results indicated that the residual strength of specimens suffering low-velocity

impact was larger than the compressive strength of intact specimens. However, the residual strength decreased as the impact velocity increased. In addition, it was confirmed that the permanent deformation increased as impact velocity increased.

However, Gong and Malvern (1990) was focused on the residual strength and deformation rather than the strain-rate effect, and it is difficult to apply the findings to assess the pure rate DIF.

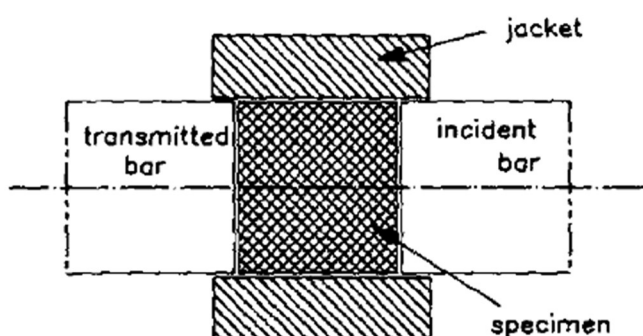


Figure 2.7 Test configuration of Gong and Malvern (1990)

2.3.2. Forquin et al. (2008)

Forquin et al. (2008) developed and established the confined SHPB test technique with mortar specimens. Figure 2.8 shows the specimen cell configuration. They proposed the specimen preparing method using epoxy resin. Through numerical analysis, they suggested the calculation method of the radial stress and strain of a specimen from the circumferential strain of the steel ring when there was plastic deformation in the steel ring. Furthermore, the frictional effects were numerically investigated, and it was found that the

friction had a limited influence with a frictional coefficient of less than 0.1. Verification tests for three mortar specimens were conducted, and the dynamic deviatoric and hydrostatic behaviors were investigated, as shown in Figure 2.9.

However, the main objective was not the investigation into the strain-rate effect of concrete (or mortar) but establishment of the test technique, and the test cases were too limited. Therefore, the pure rate DIF model cannot be drawn from the results of Forquin et al. (2008).

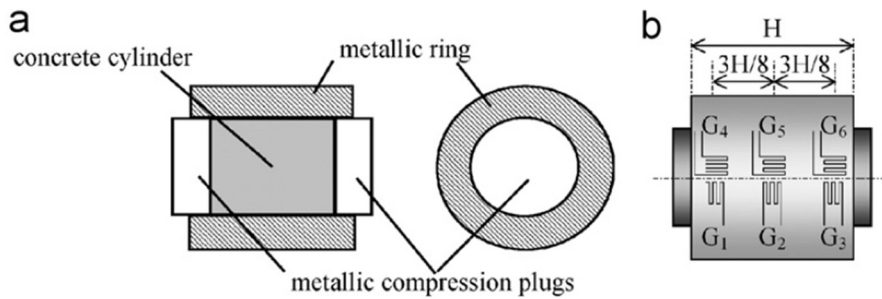


Figure 2.8 Specimen cell configuration of Forquin et al. (2008)

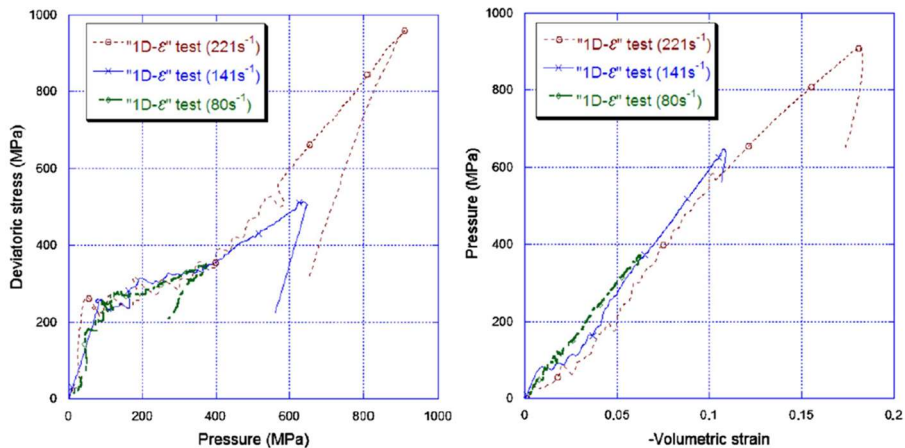
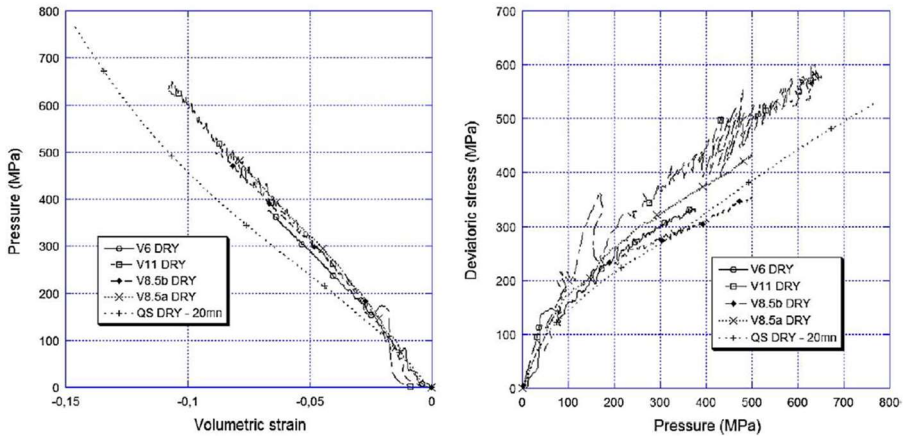


Figure 2.9 Test results of Forquin et al. (2008)

2.3.3. Forquin et al. (2010)

Forquin et al. (2010) investigated the effect of free water on the static and dynamic behaviors of mortar subjected to lateral confinements, employing the test technique suggested by Forquin et al. (2008). The water content and strain rate were considered variables, and the hydrostatic and deviatoric behaviors of specimens were observed, as shown in Figure 2.10. From the test results, it was found that the behavior of dried specimens was relatively independent of the strain rates whereas that of wet specimens changed depending on the strain rates, which means that the free water strongly affected the strain-rate sensitivity.

However, Forquin et al. (2010) was focused on the effect of free water, and any DIF or methodology to assess DIF was not addressed. Therefore, further investigation is necessary to evaluate the pure rate DIF for FEA.



(a)

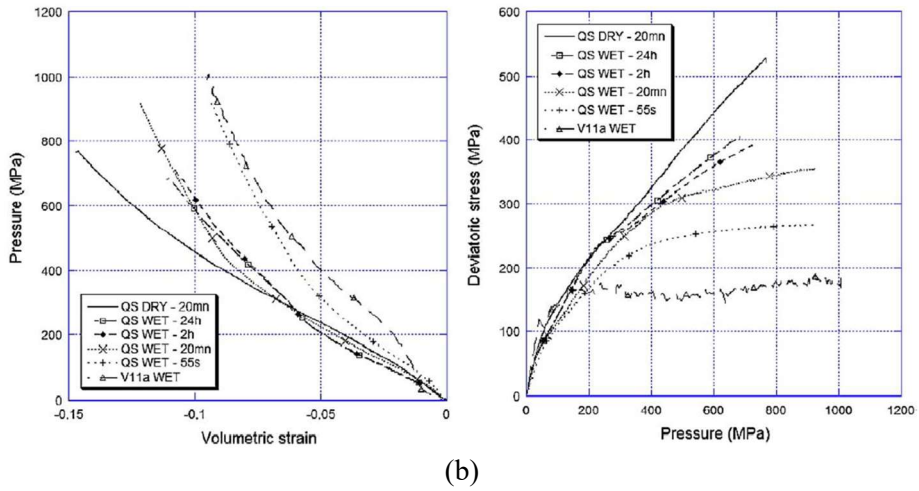


Figure 2.10 Test results of Forquin et al. (2010); (a) Dried specimens;
(b) Water-saturated specimens

2.3.4. Forquin et al. (2015)

In a similar way to Forquin et al. (2010), Forquin et al. (2015) performed the confined SHPB tests for concrete specimens with water content as a variable, and compared the results with the test results in Forquin et al. (2010). The test results showed a similar tendency to Forquin et al. (2010): water content strongly affected both hydrostatic and deviatoric behaviors of specimens, as shown in Figure 2.11.

However, the findings of Forquin et al. (2015) were insufficient to derive a DIF model for the same reasons as Forquin et al. (2010).

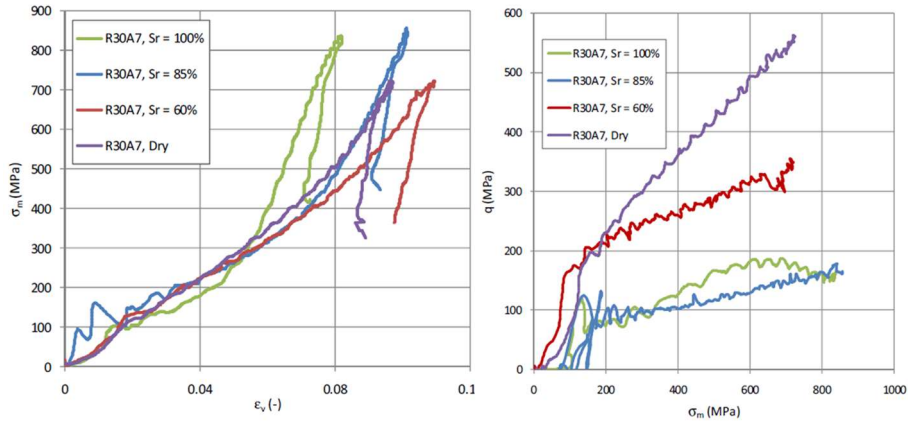


Figure 2.11 Test results of Forquin et al. (2015)

2.3.5. Piotrowska et al. (2016)

Piotrowska et al. (2016) investigated the effects of loading path and coarse aggregate type on the dynamic behaviors of concrete under multi-axial stress states. Two types of coarse aggregates were used for the fabrication of specimens: siliceous aggregates and limestone aggregates. Triaxial compressive tests and quasi-oedometric tests were conducted to figure out the loading path effect in the static state, and dynamic quasi-oedometric compressive tests were also conducted using an SHPB to investigate the dynamic behavior. In a similar manner to other previous studies (Forquin et al., 2008; Forquin et al., 2010; Forquin et al., 2015), the hydrostatic and deviatoric behaviors of concrete were assessed as shown in Figure 2.12. They reported that concrete with siliceous aggregates showed considerable compaction in the static quasi-oedometric tests compared to the static triaxial tests whereas concrete with limestone aggregates did not show a significant difference. On the other hand, the deviatoric strength of both concretes was

reduced in quasi-oedometric tests compared to triaxial tests, and limestone aggregate concrete showed severe strength reduction compared with siliceous aggregate concrete. Moreover, dynamic quasi-oedometric tests indicated that volumetric stiffness and deviatoric strength increased as strain rate increased, and the strength enhancement of limestone aggregated concrete was more significant compared to siliceous aggregate concrete.

However, as described above, Piotrowska et al. (2016) investigated only loading path and aggregate effects, and they did not address the DIF of concrete compressive strength.

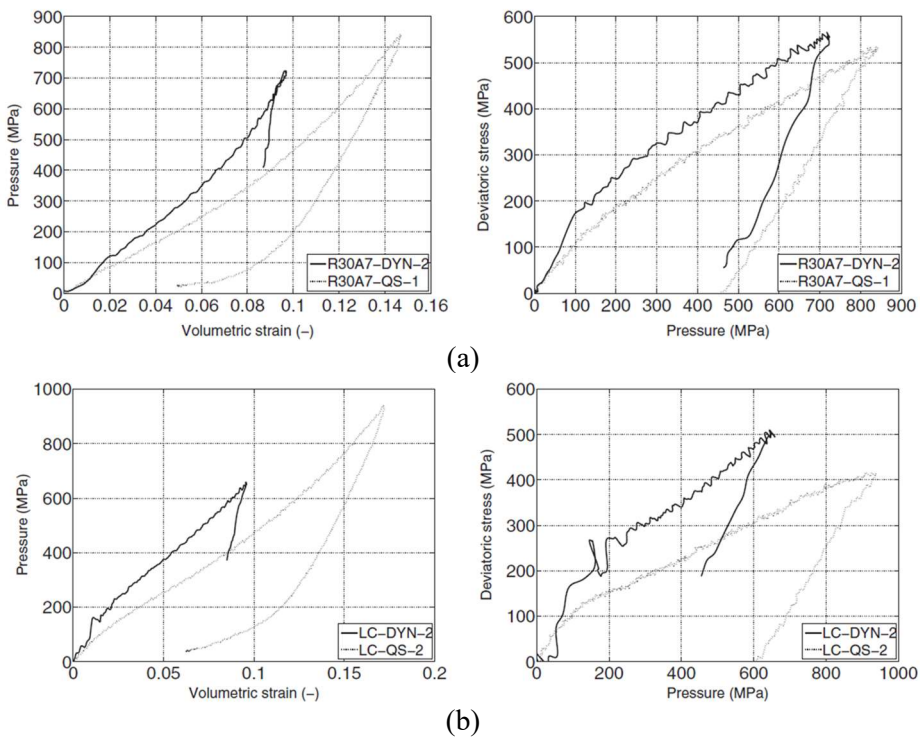


Figure 2.12 Test results of Piotrowska et al. (2016); (a) Concrete with siliceous aggregates; (b) Concrete with limestone aggregates

2.4. Concluding remarks

As discussed in Section 2.1, even though lateral strain rates and stresses are always generated in the conventional SHPB tests, only axial strain rate and stress are measured in the tests, thereby resulting in insufficient information about strain rates and stresses. This limitation makes it difficult to use the DIF models obtained from the conventional SHPB tests for FEA.

Various attempts have been made to overcome this limitation and to propose an appropriate pure rate DIF model, as described in Section 2.2. However, the previous studies in Section 2.2 indirectly estimated the effective strain rate or the pure rate DIF with various assumptions that were somewhat far from the actual conditions or that were not verified. Therefore, it was necessary to evaluate the pure rate DIF–effective strain rate relationship through experimental work to consider the actual states of concrete at high strain rates.

The confined SHPB test technique can be a solution to the problem of the conventional SHPB test since all strain rate and stress components can be measured in the test. However, the literature review in Section 2.3 indicated that the previous studies on confined SHPB tests hardly pay attention to the DIF and the relevant studies are extremely limited. Accordingly, research to investigate the pure rate DIF of concrete through the confined SHPB test has been hardly conducted until now, and the methodology for assessment of the pure rate DIF has not been established.

Therefore, to address the limitations discussed in Chapter 2, this study attempted to propose the pure rate DIF model through the concrete confined SHPB test. As a first step, in the following chapter, the dynamic compressive behavior of concrete subjected to lateral constraints was numerically investigated to suggest and verify the methodology for evaluation of the pure rate DIF in the confined SHPB test.

3. Methodology for Evaluation of Pure Rate DIF

3.1. Numerical analysis on confined SHPB test

To investigate the behavior of a concrete specimen in the confined SHPB test, numerical analysis was conducted using LS-DYNA, an FEA software specialized for explicit impact analysis. In this chapter, the methodology for evaluating the pure rate DIF was suggested and verified based on the FEA results.

3.1.1. Establishment of numerical model

3.1.1.1. Modeling part and boundary conditions

A high rate compressive behavior of a concrete specimen subjected to the lateral constraints was investigated to analyze the specimen behavior in the confined SHPB test. As shown in Figure 3.1, a cylinder specimen of $D50 \times L50$ mm was modeled using 2 mm eight-node solid elements with the reduced integration (ELFORM=1). For the uniaxial strain state, the nodes on the circumferential surface were constrained in the y and z-axis directions, and the reaction end (back end) of the specimen was constrained in the x-axis direction. Then, the prescribed motions were input to the nodes of the loaded end (front end) for high rate compression. The prescribed nodal velocities are shown in Figure 3.2; here, V in the legend denotes the peak deformation velocity in a unit of m/s.

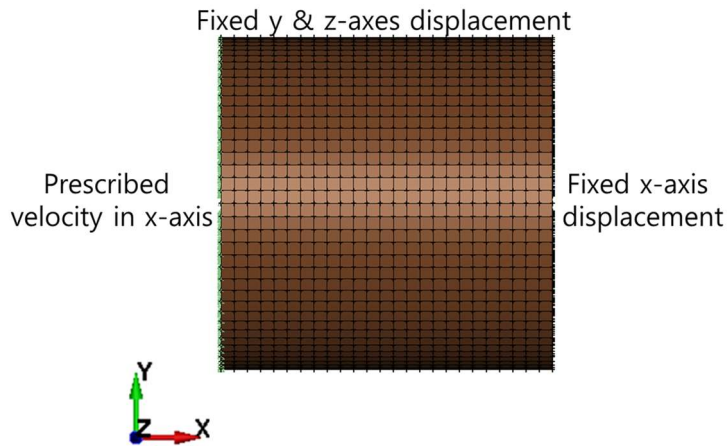


Figure 3.1 Specimen model and boundary conditions

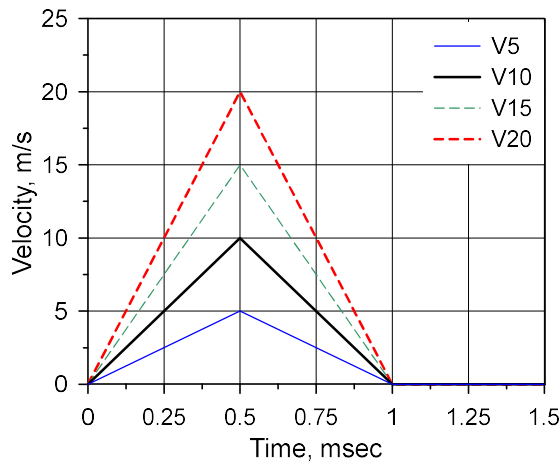


Figure 3.2 Prescribed nodal velocity in the x-axis direction on the loaded end

3.1.1.2. Concrete specimen

The KCC model (MAT 72R3) is one of the most widely used concrete constitutive models for FEA on concrete structures under impact and blast loadings, and the KCC model can capture various characteristics of concrete behavior, such as the pressure-dependency, lode-angle-dependency, and

strain-rate-dependency. Moreover, the KCC model has the advantage that a DIF model ($\gamma_{rate} - \dot{\epsilon}_{eff}$ curve) can be input using a user-defined curve. In this model, the DIF is used for enhancing the failure surfaces and delaying damage accumulation. Therefore, this study selected the KCC model as the concrete constitutive model.

The compressive strength of the specimen was assumed as 40 MPa that is usually used at construction sites of social infrastructures. The density and Poisson's ratio were assumed to be 2300 kg/m³ and 0.18, respectively. The model parameters and equation of state (EOS) were determined as the auto-generating or recommended values referring to Wu and Crawford (2015). Tables 3.1 and 3.2 show the input model parameters. The tabulated compaction model (EOS 8) was used for the EOS model, and the EOS parameters are listed in Table 3.3; here, ϵ_v and K_u denote volumetric strain and unloading bulk modulus.

The pure rate DIF model proposed by Lee et al. (2018) was determined as an input DIF model in compression, and the tensile DIF model of fib MC2010 (fib bulletin 65, 2012) was used in tension. In addition to the strain-rate-dependent cases, the strain-rate-independent case of V10 was also analyzed for purpose of comparison; in this case, both DIFs in compression and tension were not considered. Since the mesh distortion was not severe in this FEA, no erosion criterion was used for this analysis.

Table 3.1 Concrete model parameter details (unit: ton, mm, sec)

Description	Symbol	Parameter value
Density	ρ_s	2.3×10^{-9}
Poisson's ratio	ν_s	0.18
Uniaxial tensile strength	f_t	3.54
Maximum failure surface parameters	a_0	11.8150
	a_1	0.4463
	a_2	0.002021
Yield failure surface parameters	$a_{0,y}$	8.9251
	$a_{1,y}$	0.6250
	$a_{2,y}$	0.006442
Residual failure surface parameters	$a_{1,f}$	0.4417
	$a_{2,f}$	0.002960
Associativity parameter	ω	0.5
Localization width	w_{lz}	39
Damage scaling factors	b_1	0.8170
	b_2	1.6496
	b_3	1.15

Table 3.2 Default yield scale factor (η)–damage function (λ) relationship

λ	η
0	0
8.0×10^{-6}	0.85
2.4×10^{-5}	0.97
4.0×10^{-5}	0.99
5.6×10^{-5}	1
7.2×10^{-5}	0.99
8.8×10^{-5}	0.97
3.2×10^{-4}	0.5
5.2×10^{-4}	0.1
5.7×10^{-4}	0

Table 3.3 EOS model parameters

ε_v	p , MPa	K_u , MPa
0	0	16088
-0.0015	24	16088
-0.0043	53	16314
-0.0101	84	17130
-0.0305	160	20387
-0.0513	242	23645
-0.0726	343	26902
-0.0943	525	29361
-0.174	3067	66053
-0.208	4692	80442

3.1.2. Data-processing procedure

The FEA data was sampled with a sampling rate of 1 MHz. Engineering axial stress (σ_x^{eng}) and strain (ε_x^{eng}) of the specimen were obtained using Equations (3.1) and (3.2); where F_{front} and F_{back} denote the nodal forces on the front and back ends of the specimen, respectively; u_{front} and u_{back} are nodal displacements on front and back ends of the specimen, respectively; and N_{node} is the number of nodes on an end of the specimen.

$$\sigma_x^{eng} = \frac{1}{2A_s} \left(\sum_{node} F_{front} + \sum_{node} F_{back} \right) \quad (3.1)$$

$$\varepsilon_x^{eng} = \frac{1}{l_s N_{node}} \left(\sum_{node} u_{front} - \sum_{node} u_{back} \right) \quad (3.2)$$

As shown in Equation (3.3), true axial strain rate ($\dot{\varepsilon}_x$) was obtained using central difference of true axial strain (ε_x) that was converted from engineering axial strain (ε_x^{eng}); here, the subscript i means the i -th time step; and Δt is the constant time step between the i -th and $(i+1)$ -th steps. Then, the effective deviatoric strain rate ($\dot{\varepsilon}_{eff}$) can be calculated using Equation (3.4).

$$\dot{\varepsilon}_{x,i} = \frac{\varepsilon_{x,i+1} - \varepsilon_{x,i-1}}{2\Delta t} \quad (3.3)$$

$$\dot{\varepsilon}_{eff} = \sqrt{\frac{2}{3} \dot{\varepsilon}_{ij} \dot{\varepsilon}_{ij}} = \frac{2}{3} \dot{\varepsilon}_x \quad (3.4)$$

The average loading path (p , $\Delta\sigma$) was determined using Equations (3.5) and (3.6); where $N_{element}$ is the number of elements of the specimen part.

$$p = \frac{1}{N_{element}} \sum_{element} p \quad (3.5)$$

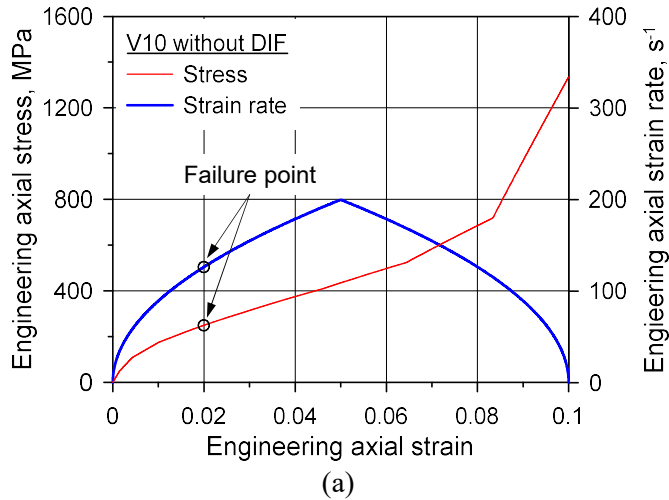
$$\Delta\sigma = \frac{1}{N_{element}} \sum_{element} \Delta\sigma \quad (3.6)$$

3.1.3. Numerical analysis results

3.1.3.1. Strain-rate-independent case

Figure 3.3 shows the FEA results of the strain-rate-independent case of V10. As shown in Figure 3.3 (a), the axial stress of concrete continuously increased, so any distinct point that can be defined as a failure point, such as a strength point, was not observed in the axial stress–strain curve. On the

other hand, the failure point can be clearly defined with the loading path and static maximum failure surface. As shown in Figure 3.3 (b), the stress increased initially along the uniaxial strain path, resulting from the lateral confinements. As the stress state approached the static failure surface, the triaxiality, which is defined as $p/\Delta\sigma$, gradually increased. Finally, the loading path was in contact with the static failure surface at a point. After the contact, the loading path showed the continuously increasing tendency below the static failure surface, resulting in a continuous increase in the axial stress. Therefore, the failure point in the loading path can be determined as the contact point, and the failure point in the axial stress–strain curve can be also determined as a corresponding point, as shown in Figure 3.3 (a).



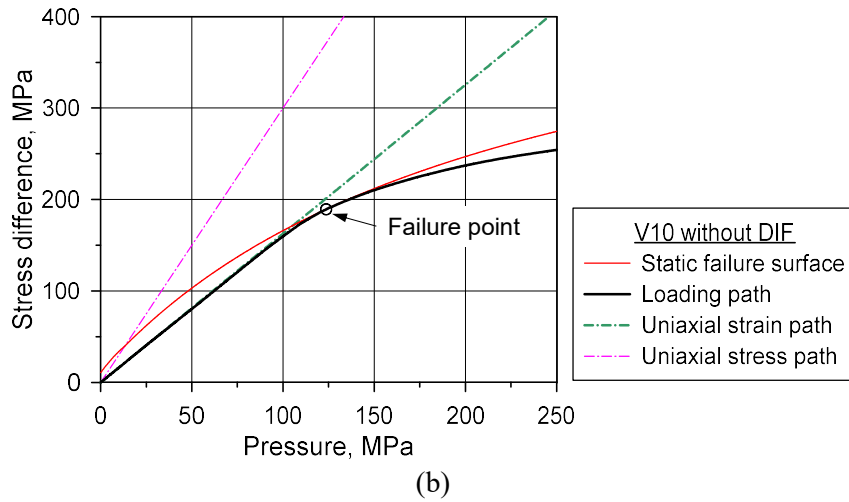


Figure 3.3 FEA results of the strain-rate-independent case (V10); (a) Axial stress–strain relationship; (b) Loading path

3.1.3.2. Strain-rate-dependent case

The axial stress–strain curves of the strain-rate-dependent cases showed the same tendency as that of the strain-rate-independent case, as shown in Figure 3.4 (a). The distinction of a failure point was difficult with only the axial stress–strain curve. Figure 3.4 (b) shows the loading path and static maximum failure surface of the strain-rate-dependent case of V10. The stress increased initially along the uniaxial strain path, similarly to the strain-rate-independent case. However, the loading path crossed over the static failure surface because the strength was enhanced due to the strain-rate effect. Then, gradual increases in the triaxiality and stress were observed.

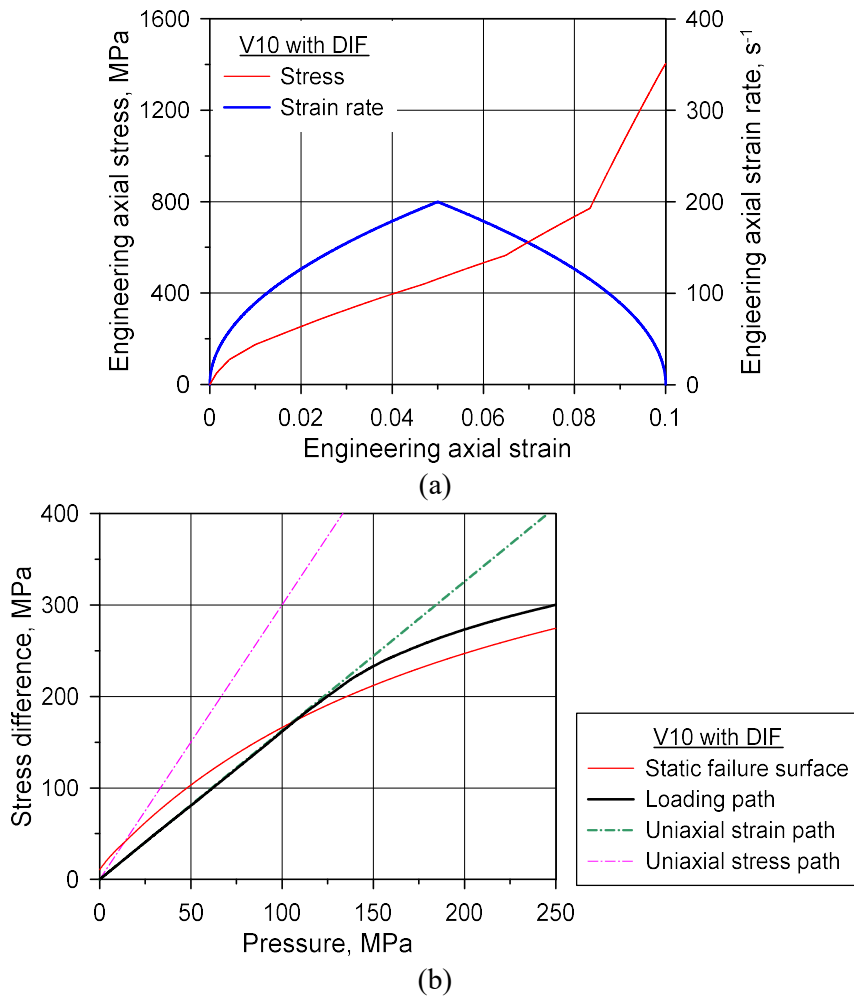


Figure 3.4 FEA results of the strain-rate-dependent case (V10); (a) Axial stress-strain relationship; (b) Loading path

3.2. Methodology for evaluation of pure rate DIF

From an observation of the specimen behavior of the strain-rate-independent case, the following assumptions can be drawn.

- (1) The loading path should be in contact with the failure surface at a point, and the contact point is the failure point.
- (2) Except for the failure point, the stress state of the specimen should be below the failure surface.

For the strain-rate-dependent cases, the above assumptions can be mathematically expressed using Equation (3.7); here, p_f is the pressure value at the failure point.

$$\begin{cases} \Delta\sigma_d(\gamma_{rate}, p) = \Delta\sigma(p) & \text{for } p = p_f \\ \Delta\sigma_d(\gamma_{rate}, p) < \Delta\sigma(p) & \text{for } p \neq p_f \end{cases} \quad (3.7)$$

Meanwhile, in the KCC model that was used for the FEA in this chapter, the dynamic maximum failure surface is enhanced using Equation (3.8) (Malvar et al., 1997; Kong et al., 2017).

$$\Delta\sigma_d(\gamma_{rate}, p) = \gamma_{rate} \Delta\sigma_s(p / \gamma_{rate}) \quad (3.8)$$

Therefore, the pure rate DIF can be determined as the value making the dynamic failure surface satisfy Equations (3.7) and (3.8). Figure 3.5 shows the procedure to obtain the pure rate DIF based on the bisection method. In the figure, the subscript i means the i -th trial. Then, the failure point and

corresponding strain rate can be also determined from the contact point and the data at the corresponding time.

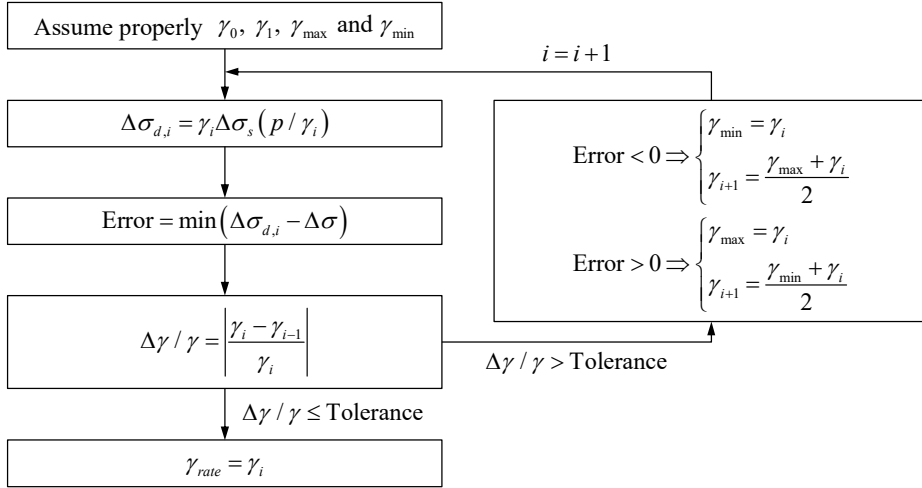


Figure 3.5 Procedure for evaluating the pure rate DIF

Figure 3.6 shows the FEA results of the strain-rate-dependent case of V10 with the failure point and dynamic failure surface that were determined according to the procedure of Figure 3.5. As shown in Figure 3.6 (b), the loading path was in contact with the dynamic failure surface at the failure point, and other stress points were below the dynamic failure surface. For all strain-rate-dependent cases, the estimated pure rate DIF and effective deviatoric strain rate data is plotted in Figure 3.7 and listed in Table 3.4; here, γ_{input} and $\gamma_{\text{estimated}}$ denote input and estimated DIF values, respectively. The estimation results indicated that the input DIF was predicted with high accuracy (about 0.3% error), which means that the methodology for evaluating the pure rate DIF of this study was valid.

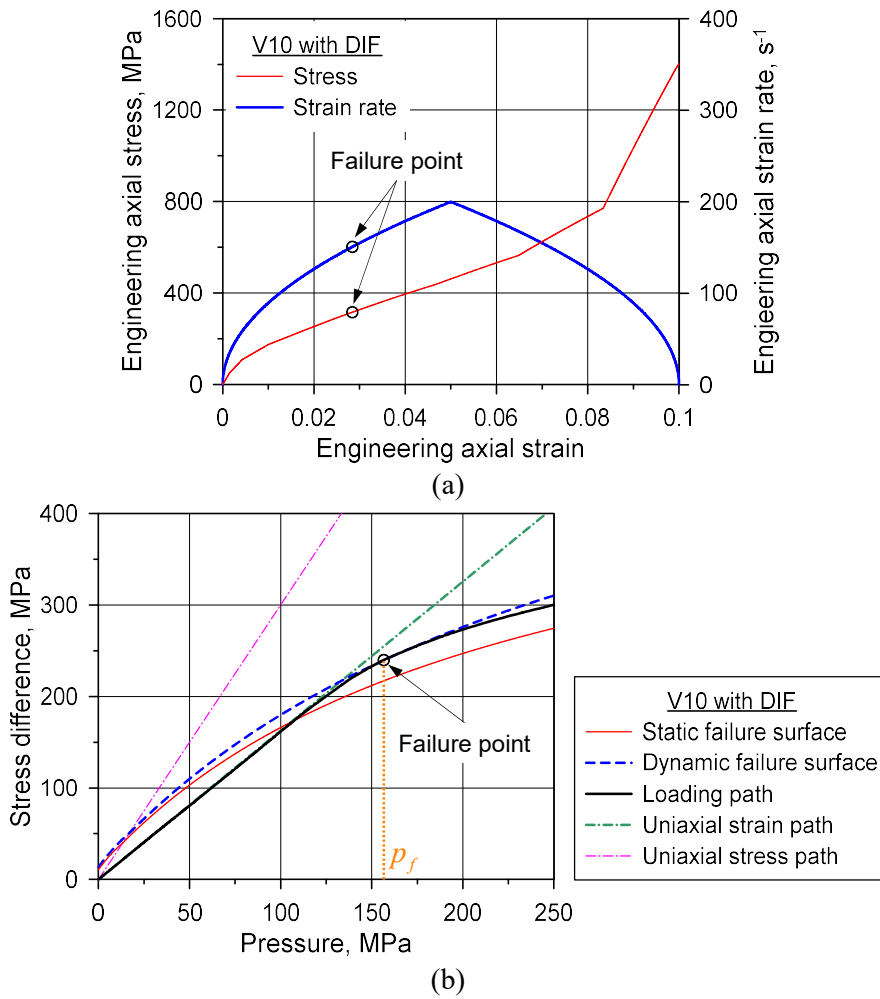


Figure 3.6 FEA results of the strain-rate-dependent case with the failure point (V10); (a) Axial stress–strain relationship; (b) Loading path

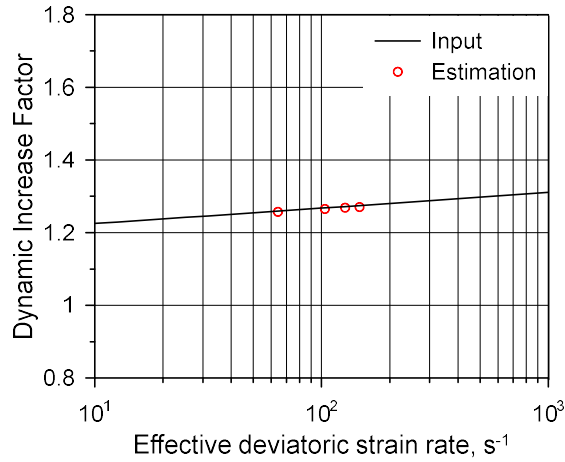


Figure 3.7 Comparison of the estimated DIF with the input DIF curve

Table 3.4 Estimation of the pure rate DIF

Case	$\dot{\epsilon}_x, s^{-1}$	$\dot{\epsilon}_{eff}, s^{-1}$	γ_{input} (1)	$\gamma_{estimated}$ (2)	Error [(2)-(1)]/(1)
V5	96.3	64.2	1.2591	1.2572	-0.15%
V10	155.2	103.4	1.2680	1.2651	-0.23%
V15	190.5	127.0	1.2718	1.2685	-0.26%
V20	220.7	147.1	1.2746	1.2704	-0.32%

If the input DIF model is changed, only the degree of strength enhancement will change, but the two observations on the loading path will be the same. Accordingly, the methodology to evaluate pure rate DIF can be derived in the same way. In conclusion, the accuracy of the input DIF model was not critical in this approach, and the conclusions of this chapter are valid regardless of the accuracy of the input DIF model.

3.3. Concluding remarks

In this chapter, the methodology for assessing the pure rate DIF was suggested based on the numerical analysis of the concrete confined SHPB test. The implementing procedure of the methodology using the bisection method is presented in Figure 3.5. The estimation of the input DIF through the suggested methodology showed good predictive accuracy, which means that this methodology was valid.

Therefore, the following chapter describes experimental work to obtain the actual pure rate DIF data applying the suggested methodology and to propose the pure rate DIF model. For acquisition of the pure rate DIF data, the static and dynamic confined tests were conducted using a universal testing machine and SHPB. Moreover, the conventional SHPB test was also performed for comparison of the apparent DIF to the pure rate DIF.

4. SHPB Test Program

4.1. Test variables

Two variables were considered in the experimental work: test technique and striker bar impact velocity. The confined SHPB test was performed to obtain the pure rate DIF data of concrete, and the conventional SHPB test was also conducted to be compared with the confined SHPB test. The impact velocity of the striker bar was determined to obtain data in the strain rate range ($10\text{--}200\text{ s}^{-1}$) representing the impact and blast loadings. In addition, the static test was also considered in the case of confined tests to determine the static failure surface of specimens. Figure 4.1 shows the designation of test cases. Six specimens were tested per one loading condition.

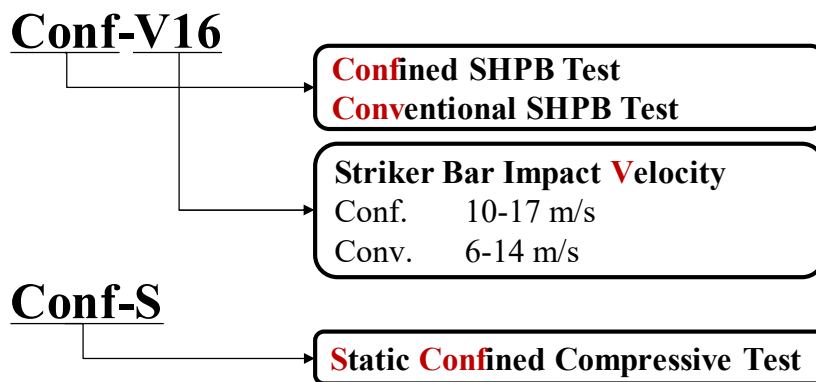


Figure 4.1 Designation of test cases

4.2. Specimen preparation

Specimens were fabricated according to ASTM C192 (2019). The mix proportion in Table 4.1 was used for fabrication and was aimed at compressive strength of 40 MPa that is usually used for social infrastructures. The maximum coarse aggregate size (G_{\max}) was determined as 13 mm, considering that the specimen dimension should be at least three times G_{\max} to minimize the variation of test data (Kim et al., 2019). Fresh concrete was placed in cylinder molds of D50×L100 mm. For the specimens of the confined tests, seamless molds were manufactured with the same tolerance (± 0.02 mm) as steel rings to ensure a snug fit, as shown in Figure 4.2. After the 37-day water curing, the middle part of the hardened specimen was sampled to D50×L50 mm by cutting both ends away. The maximum error of the perpendicularity was 0.26° which is considered acceptable (Kim et al., 2019; ASTM C39, 2020). The cut specimens were kept in plastic wrap until testing to minimize shrinkage that could cause a gap between a specimen and a steel ring. Figure 4.3 shows the fabricated specimens.

Table 4.1 Mix proportion of concrete specimens

Target strength, MPa	G_{\max} , mm	Unit weight, kg/m ³			
		Water	Cement	Fine aggregate	Coarse aggregate
40	13	179	459	661	1037



Figure 4.2 Seamless molds for specimens of confined tests



Figure 4.3 Fabricated specimens

According to ASTM C39 (2020), static compressive strength tests were conducted for six specimens of $D50 \times L100$ mm and six specimens of $D150 \times L300$ mm. The averaged test results are listed in Table 4.2. In this study, the static material properties were determined from the results of specimens of $D50 \times L100$ mm to minimize the size effect. However, because the Poisson's ratio of $D50 \times L100$ mm specimens was not obtained, that of $D150 \times L300$ mm specimens was used.

Table 4.2 Static material properties

Specimen	Compressive strength, MPa	Elastic modulus, MPa	Poisson's ratio	Density, kg/m ³
D50×L100	51.5	29965	-	2434
D150×L300	50.6	29660	0.1505	2426

4.3. Test procedures

In this section, the procedures of three kinds of tests were described: the conventional SHPB test, static confined compressive test (static quasi-oedometric test), and confined SHPB test. From the conventional SHPB test, the apparent DIF data was acquired. The static confined compressive test was conducted to determine the static failure surface, and the pure rate DIF was evaluated based on the static failure surface and the results of the confined SHPB test.

4.3.1. Conventional SHPB test

4.3.1.1. Test procedure

An SHPB of Extreme Performance Testing Center in Seoul National University was used for the conventional SHPB test. The geometrical and material properties of bar components are listed in Table 4.3. Figure 4.4 shows the SHPB apparatus.

Table 4.3 Characteristics of bar components

	Property	Value
Dimension	Diameter, mm	76.2
	Length, m	5.5
Material properties	Density, kg/m ³	7800
	Elastic modulus, GPa	210
	Poisson's ratio	0.29



Figure 4.4 SHPB apparatus

A striker bar of 600 mm was used to ensure sufficient loading duration, and impact velocities were determined as 6, 8, 10, 12, and 14 m/s to adjust strain rates. A pulse shaper should be used to prevent the dynamic non-equilibrium state of a specimen in the conventional SHPB test for concrete (Frew et al., 2002; Heard et al., 2014; Lee et al., 2018; Kim et al., 2019; Kim et al., 2022). In this study, annular pulse shapers made of C1020 copper were attached to the impact end of the incident bar using petroleum jelly, as shown in Figure 4.5 (a). The dimension of pulse shapers was determined as 52×48×4 mm based on preliminary tests.

Kim et al. (2022) suggested and verified a lubrication technique to remove the frictional effect in concrete SHPB tests. In accordance with Kim et al. (2022), both ends of the specimen were lubricated using polytetrafluoroethylene (PTFE) grease of 12 mg/cm² or more to minimize the frictional effect, as shown in Figure 4.5 (b). Then, the specimen was neatly sandwiched between the bar components as shown in Figure 4.5 (c), and it was loaded by the collision of the striker bar.

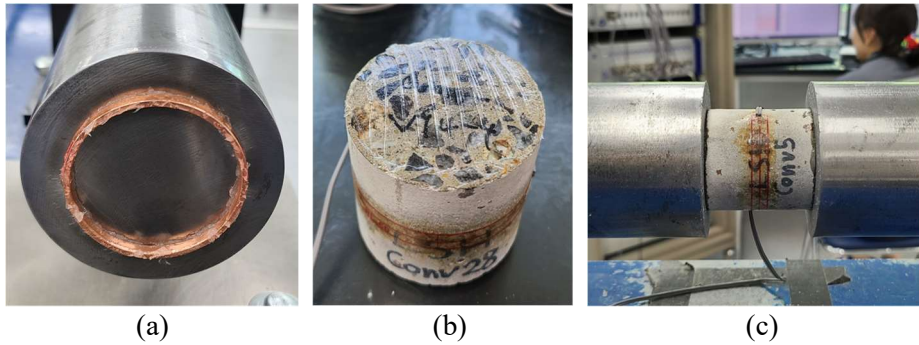


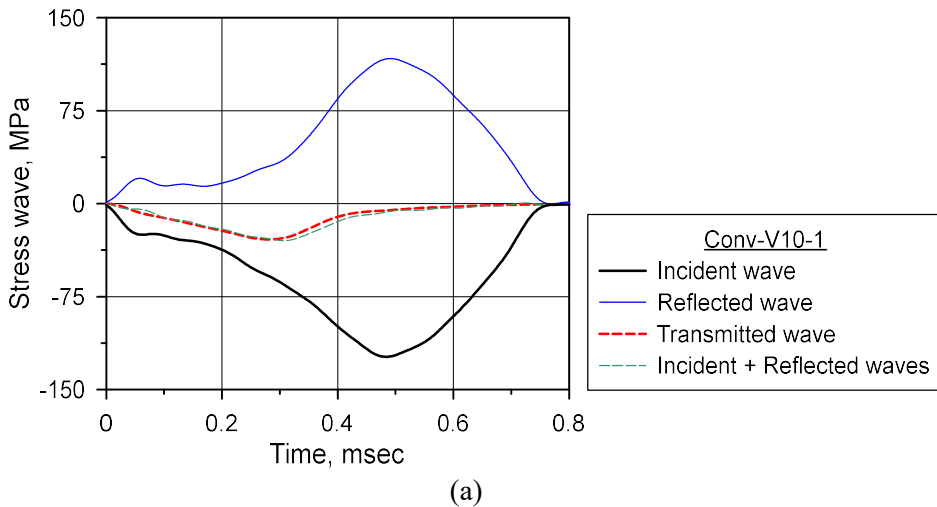
Figure 4.5 Conventional SHPB test setup; (a) Pulse shaper;
(b) Lubricated specimen; (c) Mounted specimen

4.3.1.2. Measurement and data-processing procedure

The test data was sampled with a sampling rate of 1 MHz. During the tests, the incident and reflected waves were measured from the strain gauges attached to the incident bar, and the transmitted wave was obtained from the strain gauges attached to the transmitted bar. Two strain gauges per each bar component were attached at 180° positions, and the results were averaged to cancel out trivial bending signals. Each strain signal was filtered using a low-pass filter with a cutoff frequency of 15 kHz to remove the high-frequency noises, similarly to Lee et al. (2018) and Kim et al. (2019). Figure 4.6 (a) shows the typical stress waves in the conventional SHPB test.

In addition, in order to calculate the effective deviatoric strain rate, a strain gauge of 60 mm gauge length was attached to the center of the specimen in the circumferential direction, as shown in Figure 4.5 (b) and (c). The circumferential strain of the specimen was filtered with a low-pass filter of a cutoff frequency of 50 kHz. Figure 4.6 (b) shows the typical strain of the specimen. As shown in the figure, the circumferential strain of specimens in

some test cases showed a relatively large value of about 0.007 level at the peak stress. Under these high strain values, the crack may cause a reliability issue in strain signals. As mentioned, however, the gauge length was 60 mm which was long enough to include cracks (about 40% of the circumference of a specimen); therefore, it was thought that the strain gauge was possible to measure appropriately the average strain of specimens, including the crack strain. Figure 4.7 exhibits the typical failure pattern of a specimen at the peak stress, which indicates that the cracks occurred across the strain gauge.



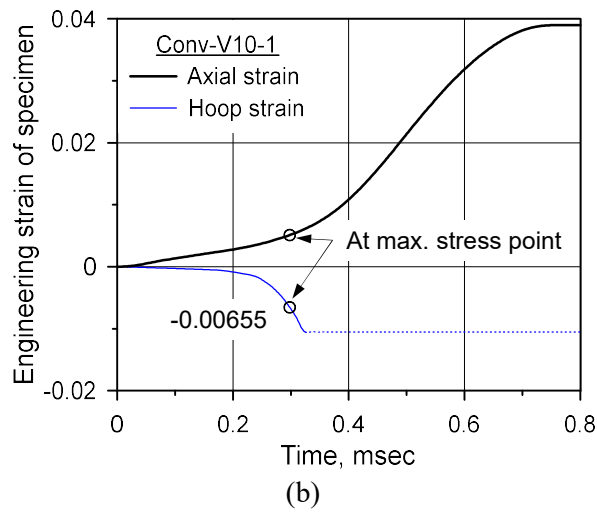


Figure 4.6 Typical test results of the conventional SHPB test (Conv-V10-1);

(a) Stress waves; (b) Strain of a specimen

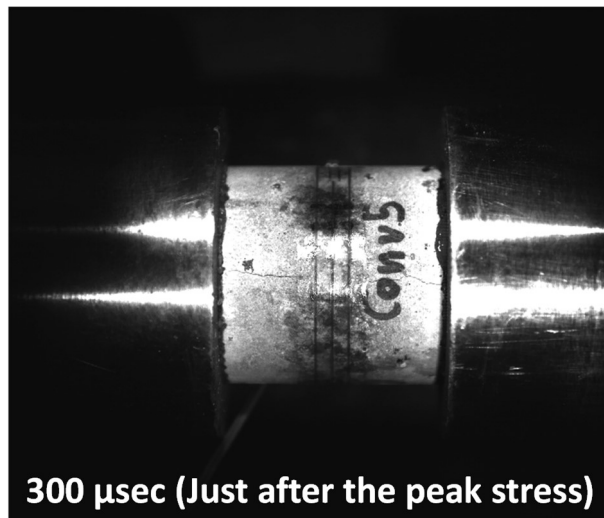


Figure 4.7 Typical failure pattern of a specimen at the peak stress point

(Conv-V10-1)

The axial stress and strain were calculated based on one-dimensional stress wave theory (Chen and Song, 2010), which is introduced in Section 2.1, as shown in Equations (4.1)–(4.3).

$$\sigma_x = \frac{A_b}{2A_s} E_b (\varepsilon_{incident} + \varepsilon_{reflect} + \varepsilon_{transmitted}) \quad (4.1)$$

$$\dot{\varepsilon}_x^{eng} = \frac{c_{1,b}}{l_s} (\varepsilon_{incident} - \varepsilon_{reflect} - \varepsilon_{transmitted}) \quad (4.2)$$

$$\varepsilon_x^{eng} = \frac{c_{1,b}}{l_s} \int_0^t (\varepsilon_{incident} - \varepsilon_{reflect} - \varepsilon_{transmitted}) d\tau \quad (4.3)$$

where σ_x is the average axial stress of the specimen; ε_x^{eng} and $\dot{\varepsilon}_x^{eng}$ are engineering axial strain and strain rate, respectively; $\varepsilon_{incident}$, $\varepsilon_{reflect}$ and $\varepsilon_{transmitted}$ denote the incident, reflected and transmitted strain waves, respectively; A_b , E_b and $c_{1,b}$ are the cross-sectional area, elastic modulus and wave propagation velocity of the bar components; A_s and l_s denote the initial cross-sectional area and length of the specimen, respectively; and t is time. Then, the engineering axial strain (ε_x^{eng}) was converted to the true axial strain (ε_x), and the true axial strain rate ($\dot{\varepsilon}_x$) was obtained using Equation (3.3). Moreover, the radial strain rate ($\dot{\varepsilon}_r$) was calculated using Equation (4.4) with the assumption that the circumferential strain (ε_θ) was equal to the radial strain (ε_r); this assumption is valid when the uniform deformation within a specimen is assumed, which is regarded as a fundamental rule in material tests.

$$\dot{\epsilon}_{r,i} = \frac{\epsilon_{r,i+1} - \epsilon_{r,i-1}}{2\Delta t} \quad (4.4)$$

Effective deviatoric strain rate ($\dot{\epsilon}_{eff}$) was calculated using Equation (4.5), as follows;

$$\dot{\epsilon}_{eff} = 2|\dot{\epsilon}_x - \dot{\epsilon}_r|/3 \quad (4.5)$$

The apparent DIF (γ_{app}) was obtained from static compressive strength (f_c) and the peak value of the dynamic axial stress (i.e., the apparent dynamic strength, $f_{d,app}$), as shown in Equation (4.6). The instantaneous strain rate value was also obtained at the corresponding time as shown in Figure 4.8.

$$\gamma_{app}(\dot{\epsilon}_{eff}) = \frac{f_{d,app}(\dot{\epsilon}_{eff})}{f_c} \quad (4.6)$$

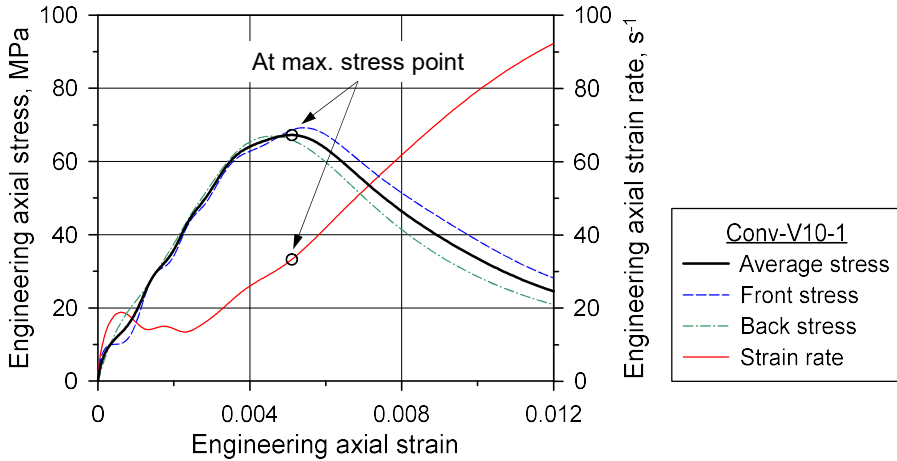


Figure 4.8 Typical axial stress–strain relationship and axial strain rate history in the conventional SHPB test (Conv-V10-1)

4.3.2. Static confined compressive test

4.3.2.1. Design of steel ring and disks

To ensure the quasi-uniaxial strain state of a specimen and to prevent plastic deformation of a steel ring, the steel ring of sufficient thickness and strength should be designed and manufactured for the confined tests. Moreover, proper steel disks were also necessary to appropriately apply the force to the specimen. F53 stainless steel of ASTM A182 (2020) was selected as a material for the steel ring and disks because it has a high yield strength (about 590 MPa). The coupon tests were conducted for three F53 specimens according to ASTM A370 (2019), and the averaged results are listed in Table 4.4.

Table 4.4 Material properties of the steel ring and disks

Density, kg/m ³	Proportional limit, MPa	0.2%-offset yield strength, MPa	Elastic modulus, GPa	Poisson's ratio
7800	400	592	184.3	0.2967

In the case of the steel ring, the thickness and length needed to be determined, as shown in Figure 4.9. The length of the steel ring was determined to be 54 mm to prevent the specimen and steel disks from coming out of the steel ring during tests.

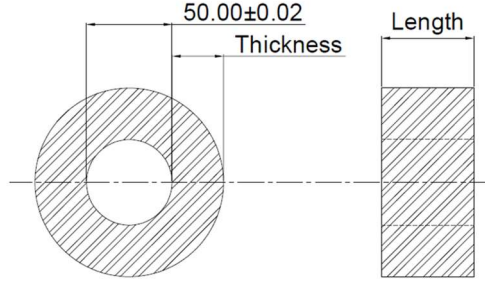


Figure 4.9 Schematic diagram of the steel ring (unit: mm)

Since the steel ring would be used for the confined SHPB test as well as the static confined compressive test, the behavior of the steel ring subjected to the high rate inner pressure should be investigated to determine the thickness of the steel ring. To calculate the inner pressure (i.e., the radial stress of a specimen, σ_r), the static elastic solution is used (Timoshenko and Goodier, 1987), as shown in Equation (4.7).

$$\sigma_r = -\frac{(r_{o,ring}^2 - r_{i,ring}^2)}{2r_{i,ring}^2} E_{ring} \varepsilon_{\theta,ring} \quad (4.7)$$

where $r_{o,ring}$ and $r_{i,ring}$ are the radii of outer and inner surfaces of the steel ring, respectively; E_{ring} is the elastic modulus of the steel ring; and $\varepsilon_{\theta,ring}$ is circumferential strain at the center on the outer surface of the steel ring. However, if the steel ring is too thick, the static elastic solution is not accurate due to inertial force. Therefore, a numerical analysis was conducted to determine the thickness of the steel ring.

In the numerical analysis, steel rings with three different thicknesses were considered: 30, 40, and 50 mm thicknesses (T30, T40, and T50), as shown in Figure 4.10. The eight-node solid elements of 2 mm with selective reduced integration (ELFORM=2) were used for modeling. Since the steel ring is in the linear elastic state during the confined tests, the linear elastic model was used for the material model, and the model parameters were determined from the material properties of F53 steel in Table 4.4. The radial internal pressure was applied to the inner surface of the steel ring, as shown in Figure 4.11 (a). The applied internal pressure time history is presented in Figure 4.11 (b) that was obtained from a preliminary confined SHPB test.

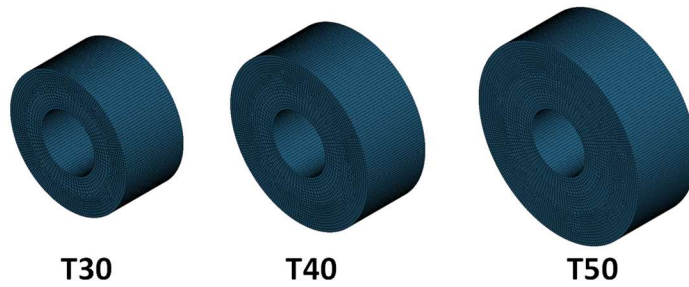
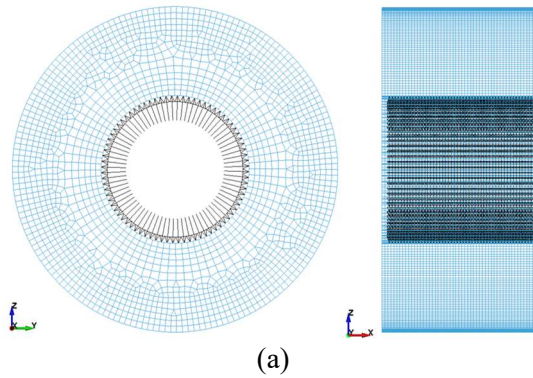


Figure 4.10 Steel ring models



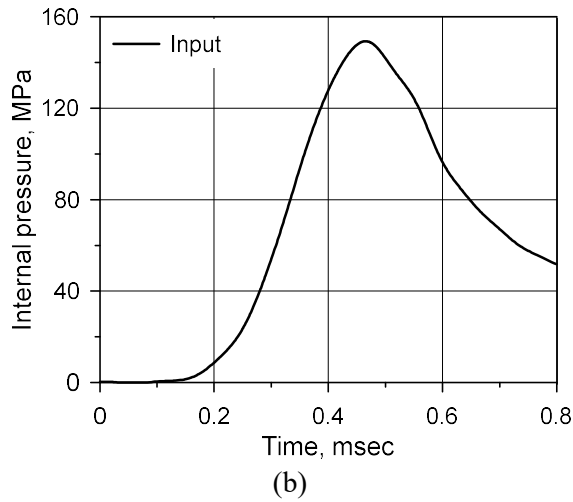


Figure 4.11 Loading conditions; (a) Loaded segments;
(b) Internal pressure history

As an analysis result, circumferential strain at the center on the external surface of the steel ring was obtained, and the internal pressure was estimated using Equation (4.7). Figure 4.12 shows the estimation results. The ratios of the maximum estimated pressure to the maximum input pressure were 97.9%, 96.3%, and 96.1% for T30, T40, and T50 cases, respectively. For the case of T30, the estimated internal pressure showed good agreement with the input internal pressure with an error of about 2% at the maximum pressure. On the other hand, the cases of T40 and T50 underestimated the input internal pressure because of the larger inertial force in the steel ring, compared with the T30 case. Therefore, the thickness of the steel ring was determined as 30 mm.

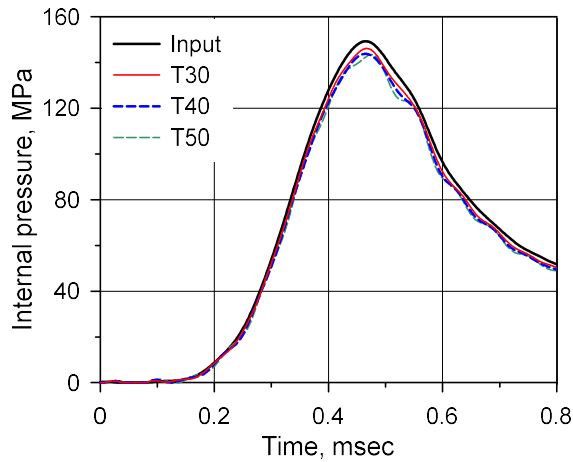


Figure 4.12 Internal pressure estimated from the circumferential strain data

In the case of the steel disks, the diameter was determined as 49.8 mm to prevent the disks from being stuck in the steel ring due to the Poisson effect. The length was designed as 10 mm to prohibit the loading plate or bar components from being in contact with the steel ring during the tests. Figure 4.13 shows the cross-sectional drawing of the specimen cell that consisted of the specimen, steel ring and disks, and Figure 4.14 presents the manufactured steel ring and a specimen.

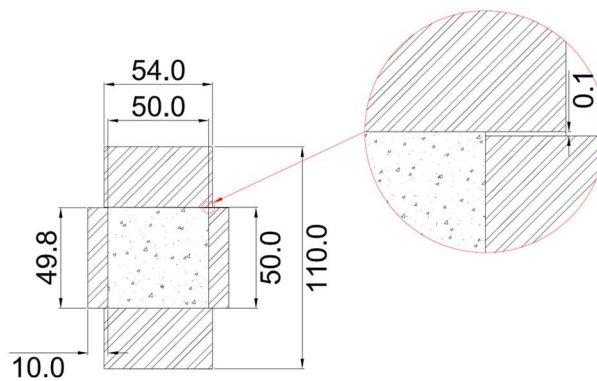


Figure 4.13 Cross-sectional drawing of the specimen cell

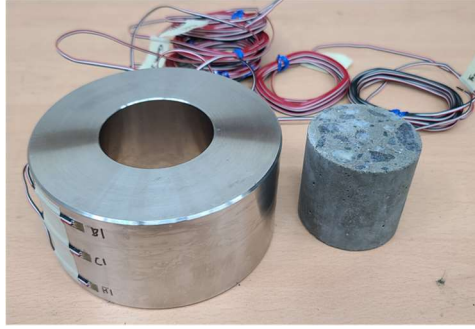


Figure 4.14 Manufactured steel ring and specimen

4.3.2.2. Test procedure

Figure 4.15 shows the static confined compressive test setup. All interfaces among the specimen, steel ring, steel disks, and loading plates were lubricated using PTFE grease to minimize the frictional effect, as shown in Figure 4.15 (a). Then, the specimen cell was loaded with a loading rate of 5×10^{-7} m/s through displacement control. This loading rate corresponded to the axial strain rate of about 10^{-5} s⁻¹. The test was terminated when the axial force reached 780 kN that corresponded to the proportional limit of the steel disks.

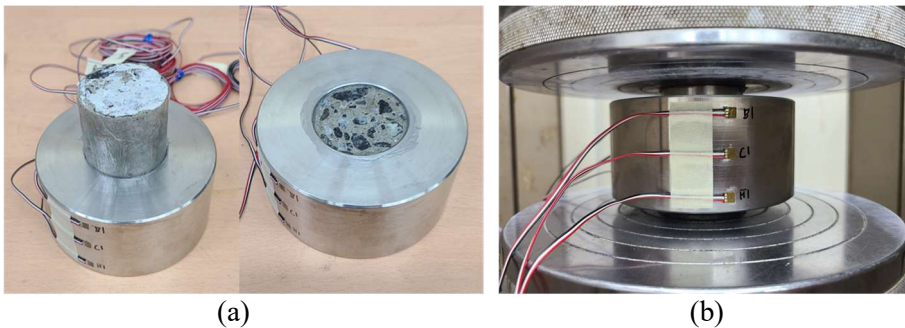
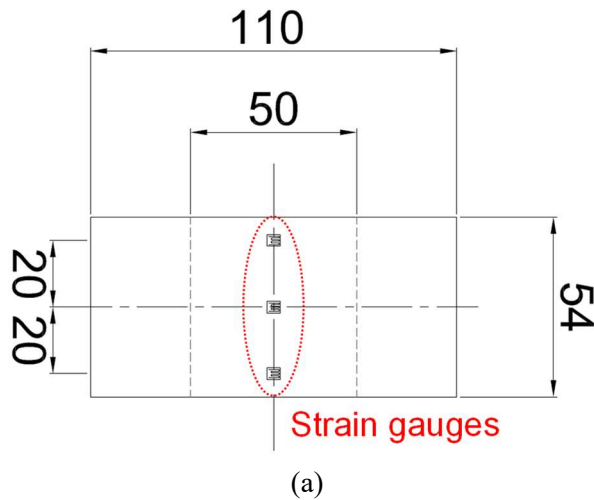


Figure 4.15 Static confined compressive test setup; (a) Lubrication using PTFE grease; (b) Mounted specimen cell

4.3.2.3. Measurement, data-processing procedure and test results

The axial force was measured using a load cell within the universal testing machine to obtain the axial stress of the specimen. As shown in Figure 4.16, six strain gauges were attached at 180° positions in three locations, and the signals of two strain gauges at the center were used for the calculation of the radial stress of the specimen. The test data was sampled with a sampling rate of 1 Hz, and the data was filtered using the moving average. The window size of the moving average was determined as 11 so that the original test data was not distorted.



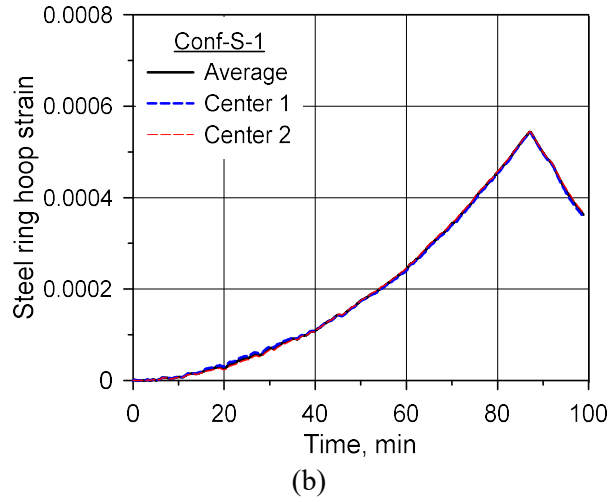


Figure 4.16 Measurement of strain of the steel ring; (a) Strain gauge positions;
(b) Typical external circumferential strain of the steel ring (Conf-S-1)

The radial stress of the specimen was calculated using Equation (4.7), and the circumferential stress was assumed to be equal to the radial stress. Then, the pressure (p) and principal stress difference ($\Delta\sigma$) were calculated using Equations (4.8) and (4.9), respectively; here, s_{ij} is deviatoric stress tensor of the specimen. Figure 4.17 shows the loading paths of four specimens and their average path.

$$p = (\sigma_x + 2\sigma_r) / 3 \quad (4.8)$$

$$\Delta\sigma = \sqrt{3s_{ij}s_{ij} / 2} = |\sigma_x - \sigma_r| \quad (4.9)$$

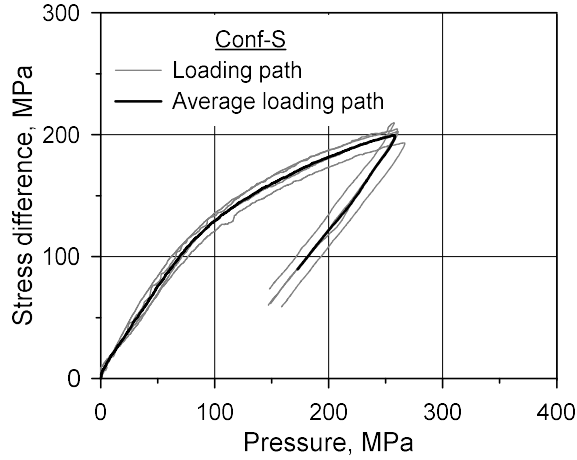


Figure 4.17 Loading path of specimens in the static confined compressive test

The static failure surface was determined using the average loading path. In this study, the maximum failure surface of the KCC model was selected as the static failure surface ($\Delta\sigma_s$), as shown in Equation (4.10) (Malvar et al., 1997; Wu and Crawford, 2015; Kong et al., 2017).

$$\Delta\sigma_s = \begin{cases} a_0 + p / (a_1 + a_2 p) & \text{for } p \geq f_c / 3 \\ (1.5 / \psi)(p + f_t) & \text{for } (0 \leq p \leq f_c / 3) \\ & \text{or } (\lambda \leq \lambda_m \text{ and } -f_t \leq p \leq 0) \\ 3(p / \eta + f_t) & \text{for } p \leq 0 \text{ and } \lambda > \lambda_m \end{cases} \quad (4.10)$$

where f_c and f_t are static compressive and tensile strengths, respectively; a_0 , a_1 , and a_2 are maximum shear failure surface parameters; ψ is the tensile-to-compressive meridian ratio; η and λ are yield scale factor and damage function, respectively; and λ_m is damage function value corresponding to $\eta=1$. In the interesting domain ($p \geq f_c / 3$), three failure

surface parameters (a_0 , a_1 , and a_2) should be assessed to determine the static failure surface. For the assessment, three assumptions were used.

- (1) The static failure surface passes through the uniaxial strength point.
- (2) The static failure surface is in contact with the average loading path.
- (3) The a_1 is independent of f_c (Malvar et al., 1997; Wu and Crawford, 2015; Kong et al., 2017).

The first and second assumptions can be mathematically expressed using Equations (4.11) and (4.12); here, considering the third assumption, a_1 was assumed as 0.5698 by referring to Kong et al. (2017).

$$a_0 = f_c - \frac{f_c}{(3a_1 + a_2 f_c)} \quad (4.11)$$

$$\begin{cases} \Delta\sigma_s(p, a_0, a_1, a_2) = \Delta\sigma(p, a_0, a_1, a_2) & \text{for } p = p_f \\ \Delta\sigma_s(p, a_0, a_1, a_2) > \Delta\sigma(p, a_0, a_1, a_2) & \text{for } p \neq p_f \end{cases} \quad (4.12)$$

The a_0 and a_2 that satisfy above equations were numerically found, and the results are $a_0 = 24.2238$ MPa, $a_1 = 0.5698$, and $a_2 = 0.003470$ MPa⁻¹. Figure 4.18 shows the determined static failure surface and average loading path.

As shown in Figure 4.18, the specimen showed similar behavior to that of the strain-rate-independent case in Chapter 3. The stress initially increased along the uniaxial strain path, which means that the gap between a specimen

and a steel ring was not significant. Then, the triaxiality gradually increased, and the loading path was finally in contact with the static failure surface at a point. After reaching the failure point, the stress continued to increase below the static failure surface until unloading.

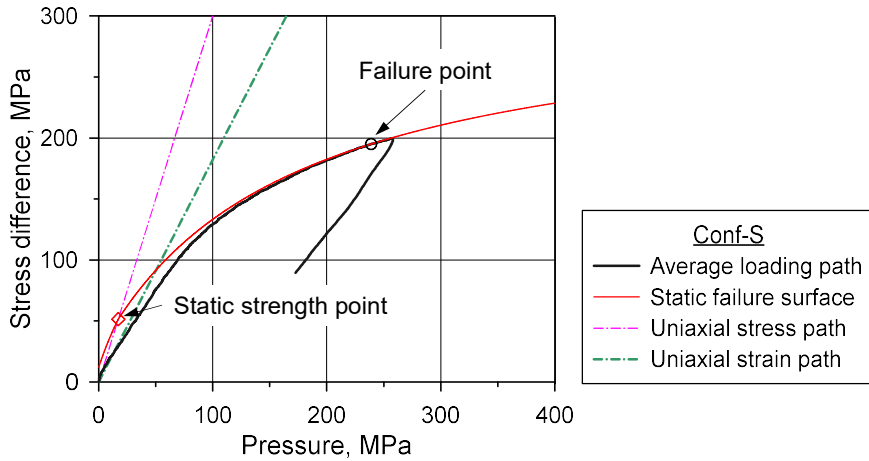


Figure 4.18 Static maximum failure surface

4.3.3. Confined SHPB test

4.3.3.1. Test procedure

The confined SHPB test was conducted using the same apparatus as that of the conventional SHPB test. Moreover, the same striker bar and pulse shapers were used to generate desirable incident waves with long loading durations and slow loading rates. Impact velocities were increased to 10, 12, 14, 16, and 17 m/s since confined specimens have stronger impact resistance compared to unconfined specimens of the conventional SHPB tests.

The identical steel ring and disks with those of the static confined compressive test were used for the confined SHPB test. Figure 4.19 shows the confined SHPB test setup. All interfaces among the specimen, steel ring, steel disks, and bar components were sufficiently lubricated using PTFE grease to minimize the frictional effect, as shown in Figure 4.19 (b). Then, the specimen cell was mounted on a PTFE block and it was neatly sandwiched, as shown in Figure 4.19 (c). Finally, the specimen cell was loaded by the striker bar and air gun.

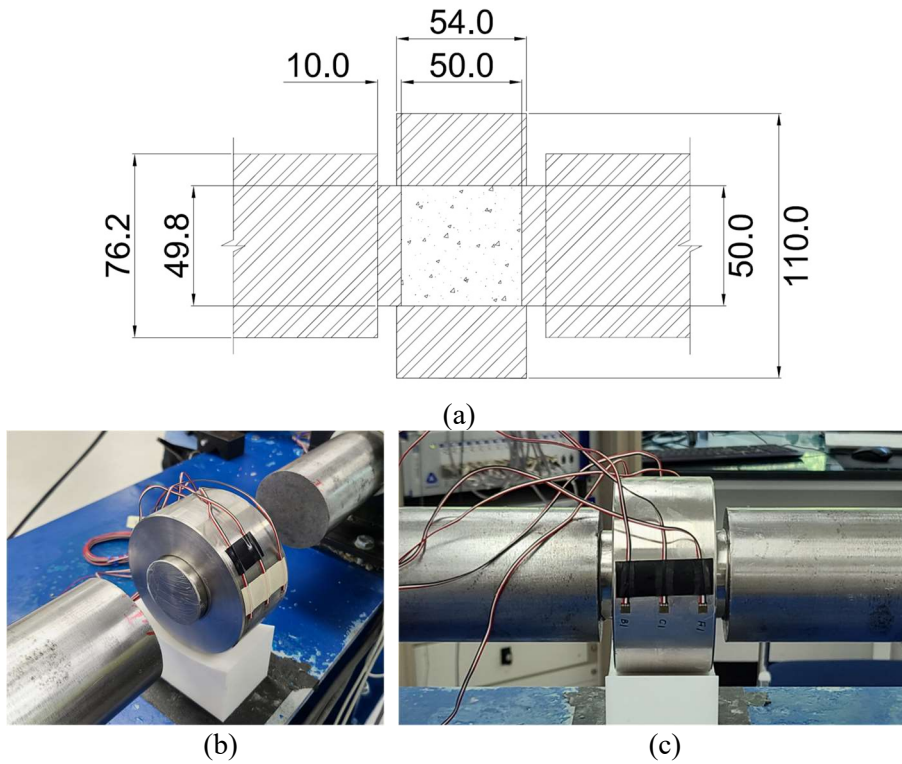
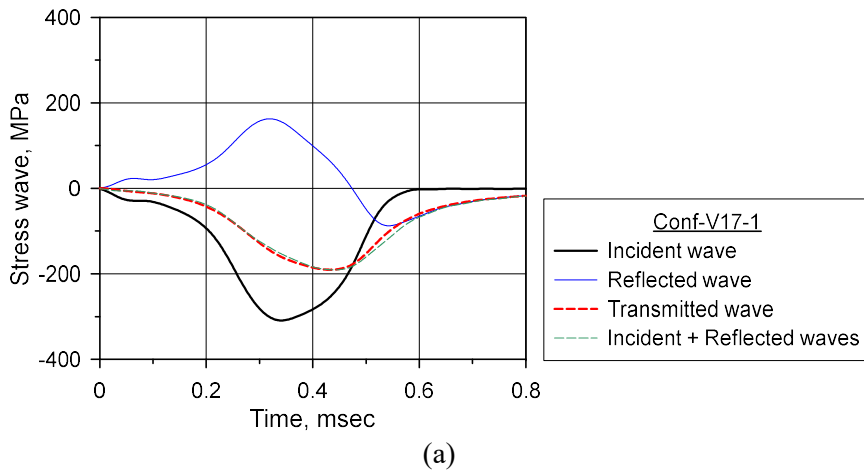


Figure 4.19 Confined SHPB test setup; (a) Drawing; (b) Lubricated specimen cell; (c) Mounted specimen cell

4.3.3.2. Measurement and data-processing procedure

The test data ($\varepsilon_{incident}$, $\varepsilon_{reflect}$, $\varepsilon_{transmitted}$, and $\varepsilon_{\theta,ring}$) was measured through the same procedures as those in the conventional SHPB test and static confined compressive test. The data was sampled with a sampling rate of 1 MHz, and it was filtered using a low-pass filter with a cutoff frequency of 15 kHz. Figure 4.20 shows the typical test data of the confined SHPB test. As shown in the figure, any issue about the time lag between stress waves and steel ring strain signals, which may be caused by stress wave travel or gap, was not observed.



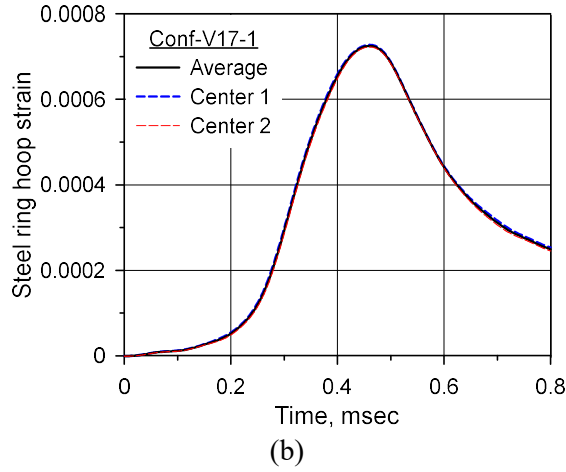


Figure 4.20 Typical test results of the confined SHPB test (Conf-V17-1);
 (a) Stress waves; (b) External circumferential strain of the steel ring

The axial and radial stresses were obtained using Equations (4.1) and (4.7) that are based on one-dimensional stress wave theory and static elastic solution, respectively. To calculate the axial strain rate of the specimen, the total strain rate ($\dot{\epsilon}_{total}^{eng}$) and strain (ϵ_{total}^{eng}) considering the deformation of both steel disks and specimen were calculated first, as shown in Equations (4.13) and (4.14). Then, the strains of the steel disks were excluded from the total strain using Equation (4.15), and the axial strain rate was obtained using Equation (3.3).

$$\dot{\epsilon}_{total}^{eng} = \frac{c_{1,b}}{l_s + 2l_d} (\epsilon_{incident} - \epsilon_{reflect} - \epsilon_{transmitted}) \quad (4.13)$$

$$\epsilon_{total}^{eng} = \int_0^t \frac{c_{1,b}}{l_s + 2l_d} (\epsilon_{incident} - \epsilon_{reflect} - \epsilon_{transmitted}) d\tau \quad (4.14)$$

$$\varepsilon_x^{eng} = \varepsilon_{total}^{eng} + 2 \left(\varepsilon_{total}^{eng} - \frac{A_s \sigma_x}{E_d A_d} \right) \frac{l_d}{l_s} \quad (4.15)$$

where l_d and A_d denote the initial length and cross-sectional area of the steel disk; and E_d is elastic modulus of the steel disks. Even though the radial strain of the specimen was minimized in the confined SHPB test, the radial strain was considered in the analysis to obtain more precise strain rate value. The engineering radial strain (ε_r^{eng}) was calculated using Equation (4.16) (Timoshenko and Goodier, 1987), and the radial strain rate was obtained using Equation (4.4).

$$\varepsilon_r^{eng} = \frac{r_{o,ring}}{2r_{i,ring}} \left[\left(1 + \nu_{ring} \right) \frac{r_{o,ring}}{r_{i,ring}} + \left(1 - \nu_{ring} \right) \frac{r_{i,ring}}{r_{o,ring}} \right] \varepsilon_{\theta,ring} \quad (4.16)$$

where ν_{ring} is the Poisson's ratio of the steel ring. The pressure and principal stress difference were calculated using Equations (4.8) and (4.9), and the effective deviatoric strain rate was obtained using Equation (4.5). The typical axial stress-strain curve and loading path of the specimen were presented in Figure 4.21.

Lastly, the dynamic failure surface and the pure rate DIF were evaluated using the methodology proposed in Chapter 3 according to Figure 3.5. As shown in Figure 4.21 (b), the loading path showed the same tendency as that of the strain-rate-dependent cases in Chapter 3. The stress initially increased along the uniaxial strain path, which implies that the gap between a specimen and a steel ring was negligible. Then, the loading path crossed over the static

failure surface, and the slope of the loading path decreased with an increase in the triaxiality. Finally, the loading path was in contact with the dynamic failure surface. After the failure, the stress continuously increased below the dynamic failure surface until unloading, resulting in a continuous increase in the axial stress.

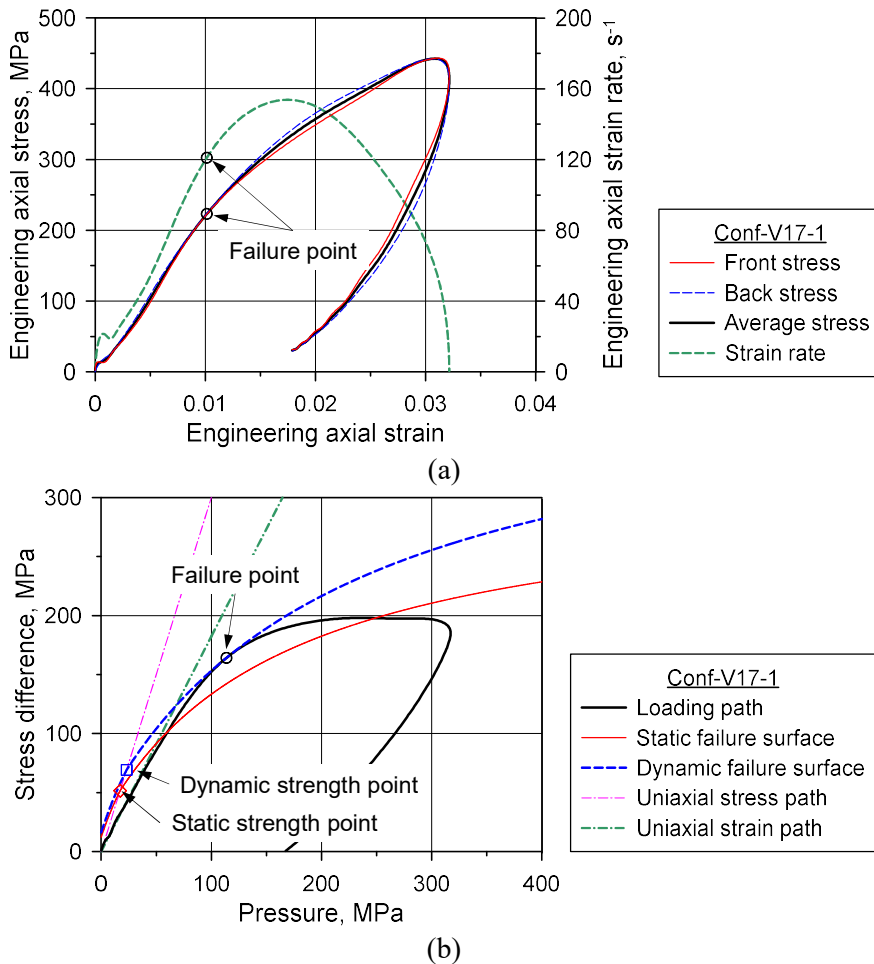


Figure 4.21 Typical test results of the confined SHPB test (Conf-V17-1);

(a) Axial stress–strain relationship and axial strain rate history;

(b) Loading path and dynamic failure surface

4.4. Test results and discussion

4.4.1. Assessment of dynamic stress equilibrium

In the SHPB tests, since the axial stress of the specimen was determined from the average axial stress, the front and back stresses of the specimen should be close to each other for the data to be reliable. Therefore, the dynamic stress equilibrium of specimens was assessed prior to analyzing the test results. The dynamic equilibrium can be evaluated using an R-value (Flores-Johnson and Li, 2017; Kim et al., 2019), as shown in Equation (4.17). The R-value indicates the ratio of the difference in the front and back stresses to the average strength. Figure 4.22 indicates the R-values in the conventional and confined SHPB tests. All specimens in the confined SHPB test showed R-values lower than 5%, and most specimens in the conventional SHPB test showed R-values lower than 10%, indicating that the specimens were almost in the dynamic equilibrium state. Only a few cases of the conventional SHPB tests with the impact velocity of 14 m/s showed the R-values ranged in 11–13%, which means that these specimens were in the moderate non-equilibrium states. Therefore, this study considered all specimens to be in the dynamic equilibrium state, and all test data was used for the analysis and discussion.

$$R = \frac{|\sigma_{x,front} - \sigma_{x,back}|}{\sigma_x} \Bigg|_{\text{at peak average stress}} \quad (4.17)$$

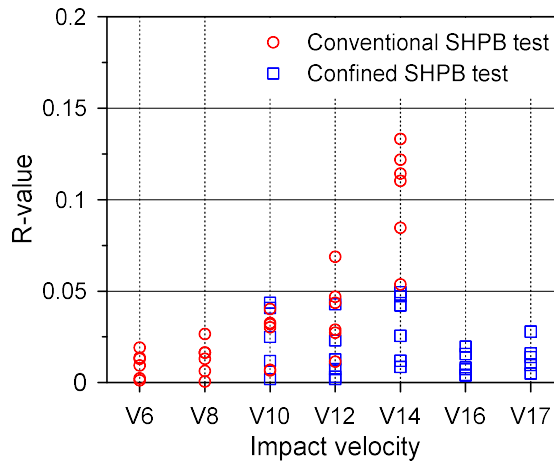


Figure 4.22 Assessment of dynamic stress equilibrium of specimens

4.4.2. Comparison between conventional and confined SHPB tests

The DIF–effective deviatoric strain rate data was plotted in Figure 4.23. Both DIFs showed an increasing tendency with an increase in the effective deviatoric strain rates. As expected, the apparent DIF obtained from the conventional SHPB test showed higher values than the pure rate DIF from the confined SHPB test. This result means that using the apparent DIF leads to an overestimation of the resistance of concrete structures subjected to extreme loadings.

Moreover, an overestimation of dynamic strength in the conventional SHPB test comes from the lateral inertial effect of the specimen, and the inertial effect is proportional to the square of specimen diameter (Forrestal et al., 2007; Zhang et al., 2009; Lee et al., 2018). Therefore, the difference between the pure rate and apparent DIFs is expected to increase when the specimen size becomes larger to contain 19 mm or 25 mm aggregates.

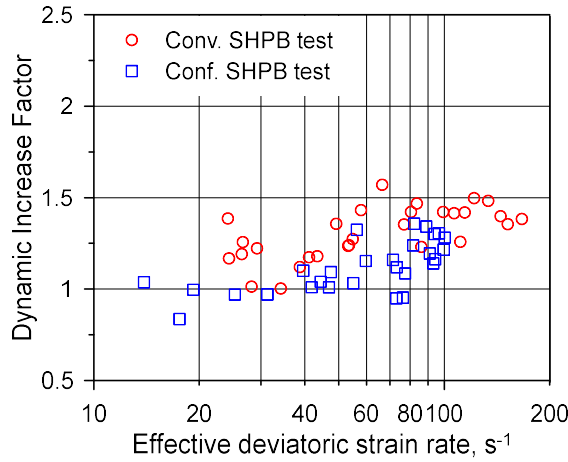


Figure 4.23 DIF–effective deviatoric strain rate relationships

4.4.3. Suggestion of pure rate DIF model

Strain rates in structures under extreme loadings are distributed in a very wide range. Strain rates of several hundred s^{-1} can occur in a local region, such as an impact region or region near a blast, while strain rates of a few s^{-1} can be observed in a region far from the local region. Therefore, a DIF model considered in an FEA for a structure subjected to extreme loadings should cover a wide range of strain rates. A hyperbolic tangent function has an upper limit, so an overestimation of DIF due to extrapolation can be prevented. Accordingly, the function was chosen as DIF models in previous studies (Gebbeken and Ruppert, 2000; Gebbeken and Greulich, 2003; Xu and Wen, 2013). This study also selected the hyperbolic tangent function of the common logarithm of effective deviatoric strain rate as a regression model for same reasons. Equation (4.18) shows the regression model of the DIF.

$$\gamma = \left\{ \left[\tanh \left(\left(\log_{10} \frac{\dot{\epsilon}_{eff}}{\dot{\epsilon}_0} - W_x \right) S \right) \right] \left[\frac{F_m}{W_y} - 1 \right] + 1 \right\} W_y \quad (4.18)$$

where $\dot{\epsilon}_0 = 1 \text{ s}^{-1}$ is the reference deviatoric strain rate; F_m is the upper limit of the DIF model; W_y is a coefficient related to the lower limit; W_x is a coefficient related to the location of the inflection point; and S is a coefficient related to the slope. The pure rate and apparent DIF models were obtained based on the pure rate and apparent DIF data, respectively. F_m was determined as 1.7, referring to the upper limits of the compressive DIFs of Xu and Wen (2013) and the CSC model (Murray, 2007). Then, W_y was calculated using the lower limit condition, $W_y = (F_m + 1) / 2 = 1.35$. To determine W_x and S , the regression analysis was conducted based on each data set employing Levenberg-Marquardt nonlinear least squares algorithm. From the regression analysis results, W_x was determined as 2.088 and 1.924 for γ_{rate} and γ_{app} , respectively, and S was 3.021 and 1.020 for γ_{rate} and γ_{app} , respectively. The suggested DIF models were presented in Figure 4.24. The pure rate DIF model is valid in the shaded effective deviatoric strain rate range (10–100 s^{-1}).

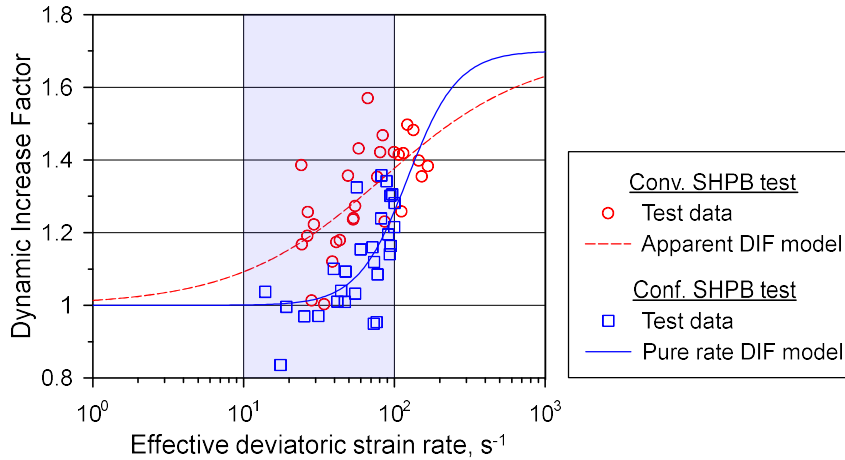


Figure 4.24 Proposed DIF models

Figure 4.25 shows the comparison of the suggested pure rate DIF model with the previous pure rate DIF models; here, the strain rate for previous DIF models was not the effective deviatoric strain rate but the axial strain rate. Compressive and tensile strengths of 51.5 and 3.71 MPa, respectively, were used to calculate the compressive DIF of Xu and Wen (2013). The previous pure rate DIF models showed a significant difference from the suggested pure rate DIF. The DIF model of Xu and Wen (2013) showed a lower slope compared with the suggested pure rate DIF model, which means that the assumption of the identical strength enhancement in tension and compression is not satisfied in the actual condition. Lee et al. (2018) selected the power function as a regression model for pure rate DIF, but the power function did not coincide with the distribution of the actual pure rate DIF data. In conclusion, the discrepancy between the suggested and previous pure rate DIF models was caused by the assumptions without verification in previous studies.

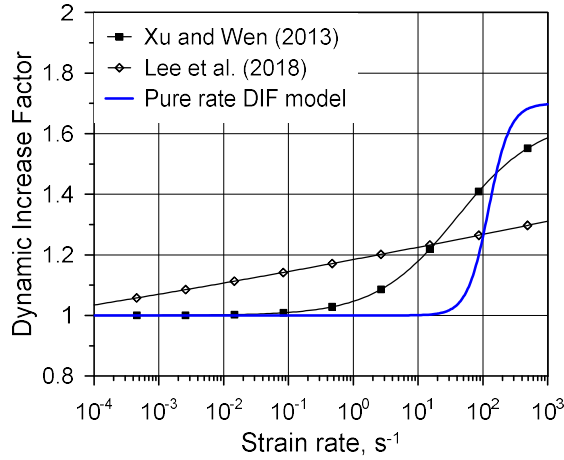


Figure 4.25 Comparison of the suggested pure rate DIF model with the existing pure rate DIF models

It has been hardly understood so far how stress states affect the strain-rate-dependency of concrete, and DIF has been considered to be independent of stress states, such as pressure. However, even if the stress states influence the DIF, the pure rate DIF model obtained from the confined tests is more justified than the existing DIF models. Extreme loadings cause very high pressure of 10^2 – 10^3 MPa in local regions of structures. Therefore, it can be said that the results of the confined SHPB tests in which a pressure of several hundred MPa is generated are closer to the actual conditions than those of the conventional SHPB tests in which a pressure of several tens MPa is generated. In view of that, it is expected that the suggested pure rate DIF model can be applied to the design and analysis of concrete structures under extreme loadings.

4.5. Concluding remarks

In this chapter, experimental work was conducted to propose the pure rate DIF model. The procedures and results of three kinds of tests were described: the conventional SHPB test, static confined compressive test, and confined SHPB test. The static confined compressive test was conducted to determine the static failure surface, and the confined SHPB test was subsequently performed to obtain the pure rate DIF data. The pure rate DIF data was assessed using the static failure surface from the static confined test and the methodology suggested in Chapter 3. Moreover, the conventional SHPB test was also conducted to compare the apparent DIF to the pure rate DIF. The comparison results indicated that the dynamic strength was overestimated in the conventional SHPB test, and using the apparent DIF might result in the overestimation of the resistance of concrete structures against extreme loadings. Lastly, the pure rate DIF model was suggested through the regression analysis based on the confined SHPB test data. A hyperbolic tangent function was used for the regression model because it has the upper limit and the overestimation due to the extrapolation can be prevented. Similarly, the apparent DIF model was also obtained based on the conventional SHPB test data. The suggested pure rate DIF model showed a significant difference from the previous pure rate DIF models, and this difference was due to the not verified assumptions of previous studies.

In the following chapter, a series of numerical analyses for the conventional SHPB test of this study was conducted to verify the suggested pure rate DIF model. The apparent DIF was also considered in the numerical

analysis for purpose of comparison. Moreover, a numerical example was introduced to demonstrate the validity of the pure rate DIF model. FEA on the drop-weight impact test for RC beams of Ahn (2021) was conducted applying the pure rate DIF, and the results were compared with the test data.

5. Verification and Application of Suggested DIF

5.1. Numerical analysis on SHPB test

In order to verify the pure rate DIF suggested in Chapter 4, the numerical analysis on the conventional SHPB test was conducted in this section. The FEA model was established using LS-DYNA, and both apparent and pure rate DIF models were considered in the FEA. The apparent DIF–effective deviatoric strain rate relationship was obtained as the FEA result.

5.1.1. Establishment of numerical model

5.1.1.1. Modeling part and boundary conditions

A cylinder specimen of D50×L50 mm was modeled using 1 mm eight-node solid elements with the selective reduced integration (ELFORM=2). The mesh size was selected through a mesh test so that the variation of FEA results depending on the mesh size was not significant with the selected mesh size. To reenact actual loading conditions in the tests, the deformation velocities of the specimens were applied to the FEA model, instead of modeling the bar components and loading device. As shown in Figure 5.1, the nodes on the back surface of the specimen were constrained in the x-axis direction, and the deformation velocities were input as the prescribed nodal velocity on the front surface. Figure 5.2 shows the average deformation velocities measured in the conventional SHPB tests. During the conventional SHPB test, the specimen was lubricated according to Kim et al. (2022); therefore, any lateral constraint such as friction was not considered in the FEA.

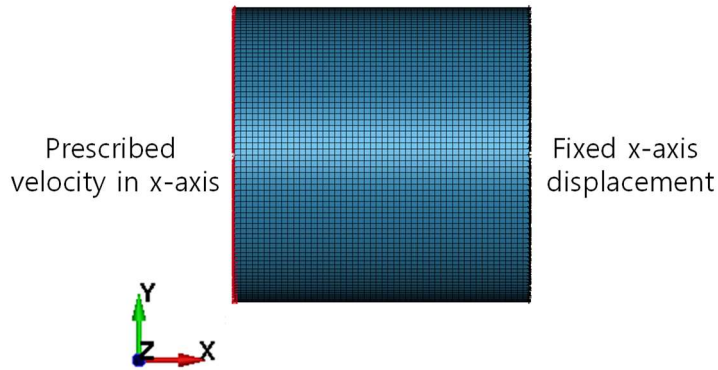


Figure 5.1 Specimen model and boundary conditions

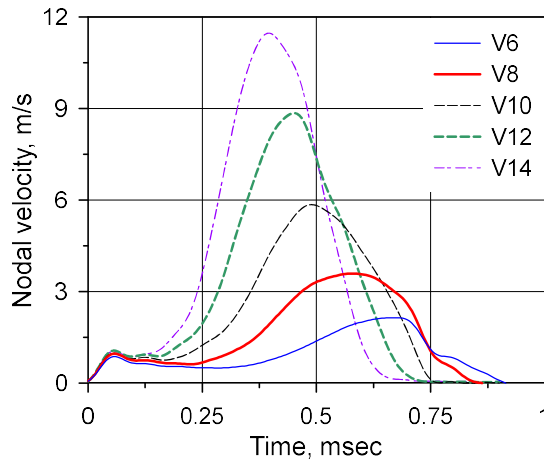


Figure 5.2 Deformation velocities of specimens in the conventional SHPB test

5.1.1.2. Concrete specimen

The KCC model (MAT 72R3) was selected as the concrete constitutive model for two reasons; (1) the KCC model was used to assess the pure rate DIF in Chapter 4, and (2) the DIF model can be input as a user-defined curve in the KCC model. The FEA was terminated before the mesh-entanglement became severe, so any erosion criterion was not considered in the FEA.

As shown in Figure 5.3, three DIF models of compressive strength were considered in the FEA: the pure rate DIF, apparent DIF, and no DIF (strain-rate-independent case). The pure rate and apparent DIF models can be found in Equation (4.18). Moreover, the tensile DIF of Xu and Wen (2013) was used for the DIF model of tensile strength, as shown in Figure 5.4. This DIF model was a function of the axial strain rate, as shown in Equation (2.23). However, this study neglected the discrepancy between axial strain rate and effective deviatoric strain rate because the effect of the tensile DIF was not significant in this analysis and any proper conversion methodology was not suggested.

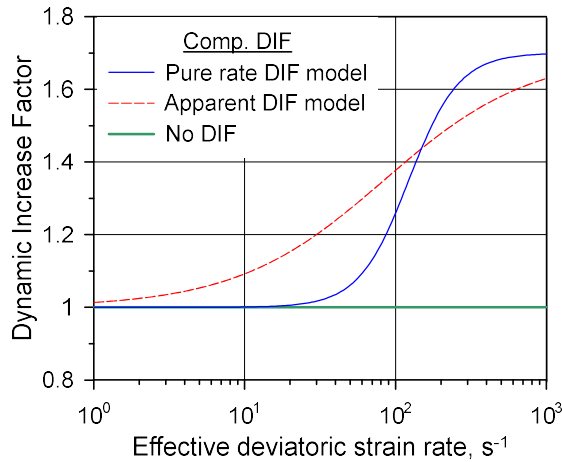


Figure 5.3 DIF models of compressive strength

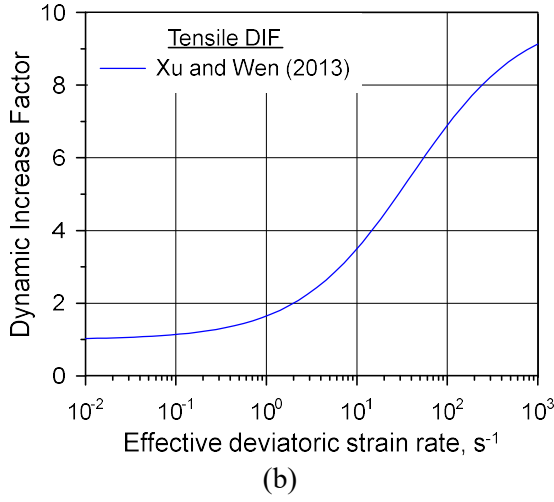


Figure 5.4 DIF model of tensile strength

Material model parameters are listed in Table 5.1. The density (ρ_s) and Poisson's ratio (ν_s) were determined from the static properties in Table 4.2. The tensile strength (f_t) was calculated using the uniaxial tensile strength formula in the fib MC2010 (fib bulletin 65, 2012), as shown in Equation (5.1).

$$f_t = 0.3(f_c - \Delta f)^{2/3} \quad (5.1)$$

where $\Delta f = 8 \text{ MPa}$.

The static failure surface obtained from the static confined test in Section 4.3.2 was used for the maximum failure surface. Yield failure surface parameters (a_{0y} , a_{1y} , and a_{2y}) were determined assuming $\Delta\sigma_y = 0.45\Delta\sigma_s$ in a similar way to Malvar et al. (1997), Wu and Crawford (2015), and Kong et al. (2017); here, $\Delta\sigma_y$ denotes the yield failure surface. Residual failure

surface parameters (a_{1f} and a_{2f}) were determined as the same as those of the maximum failure surface, considering that the residual failure surface should be parallel with the maximum failure surface for high pressure (Kong et al., 2017). Figure 5.5 shows the failure surfaces.

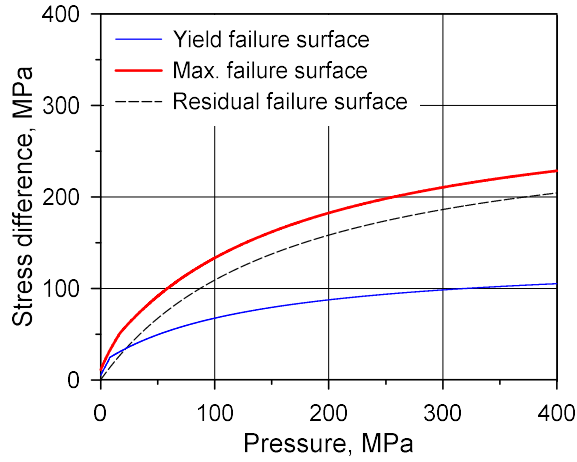


Figure 5.5 Failure surfaces

The localization width (w_{lz}) was determined as 39 mm considering the recommendation of the KCC model (three times G_{max}). The associativity parameter (ω) was 0.9 which was a recommended value for well-confined normal strength concrete (Wu and Crawford, 2015). The damage scaling factors b_1 and b_2 were determined in accordance with Wu and Crawford (2015), and the default b_3 was considered in the FEA.

Table 5.1 Concrete model parameter details (unit: ton, mm, sec)

Description	Symbol	Parameter value
Density	ρ_s	2.434×10^{-9}
Poisson's ratio	ν_s	0.1505
Uniaxial tensile strength	f_t	3.71
Maximum failure surface parameters	a_0	24.2238
	a_1	0.5698
	a_2	0.003470
Yield failure surface parameters	$a_{0,y}$	18.0041
	$a_{1,y}$	1.1646
	$a_{2,y}$	0.008558
Residual failure surface parameters	$a_{1,f}$	0.5698
	$a_{2,f}$	0.003470
Associativity parameter	ω	0.9
Localization width	w_{lz}	39
Damage scaling factors	b_1	0.804
	b_2	1.777
	b_3	1.15

Kong et al. (2017) reported that the default $\eta - \lambda$ relationship caused an overestimation of the stiffness of concrete during the hardening stage and an underestimation of the residual strength during the softening stage. Therefore, the relationship suggested by Markovich et al. (2011) was adopted in the FEA. Figure 5.6 and Table 5.2 show the $\eta - \lambda$ relationship of Markovich et al. (2011). Figure 5.6 indicated the yield scale factor (η) of Markovich et al. (2011) moderately increases and decreases during the hardening and softening stages, respectively, compared with the default values.

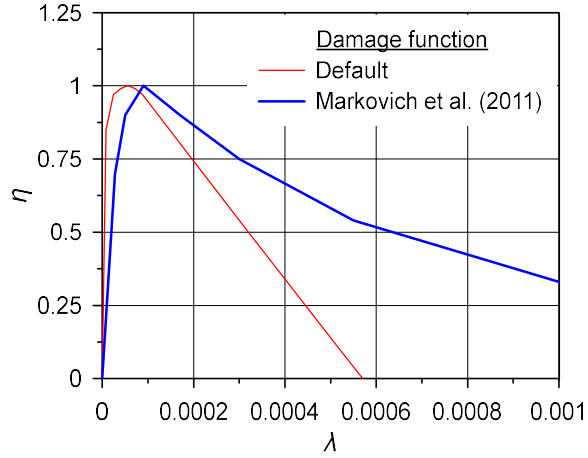


Figure 5.6 $\eta - \lambda$ relationships

Table 5.2 $\eta - \lambda$ relationship proposed by Markovich et al. (2011)

λ	η
0	0
2.8×10^{-5}	0.7
5.0×10^{-5}	0.9
9.0×10^{-5}	1
1.7×10^{-4}	0.9
3.0×10^{-4}	0.75
5.5×10^{-4}	0.54
1.0×10^{-3}	0.33
1.65×10^{-3}	0.17
2.5×10^{-3}	0.09
3.5×10^{-3}	0.032
7.0×10^{-3}	0.005
1.0×10^{10}	0

The tabulated compaction model (EOS 8) was selected as the EOS model. In a similar way to Wu and Crawford (2015), the EOS model parameters were determined by scaling down the default EOS of the KCC model so that the

initial bulk modulus was identical to that obtained from the static compressive tests. The EOS model parameters are listed in Table 5.3. The effect of temperature on EOS was neglected.

Table 5.3 EOS model parameters

ε_v	p , MPa	K_u , MPa
0	0	14290
-0.0015	21	14290
-0.0043	47	14490
-0.0101	75	15215
-0.0305	143	18108
-0.0513	215	21001
-0.0726	305	23894
-0.0943	467	26078
-0.174	2724	58668
-0.208	4167	71448

5.1.2. Data acquisition and processing procedure

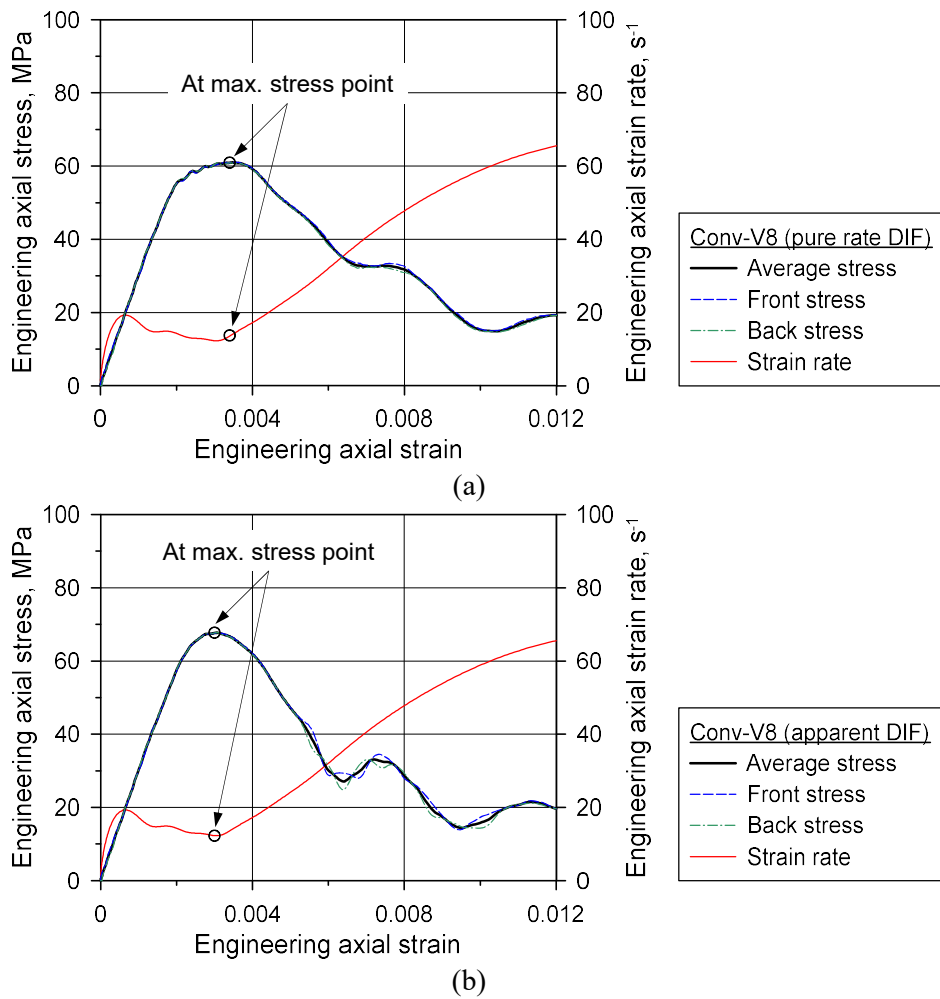
The nodal forces on the front and back surfaces of the specimen were obtained from the FEA, and the axial stress was calculated using Equation (3.1). Moreover, the engineering axial strain was calculated using Equation (5.2); where v_d denotes the deformation velocity of the specimen.

$$\varepsilon_x^{eng} = \frac{1}{l_s} \int_0^t v_d(\tau) d\tau \quad (5.2)$$

The circumferential strain at the center on the circumferential surface of the specimen was obtained in a similar way to the conventional SHPB test. Then, the axial and circumferential strain rates were calculated using Equations (3.3)

and (4.4). Lastly, the effective deviatoric strain rate was calculated using Equation (4.5). The FEA data was sampled with a sampling rate of 1 MHz.

Figure 5.7 shows typical axial stress–strain curves from the FEA. In the same way as the conventional SHPB test, the apparent DIF was acquired using Equation (4.6), and the corresponding effective deviatoric strain rate was also obtained.



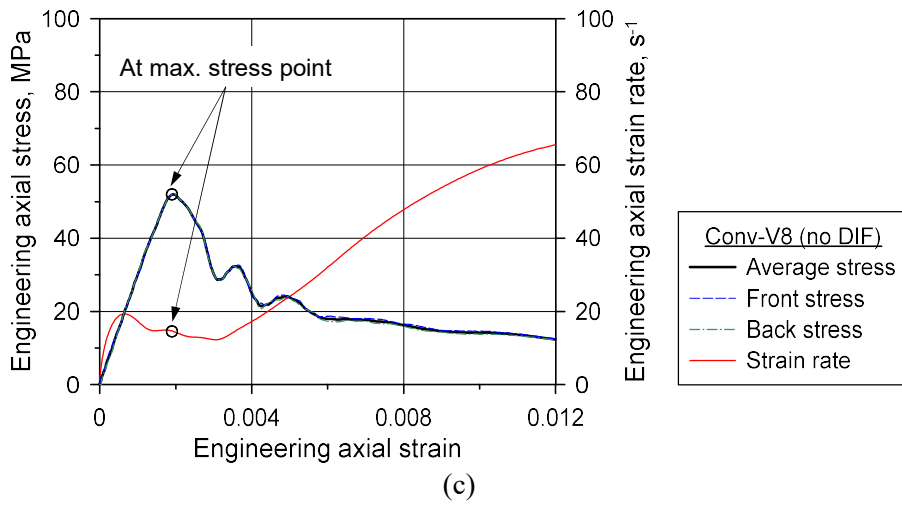


Figure 5.7 Typical axial stress–strain relationships in the FEA;
 (a) Pure rate DIF case; (b) Apparent DIF case; (c) No DIF case

5.1.3. Numerical analysis results

5.1.3.1. *Validity of KCC models and input model parameters*

Prior to discussing the results of FEA on conventional SHPB tests, the validity of the KCC model and its model parameters was examined first. As shown in Figure 5.8, an implicit static analysis on the static compressive strength tests for specimens of D50×L100 mm was conducted, and its results were compared with the static stress–strain curves of tests. The concrete specimen was modeled using the same type and size of elements and the same constitutive model as those of FEA on the conventional SHPB tests. The loading plates were modeled using the linear elastic model and the 1.25 mm eight-node solid elements with the reduced integration (ELFORM=1). The frictional coefficient between the specimen and plates was assumed as 0.2 using the Automatic Surface to Surface option. Lastly, the specimen was loaded by moving the bottom loading plate upwards.

Figure 5.9 exhibits the static stress–strain relationships of FEA and tests. The axial stress was calculated from the resultant contact forces, and the axial strain was obtained from the elements located at the center of the specimen. As shown in the figure, the FEA model somewhat overestimated the stress in the strain-hardening region, but it predicted accurately the overall static behavior of the specimen including the initial stiffness and strength. Therefore, it was concluded that the concrete constitutive model and its parameters were appropriately determined.

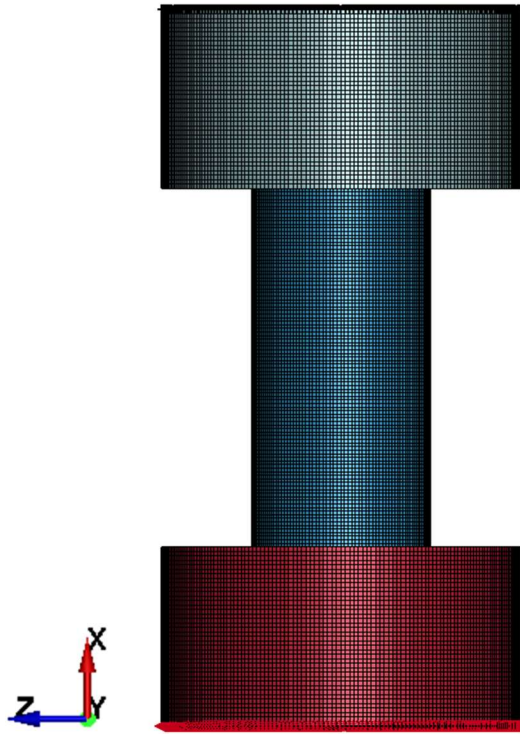


Figure 5.8 Numerical model to validate the KCC model and model parameters

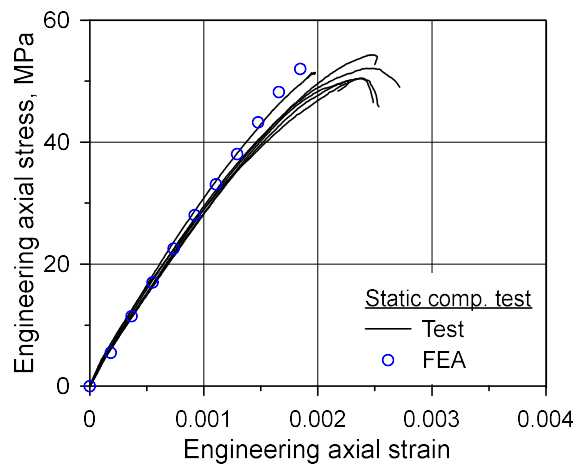
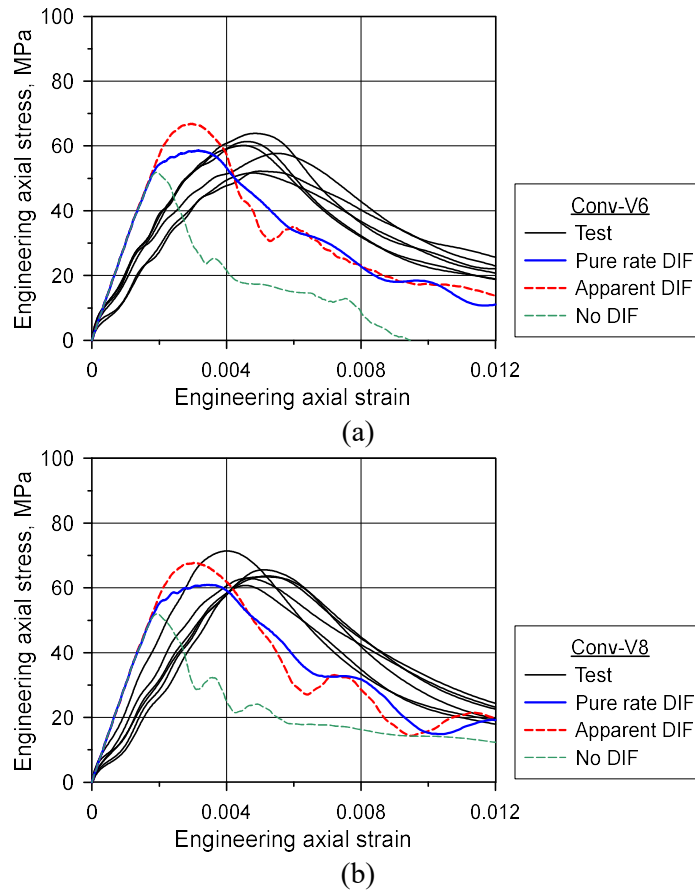
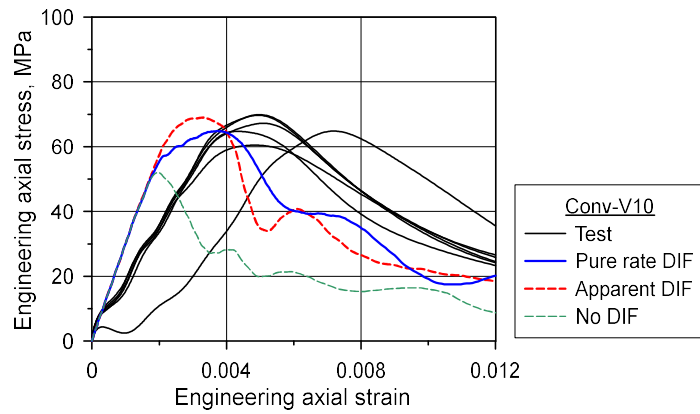


Figure 5.9 Comparison of static stress–strain relationship

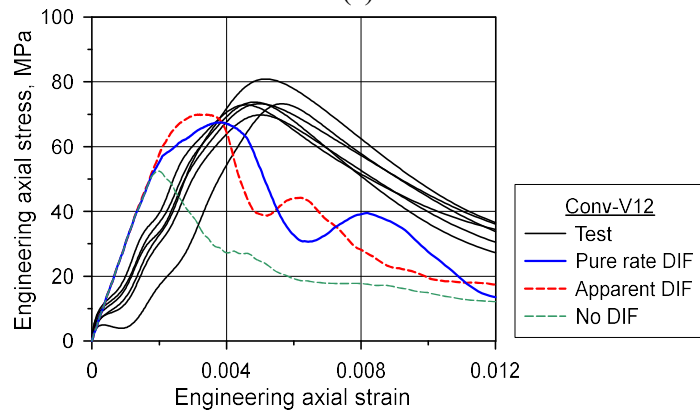
5.1.3.2. Numerical analysis results for conventional SHPB tests

Figure 5.10 shows the comparison of dynamic stress–strain curves of FEA to those of conventional SHPB tests. The stiffness of FEA results was higher than that of test results regardless of the input DIF models, which might be caused by an incomplete contact condition in the tests due to reasons such as the manufactured tolerance of specimens. Moreover, it was observed that apparent dynamic strength varied depending on the input DIF models. Therefore, the predictive accuracy for apparent strength was examined.

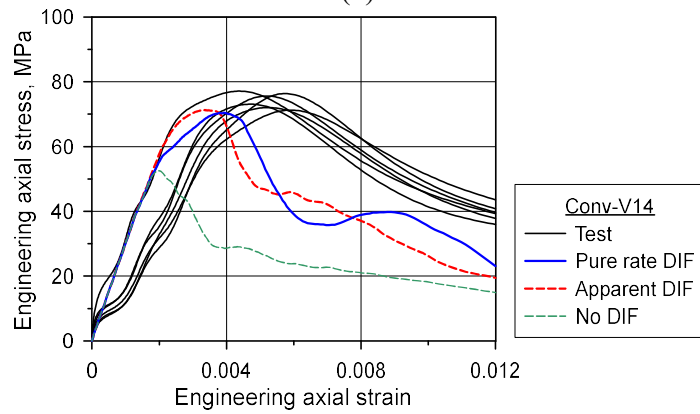




(c)



(d)



(e)

Figure 5.10 Comparison of dynamic stress–strain relationship; (a) Conv-V6; (b) Conv-V8; (c) Conv-V10; (d) Conv-V12; (e) Conv-V14

To assess the predictive accuracy for apparent dynamic strength, the apparent strength ratio (R_{AS}) was introduced, as shown in Equation (5.3). The apparent strength ratio is the ratio of the apparent strength of FEA to the average apparent strength of the conventional SHPB tests.

$$R_{AS} = \frac{(f_{d,app})_{FEA}}{(f_{d,app})_{\text{Average of test results}}} \quad (5.3)$$

Figure 5.11 shows the apparent strength ratio with respect to the impact velocities of the striker bar, and Table 5.4 lists the maximum, minimum, mean values, and coefficient of variation (COV) of the apparent strength ratio. The no DIF cases underestimated the apparent strength ratio with an error of -22% on average, which means that the strain-rate-dependency of concrete should be considered in the impact and blast loading analysis for accurate prediction. In the FEA using the apparent DIF, moderate overestimations of apparent strength were observed. The apparent strength ratio was estimated in the range from 95% to 116%, and its average was 103%. On the other hand, the FEA with the pure rate DIF showed the apparent strength ratio ranged from 91% to 101%, and the apparent strength ratio was predicted with an error of 4% on average.

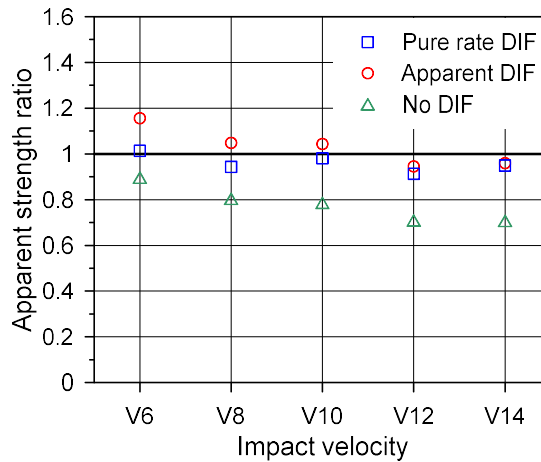


Figure 5.11 Apparent strength ratio

Table 5.4 Distribution characteristics of the apparent strength ratio

	Pure rate DIF	Apparent DIF	No DIF
Maximum	1.01	1.16	0.90
Minimum	0.91	0.95	0.71
Mean	0.96	1.03	0.78
COV	0.036	0.073	0.090

For closer examination, the apparent DIF–effective deviatoric strain rate data of each FEA was plotted in Figure 5.12. The no DIF cases showed limited enhancements in the apparent strength. The results of the FEA using the apparent DIF model were found to be higher than the apparent DIF model due to the lateral inertial effects, which implies the possibility of overestimating the resistance of concrete structures subjected to extreme loadings. On the other hand, the results of the pure rate DIF cases coincided

with the apparent DIF model. This means that the dynamic compressive behavior of concrete can be predicted with good accuracy using the suggested pure rate DIF model. Therefore, it was confirmed that the suggested pure rate DIF model was valid.

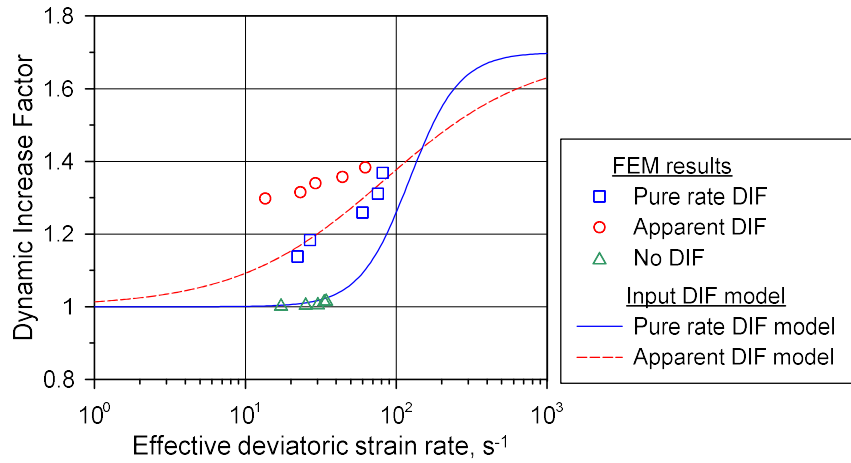


Figure 5.12 Apparent DIF–effective deviatoric strain rate relationships

5.2. Numerical analysis on drop-weight impact test

In this section, a numerical example was described for the application of the pure rate DIF model to FEA. The FEA models of the drop-weight impact tests for RC beams of Ahn (2021) were established using LS-DYNA. Not only the pure rate DIF but also various DIF models adopted in design codes and guidelines were considered in the FEA models. The central deflection time history and damage contour were obtained as FEA results, and those were compared with the test results.

5.2.1. Description of drop-weight impact test for RC beams

Ahn (2021) performed an experimental investigation into the effect of flexural stiffness of RC beams on the maximum deflection under impact loadings. As shown in Figure 5.13, a series of drop-weight impact tests were conducted for full-scale RC beams. This study chose the tests of Ahn (2021) for the FEA example because the strain rate range of the drop-weight impact tests was similar to that of the pure rate DIF data in this study; in the drop-weight impact tests, effective deviatoric strain rates of concrete ranged from 20 to 100 s⁻¹ near an impact region.



Figure 5.13 Drop-weight impact tests for RC beams of Ahn (2021)

In the work of Ahn (2021), the impact energy of a drop-weight and flexural stiffness of RC beams were considered test variables. Table 5.5 shows the designation of test cases and test variables. As shown in the table, two impact energies of 30 and 50 kJ (E30 and E50) and three beams (FS1, FS2, and FS3) were considered, so a total of six tests were conducted.

Table 5.5 Test variables of the drop-weight impact tests (Ahn, 2021)

Designation	Drop-weight			RC beam	
	Mass, ton	Impact velocity, m/s	Impact energy, kJ	Flexural stiffness, kN/mm	Flexural capacity, kN
E30-FS1	2.5	4.90	30	41	519
E30-FS2				63	485
E30-FS3				91	515
E50-FS1		6.32	50	41	519
E50-FS2				63	485
E50-FS3				91	515

Figure 5.14 shows the drawings of the RC beam specimens. These specimens were designed to be statically flexural-critical beams, and they have similar static flexural strengths but different flexural stiffnesses; here, the flexural strength and stiffness were based on three-point bending tests with 3.3, 2.7, and 2.3 m span lengths for FS1, FS2, and FS3 beams, respectively. The concrete material properties are listed in Table 5.6, and the properties of reinforcing bars are presented in Table 5.7.

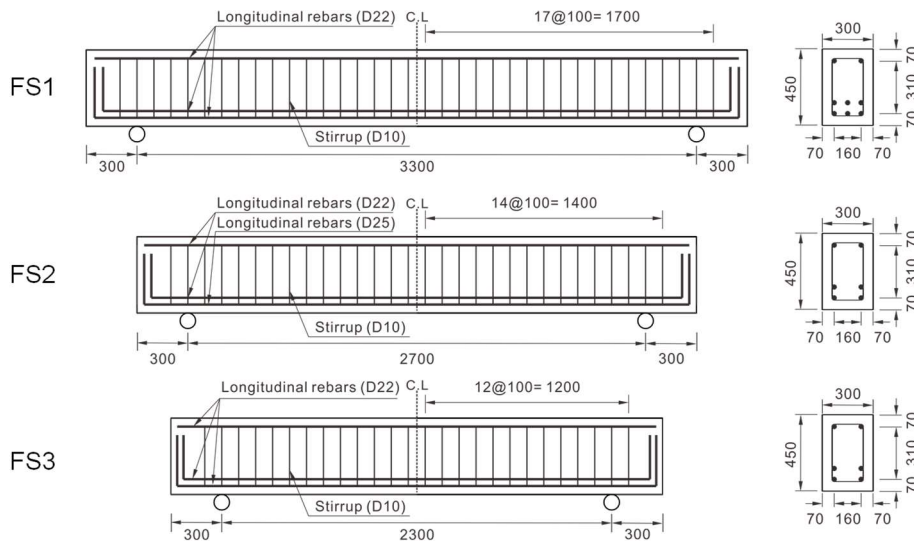


Figure 5.14 Drawings of RC beams (Ahn, 2021)

Table 5.6 Static material properties of concrete

Compressive strength, MPa	Elastic modulus, MPa	Poisson's ratio	Density, kg/m ³
54.8	26732	0.1638	2327

Table 5.7 Static material properties of reinforcing bars

Type	Designation (diameter, mm)	Yield strength, MPa	Ultimate tensile strength, MPa
Longitudinal rebar	D22 (22.2)	569	685
	D25 (25.4)	561	693
Stirrup	D10 (9.53)	464	606

The crack patterns and local damages were observed in the tests, and the impact force, inertial force, reaction force, and central deflection of RC beams were measured, as shown in Figures 5.15 and 5.16. To measure the impact force, three accelerometers were attached along the guide beam of the drop-weight. Each acceleration was multiplied by the corresponding portion of the mass, and the three impact forces were summed for calculating the total impact force. In the same way, the inertial force of the beam was calculated using five accelerometers installed along the beam. Two load cells were installed within the bottom supports to obtain the reaction force, and the central deflection was measured using a laser displacement sensor. Figures 5.17 and 5.18 present the force and central deflection time histories, respectively. The deflection of E30-FS3 was not measured because of abnormal working.

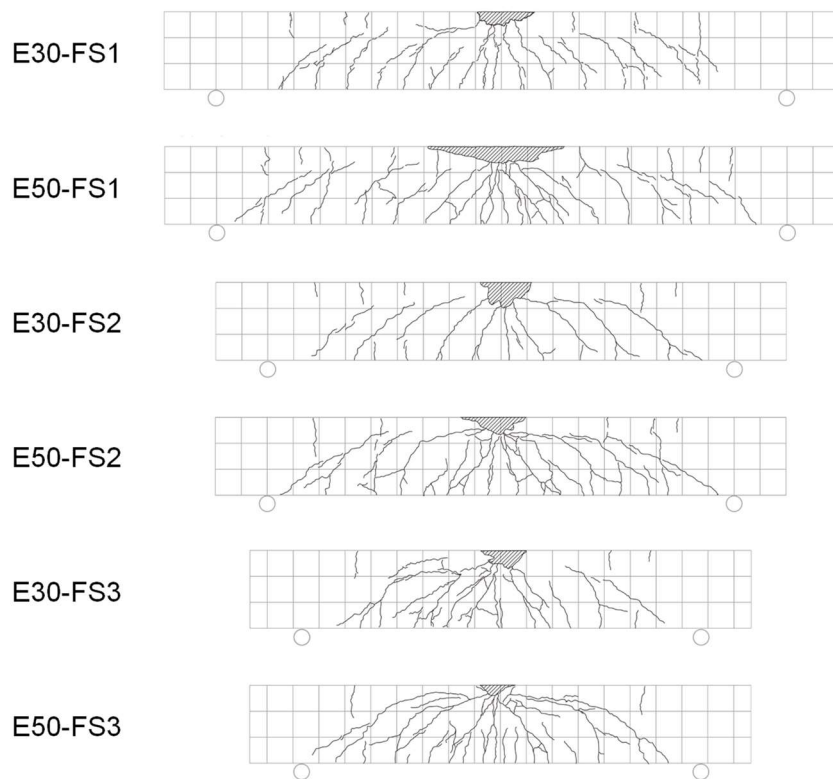


Figure 5.15 Crack patterns of RC beams (Ahn, 2021)

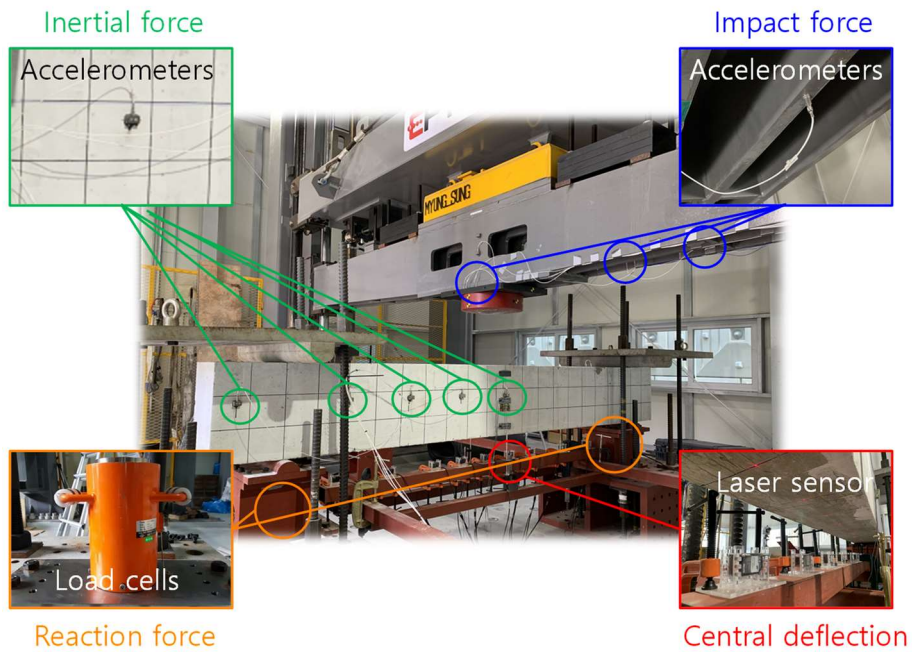
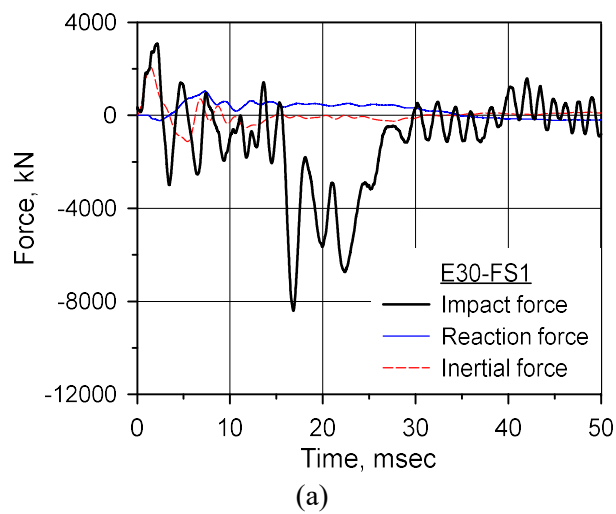
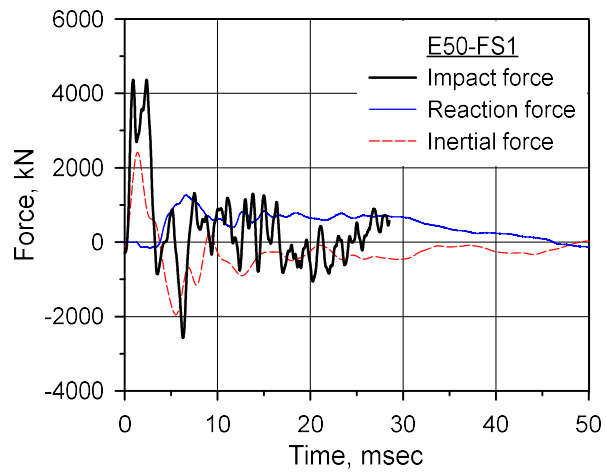
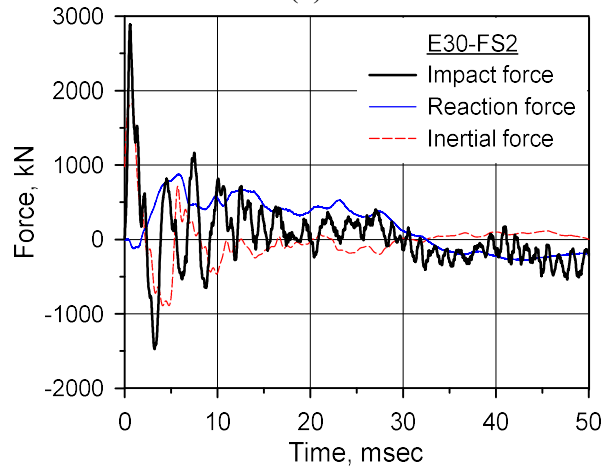


Figure 5.16 Measurement in the drop-weight impact tests (Ahn, 2021)

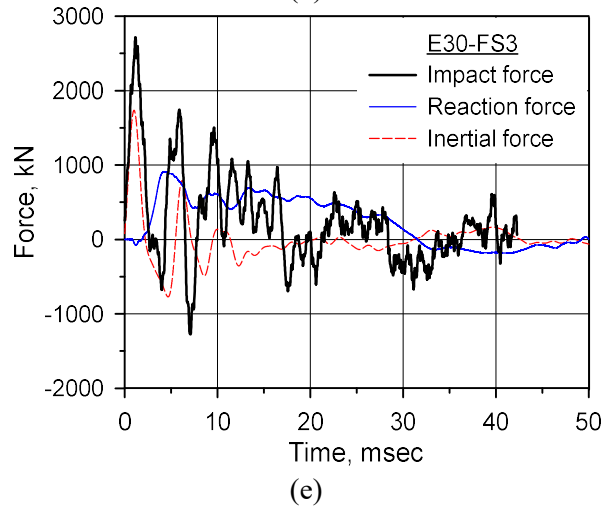
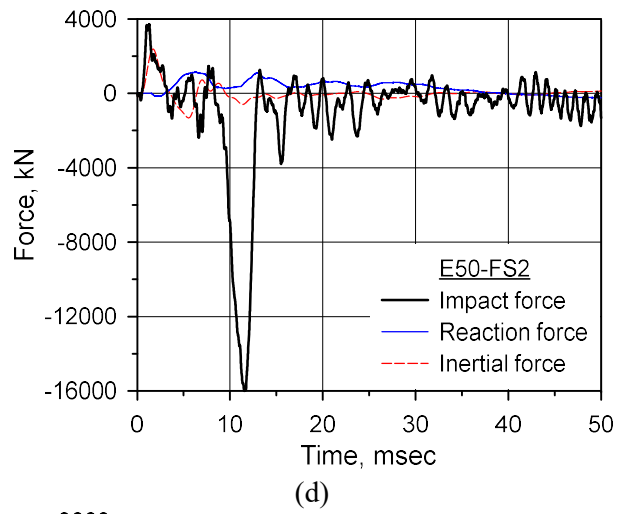




(b)



(c)



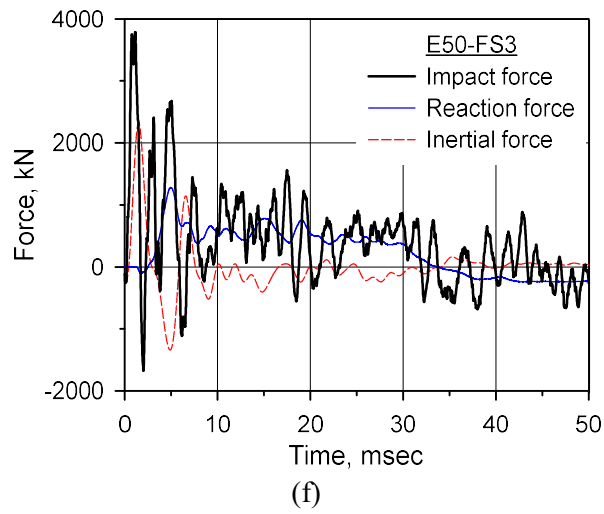
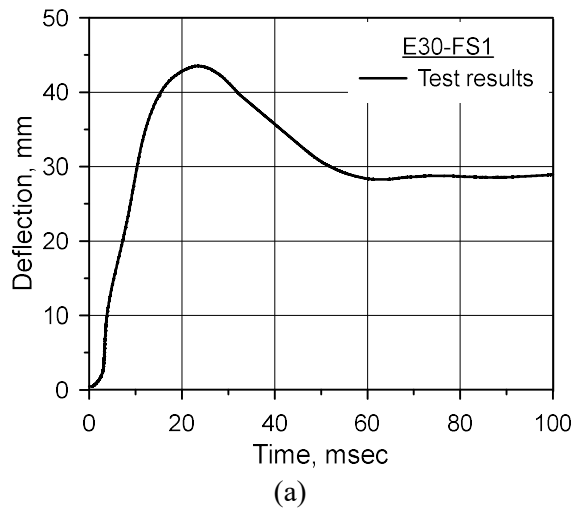
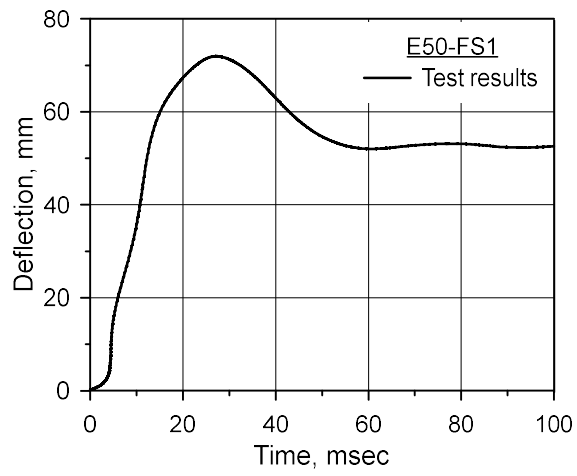
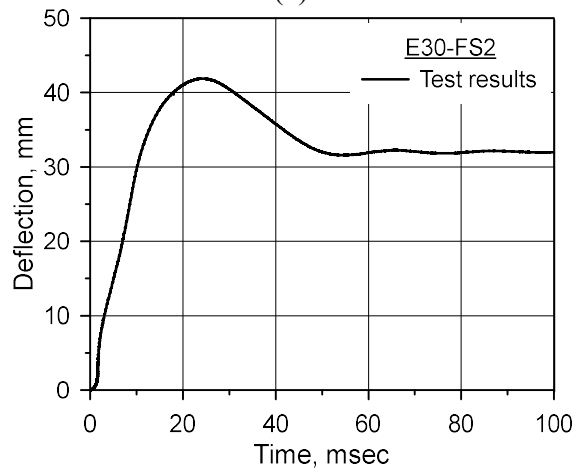


Figure 5.17 Force time histories of Ahn (2021); (a) E30-FS1; (b) E50-FS1;
(c) E30-FS2; (d) E50-FS2; (e) E30-FS3; (f) E50-FS3

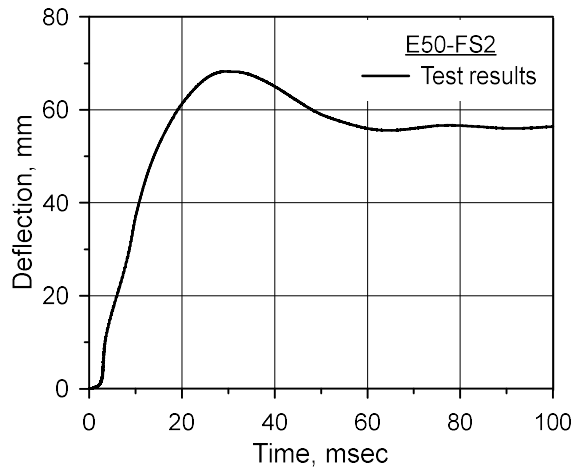




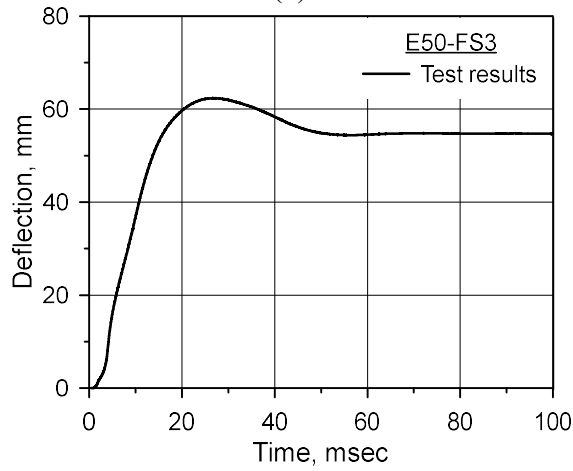
(b)



(c)



(d)



(e)

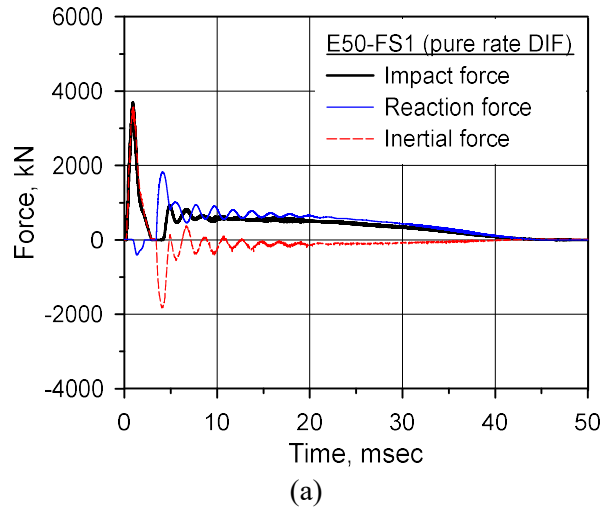
Figure 5.18 Central deflection time histories of Ahn (2021); (a) E30-FS1;
(b) E50-FS1; (c) E30-FS2; (d) E50-FS2; (e) E50-FS3

In this kind of test, the RC beams should satisfy the dynamic equilibrium expressed using Equation (5.4); here, F_{Impact} , $F_{Inertial}$, and $F_{Reaction}$ denote impact, inertial, and reaction forces, respectively. Figure 5.19, which

represents typical force time history data in FEA, showed the dynamic equilibrium was satisfied well in the FEA.

$$F_{Impact} = F_{Inertial} + F_{Reaction} \quad (5.4)$$

However, Figure 5.20 indicates that the dynamic equilibrium of all test cases was not satisfied, which means that the force data was not reliable. Pham et al. (2021) and Yu et al. (2021) argued that using acceleration signals might cause unreliable force measurements. Moreover, Ahn (2021) mentioned that the reaction force was inaccurately measured because the nuts at the upper supports were released during the test, so the initial tightened force at the supports was dissipated. Therefore, only the central deflection time histories, crack patterns, and local damages were compared with the FEA results.



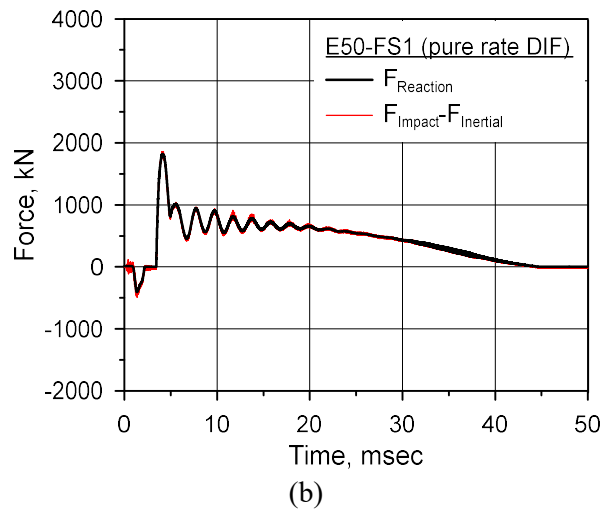
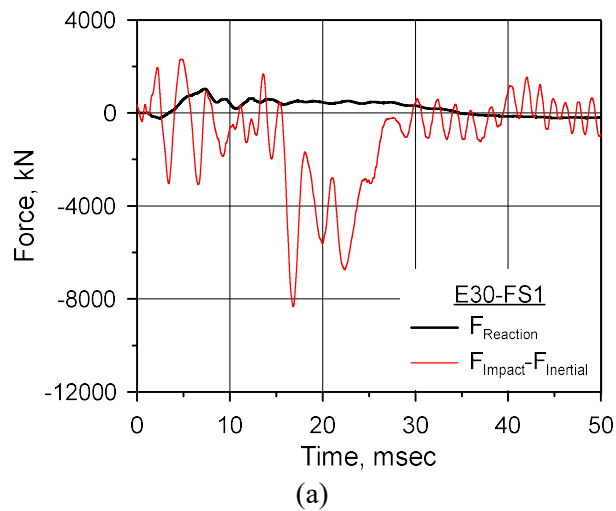
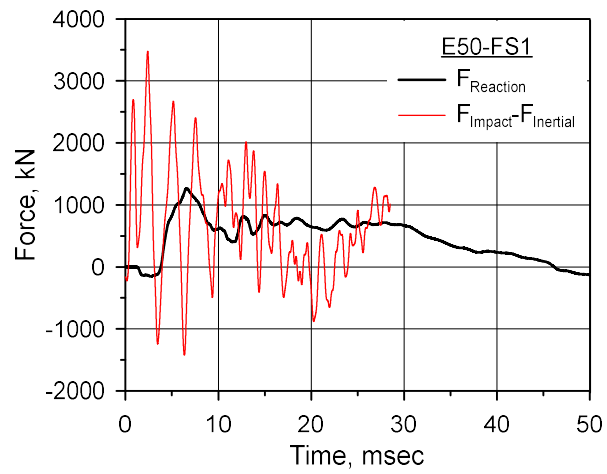


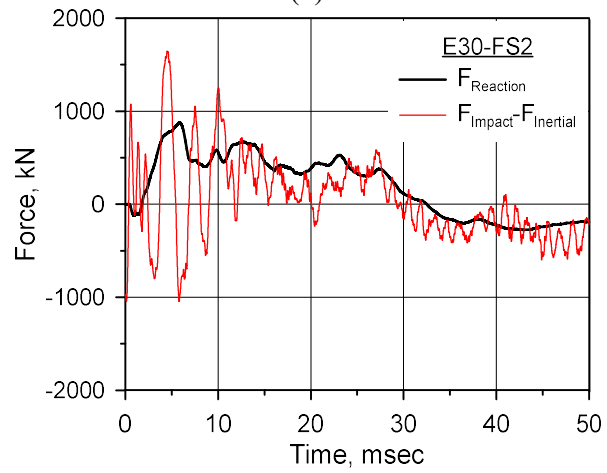
Figure 5.19 Typical force time history in the FEA using pure rate DIF

(a) Force time history; (b) Dynamic equilibrium assessment

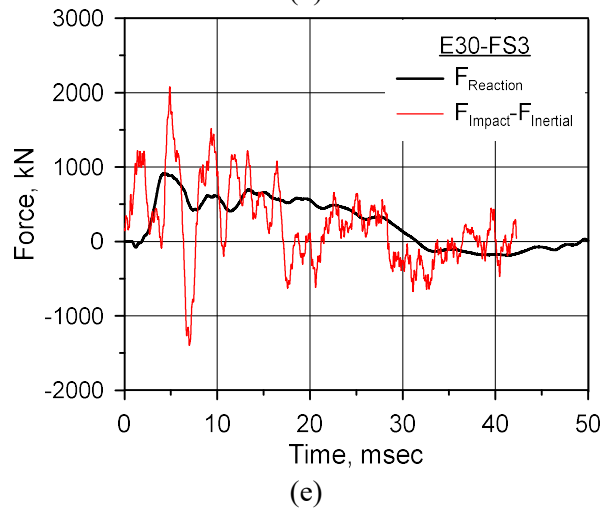
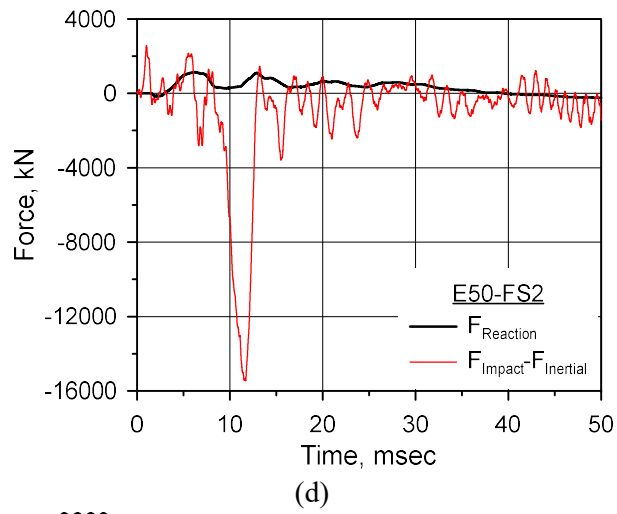




(b)



(c)



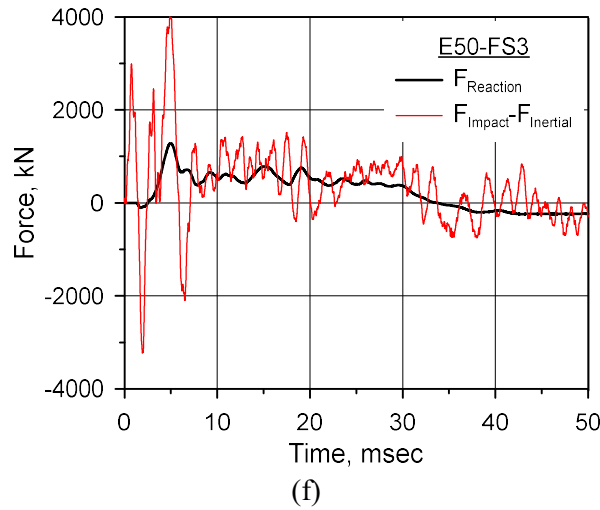


Figure 5.20 Dynamic equilibrium assessment; (a) E30-FS1; (b) E50-FS1;
(c) E30-FS2; (d) E50-FS2; (e) E30-FS3; (f) E50-FS3

5.2.2. Establishment of numerical model

5.2.2.1. Modeling details

Figure 5.21 shows the modeling parts and boundary conditions. A half model was established considering the symmetric condition. The drop-weight, RC beam, bottom and upper supports were included in the FEA model. The drop-weight was modeled using 20–50 mm solid elements, and concrete of RC beams was modeled using 25 mm solid elements. The 13 mm solid elements were used for the upper and bottom supports. All solid elements were eight-node solid elements with the reduced integration (ELFORM=1). Moreover, the reinforcing bars were modeled using Hughes-Liu beam elements of 25 mm (ELFORM=1), and the perfect bond was assumed between concrete and reinforcing bars using Constrained Beam in Solid option. A mesh test was conducted to determine the mesh size, and it was

confirmed that the variation of FEA results depending on the mesh size was not remarkable with the selected mesh size.

The symmetric boundary condition was input to the nodes on the symmetric plane. The nodes on boundary planes of the upper and bottom supports were constrained in all directions. Moreover, the displacement in the only vertical direction was allowed for the nodes at both ends of the drop-weight guide beam.

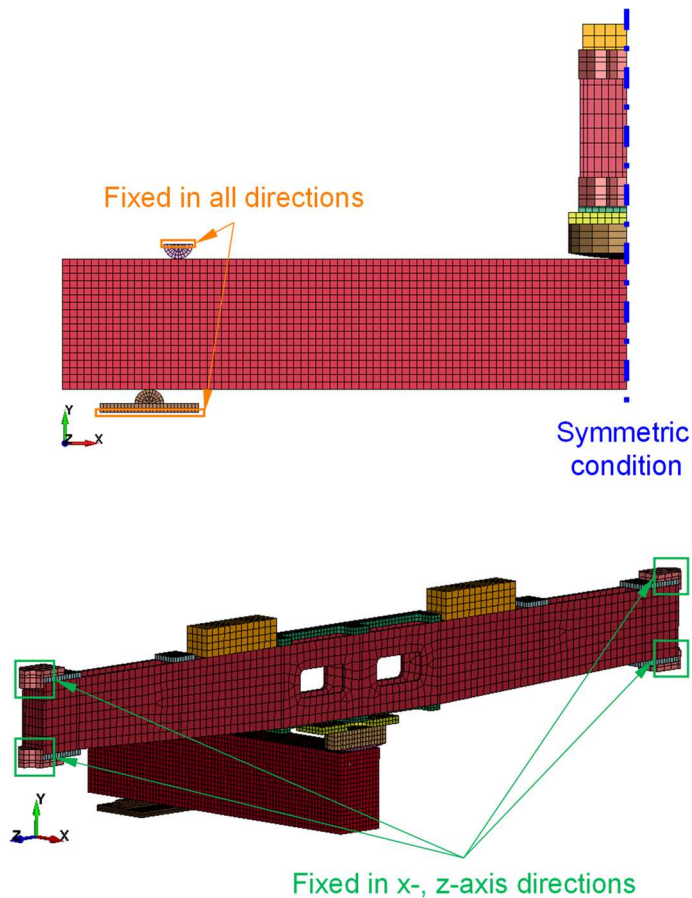


Figure 5.21 Modeling parts and boundary conditions

The initial velocity of the drop-weight was input to the FEA model considering the impact velocity in the tests. The gravity load was applied using body forces through the dynamic relaxation option. For contact conditions, the Automatic Surface to Surface option with a frictional coefficient of 0.2 was employed among the RC beam, drop-weight, and support parts, and the Automatic Single Surface Tied option was used for the contact among the parts of the drop-weight. The FEA was terminated at about 100 msec after the collision of the drop-weight with the RC beam.

5.2.2.2. *Material model for concrete*

The KCC model (MAT 72R3) was selected as the concrete constitutive model for the same reasons in Section 5.1. The FEA results showed that the ratio of hourglass energy to the internal energy of a concrete part was less than 3% for all cases, which indicated that the mesh-distortion was not significant in this problem. Therefore, no erosion criterion was applied to the FEA model.

Not only the suggested pure rate DIF model but also the compressive DIF models of ACI 349-13(γ_{ACI349}), ACI 370R-14 ($\gamma_{ACI370R}$), fib MC2010 (γ_{fib}), and UFC 3-340-02 were considered in the FEA. Figure 5.22 shows the considered compressive DIF models; here, the shaded range indicated where the pure rate DIF model is valid. Equations (5.5)–(5.7) indicate the DIF models of the design codes and guidelines; here, $\dot{\epsilon}_0 = 3 \times 10^{-5} \text{ s}^{-1}$ for γ_{fib} . Even though the strain rates of the DIF models of the design codes and guidelines are the axial strain rates, any correction for strain rates was not conducted. It is noted that the DIF model of UFC 3-340-02 is a function of the

average strain rate rather than the instantaneous strain rate, and the DIF model of fib MC2010 was determined to estimate the 15% value of data rather than the mean value (fib bulletin 70, 2013). Moreover, the tensile DIF of Xu and Wen (2013) was chosen as the DIF model of the tensile strength (see Equation (2.23) and Figure 5.4).

$$\gamma_{ACI349} = \min[0.9 + 0.1\{\log_{10} \dot{\epsilon} + 5\}, 1.25] \geq 1 \quad (5.5)$$

$$\gamma_{ACI370R} = \begin{cases} 0.00965 \log_{10} \dot{\epsilon} + 1.058 \geq 1 & \text{for } \dot{\epsilon} \leq 63.1 \text{ s}^{-1} \\ 0.758 \log_{10} \dot{\epsilon} - 0.289 \leq 2.5 & \text{for } 63.1 \text{ s}^{-1} < \dot{\epsilon} \end{cases} \quad (5.6)$$

$$\gamma_{fib} = \begin{cases} (\dot{\epsilon} / \dot{\epsilon}_0)^{0.014} & \text{for } 3 \times 10^{-5} \text{ s}^{-1} \leq \dot{\epsilon} \leq 30 \text{ s}^{-1} \\ 0.012 (\dot{\epsilon} / \dot{\epsilon}_0)^{1/3} & \text{for } 30 \text{ s}^{-1} < \dot{\epsilon} \leq 300 \text{ s}^{-1} \end{cases} \quad (5.7)$$

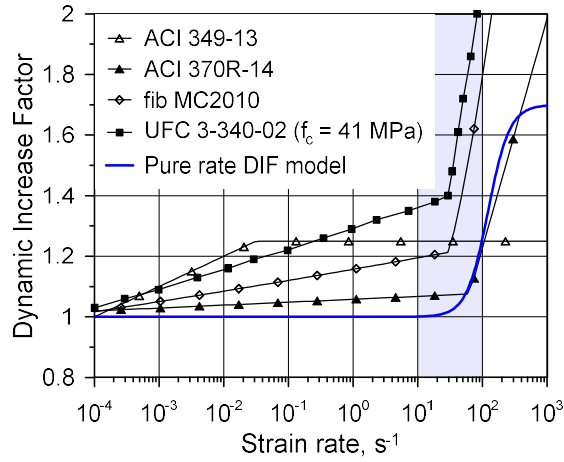


Figure 5.22 DIF models of compressive strength

Material model parameters are presented in Table 5.8. The static properties in Table 5.6 were used for the determination of the material model parameters. The tensile strength was determined using Equation (5.1).

Because there was no available triaxial material test data, the failure surfaces were determined using the auto-generating parameter values (Wu and Crawford, 2015). Figure 5.23 shows the determined failure surfaces.

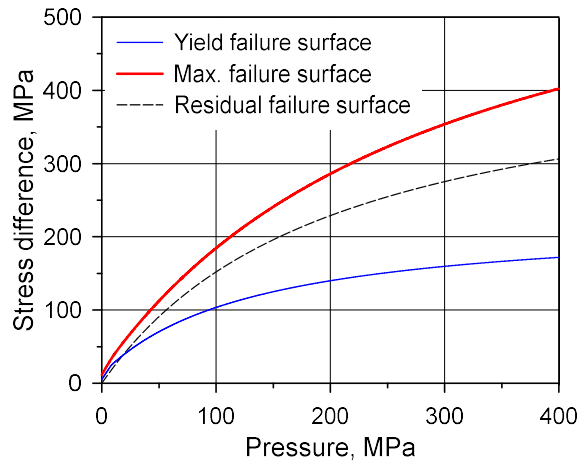


Figure 5.23 Failure surfaces

The localization width was determined as 30 mm considering the concrete element size. In a similar way to Section 5.1, the associativity parameter was determined to be 0.9, and the damage scaling factors b_1 and b_2 were calculated in accordance with Wu and Crawford (2015). As for b_3 , the default value was used.

For damage formulation, the $\eta - \lambda$ relationship of Markovich et al. (2011) was input to the FEA model for the same reasons in Section 5.1 (see Table 5.2 and Figure 5.6).

The EOS was determined in the same way in Section 5.1. The default EOS model was scaled down for the initial bulk modulus to be matched with the bulk modulus obtained from the material tests. The determined model parameters are listed in Table 5.9, and they were input to the tabulated compaction model (EOS 8).

Table 5.8 Concrete model parameter details (unit: ton, mm, sec)

Description	Symbol	Parameter value
Density	ρ_s	2.327×10^{-9}
Poisson's ratio	ν_s	0.1638
Uniaxial tensile strength	f_t	3.90
Maximum failure surface parameters	a_0	16.1980
	a_1	0.4463
	a_2	0.001475
Yield failure surface parameters	$a_{0,y}$	12.2361
	$a_{1,y}$	0.6250
	$a_{2,y}$	0.004699
Residual failure surface parameters	$a_{1,f}$	0.4417
	$a_{2,f}$	0.002159
Associativity parameter	ω	0.9
Localization width	w_{lz}	30
Damage scaling factors	b_1	1.1275
	b_2	2.0788
	b_3	1.15

Table 5.9 EOS model parameters

ε_v	p , MPa	K_u , MPa
0	0	13253
-0.0015	20	13253
-0.0043	43	13438
-0.0101	70	14111
-0.0305	132	16794
-0.0513	199	19477
-0.0726	283	22160
-0.0943	433	24186
-0.174	2527	54411
-0.208	3865	66264

5.2.2.3. Material model for reinforcing steel

The piecewise linear plasticity model (MAT 24) was selected as the constitutive model of reinforcing steels. The linear properties were assumed to be general characteristics of reinforcing bars, as shown in Table 5.10.

Table 5.10 Elastic linear material properties of reinforcing bars

Elastic modulus, GPa	Density, kg/m ³	Poisson's ratio
200	7850	0.29

The hardening models were determined based on the coupon test results, and they were input as user-defined curves. Figure 5.24 shows the isotropic hardening models of each reinforcing steel.

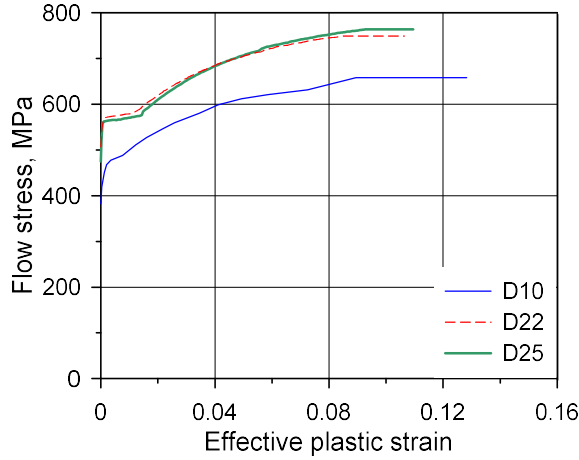


Figure 5.24 Strain-hardening models of reinforcing bars

The Malvar formula (Malvar, 1998; Malvar and Crawford, 1998) is one of the most widely used DIF models of reinforcing bars, and it is adopted in ACI 370R-14, fib MC2010, and UFC 3-340-02. Equation (5.8) shows the Malvar formula for the yield strength of rebars.

$$\gamma_y = \left(\frac{\dot{\epsilon}}{10^{-4}} \right)^{0.074 - 0.040 \frac{f_y}{414}} \quad (5.8)$$

where γ_y is the DIF of yield strength; f_y is yield strength of rebar in the unit of MPa; and $\dot{\epsilon}$ is strain rate in the unit of s^{-1} . Meanwhile, the piecewise linear plasticity model uses $\sqrt{\dot{\epsilon}_{ij}\dot{\epsilon}_{ij}}$ as the strain rate for a DIF. Therefore, the Malvar formula needed to be expressed using a function of $\sqrt{\dot{\epsilon}_{ij}\dot{\epsilon}_{ij}}$. In accordance with Fang and Wu (2017), Equation (5.8) can be expressed using Equation (5.9) with the assumption that the strain-hardening effect is not significant. Figure 5.25 shows the DIF models of rebar yield strength. The

static yield strengths in Table 5.7 were used for the calculation of the DIF models.

$$\gamma_y = \left(\sqrt{\frac{2}{3}} \frac{\sqrt{\dot{\epsilon}_{ij} \dot{\epsilon}_{ij}}}{10^{-4}} \right)^{0.074 - 0.040 \frac{f_y}{414}} \quad (5.9)$$

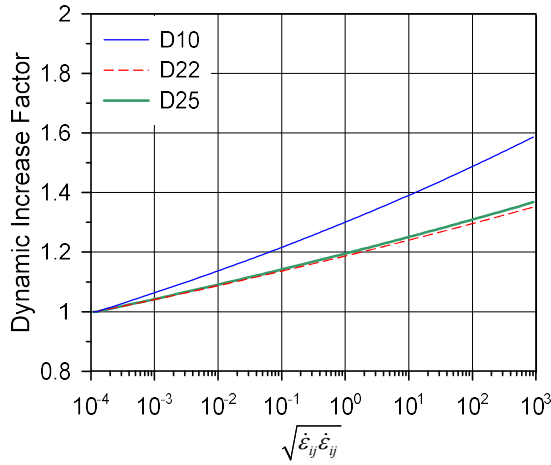


Figure 5.25 DIF models of reinforcing bars

5.2.2.4. Material models for drop-weight and supports

The drop-weight was assumed to be a rigid body by employing the rigid model (MAT 20). The model parameters for the contact condition are listed in Table 5.11. The density was adjusted so that the total mass of the drop-weight was 2.5 tons. The linear elastic model was used for the material model of the upper and bottom supports, and the material model parameters were determined using the general characteristics of steel, as shown in Table 5.12.

Table 5.11 Material properties of the drop-weight

Elastic modulus, GPa	Density, kg/m ³	Poisson's ratio
205	8499	0.29

Table 5.12 Material properties of the upper and bottom supports

Elastic modulus, GPa	Density, kg/m ³	Poisson's ratio
205	7850	0.29

5.2.3. Data acquisition

As the FEA results, the scaled damage measure (SDM, δ) contour and central deflection were obtained. The SDM is defined as Equation (5.10) (Wu and Crawford, 2015).

$$\delta = \frac{2\lambda}{\lambda + \lambda_m} \quad (5.10)$$

The SDM is zero when the stress state of an element is elastic, and it starts to increase after the stress state reaches the yield failure surface. Then, the SDM is equal to 1 when the stress state is on the maximum failure surface. As the stress state comes up to the residual failure surface, the SDM approaches 2. The central deflection was obtained from the displacement of the node at the center on the bottom surface of the beam. The SDM contour and central deflection were sampled with sampling rates of 2 kHz and 0.5 MHz, respectively.

5.2.4. Numerical analysis results

5.2.4.1. Crack pattern and local damage

Figure 5.26 shows the SDM contours at the termination of the FEA with the crack and local damage patterns in the tests; here, the displacement scale factor was set to be zero in the SDM contours. The FEA with the pure rate DIF well captured various types of damages observed in the tests. The local damages near the impact region in the FEA were similar to those in the tests, and shear plugs at the center of the beams were also well captured. Moreover, in the FEA, the diagonal cracks along the span of the beams were generated to be similar to the tests, and the negative bending cracks due to inertial forces in the early stage were also observed. Therefore, it was found that the FEA using the suggested pure rate DIF can appropriately predict the failure mode and behavior of the RC beams subjected to impact loadings.

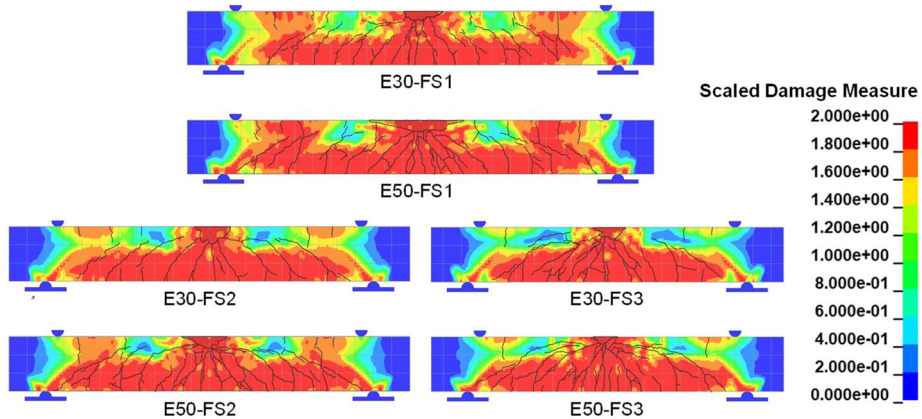
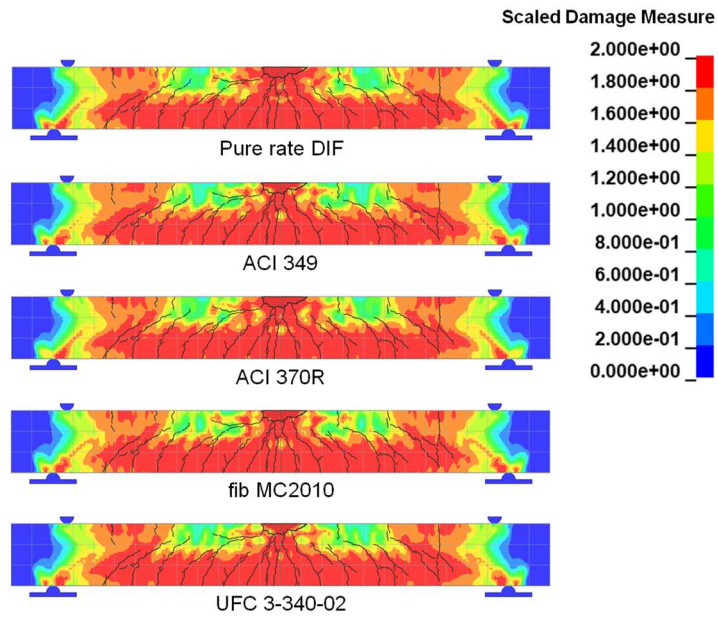
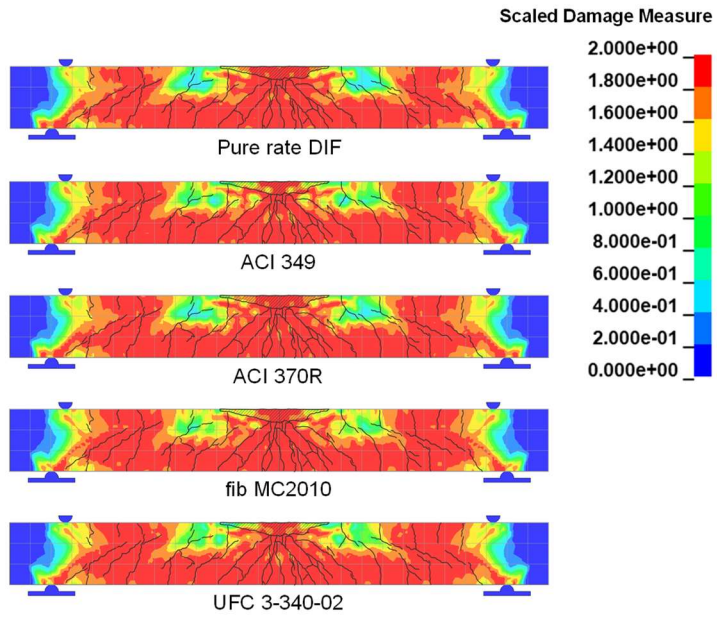


Figure 5.26 SDM contours of the FEA with the pure rate DIF

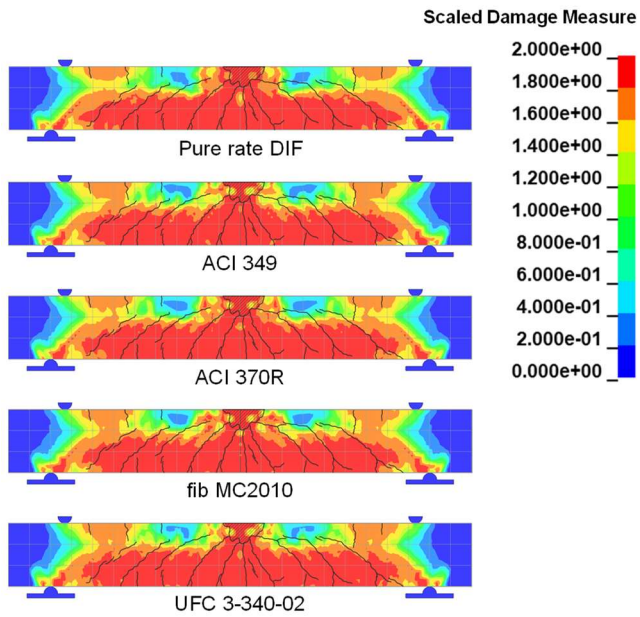
Figure 5.27 shows the comparison of the FEA results with the pure rate DIF to those with the DIFs in the design codes and guidelines. Overall damage patterns were similar regardless of the employed DIF models. The shear plugs, diagonal cracks, and negative bending cracks were observed in all DIF cases. However, the local damage areas of the FEA using DIF models in the design codes and guidelines were smaller than that of the FEA using the pure rate DIF. This was because the local damages were compressive damages that were caused by compressive stress waves due to the impact forces, and the DIF models in the design codes and guidelines have higher values compared with the pure rate DIF model.



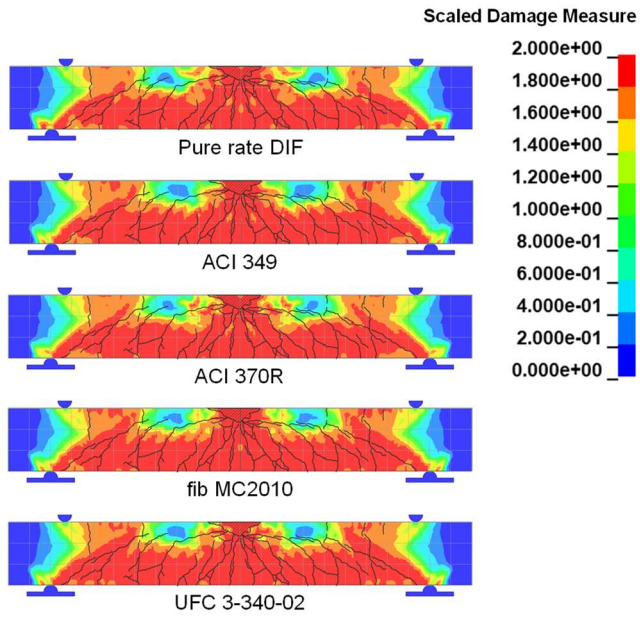
(a)



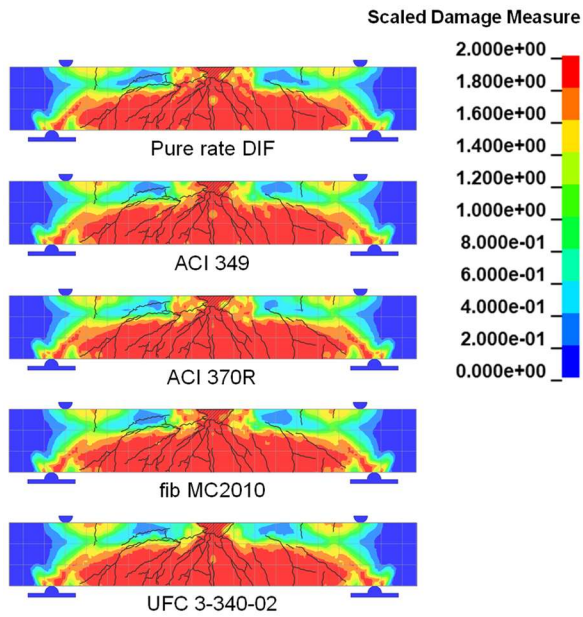
(b)



(c)



(d)



(e)

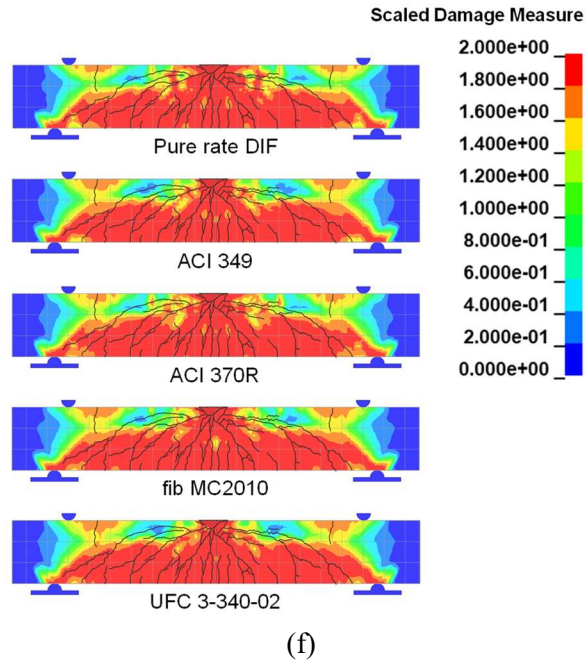
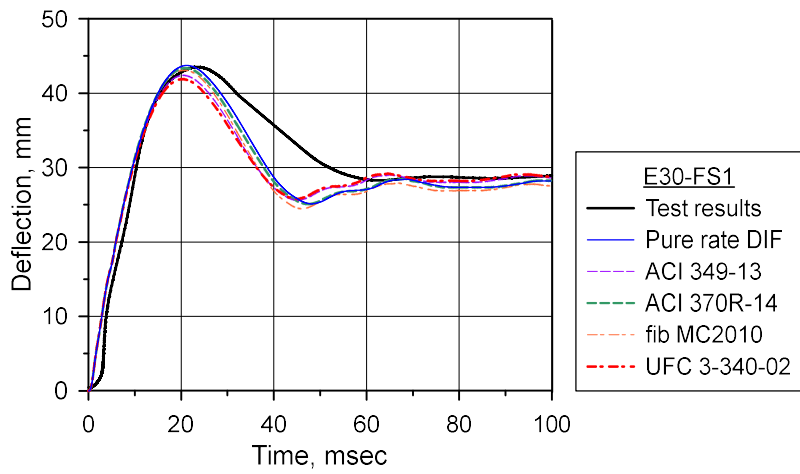


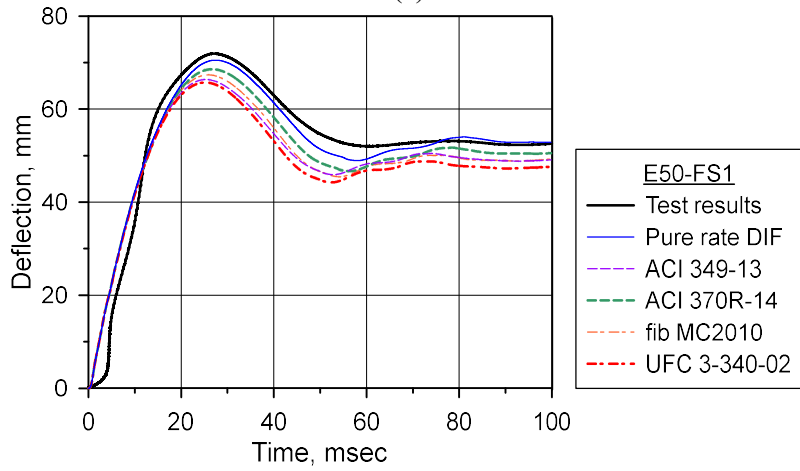
Figure 5.27 Comparison of SDM contours (a) E30-FS1; (b) E50-FS1; (c) E30-FS2; (d) E50-FS2; (e) E30-FS3; (f) E50-FS3

5.2.4.2. Displacement time history

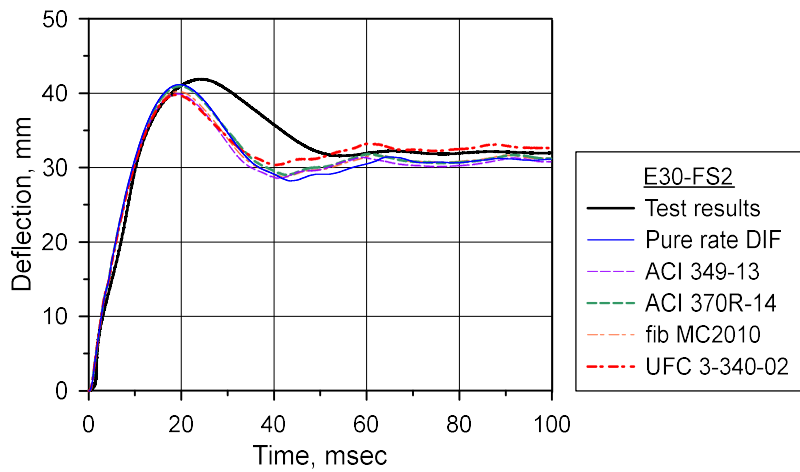
Figure 5.28 shows the central deflection time histories of the RC beams in the test and FEA. The results indicated that the FEA with the pure rate DIF showed good predictions for the deflection time histories. When the DIF model in the design codes and guidelines were used for the FEA, the predictive accuracy decreased, and the central deflection time histories were underestimated.



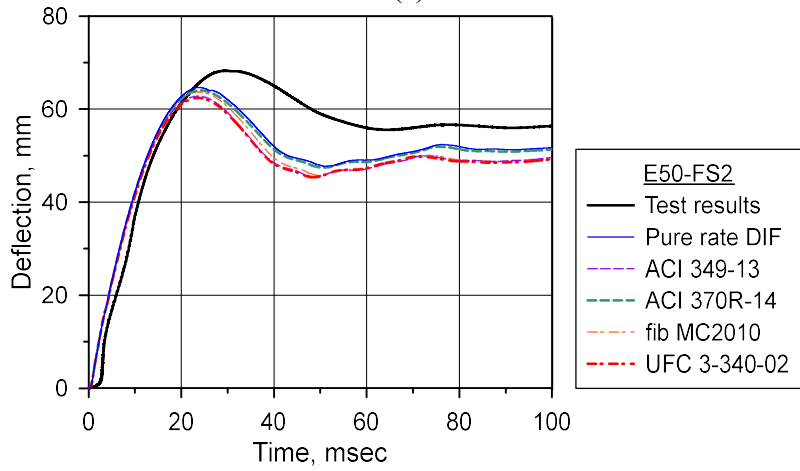
(a)



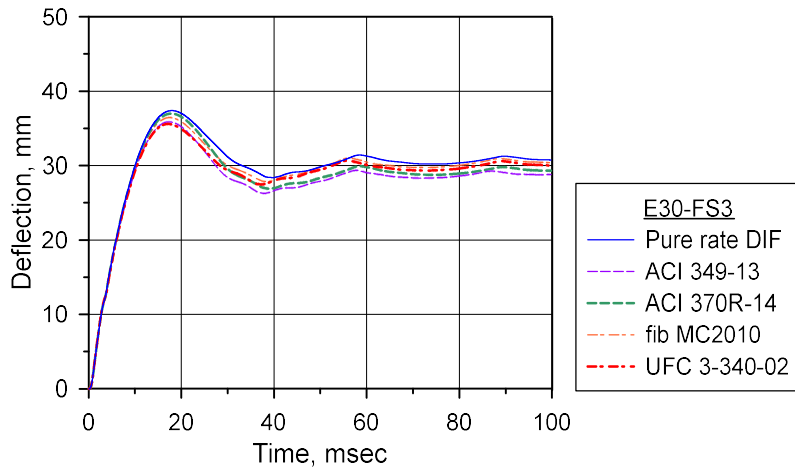
(b)



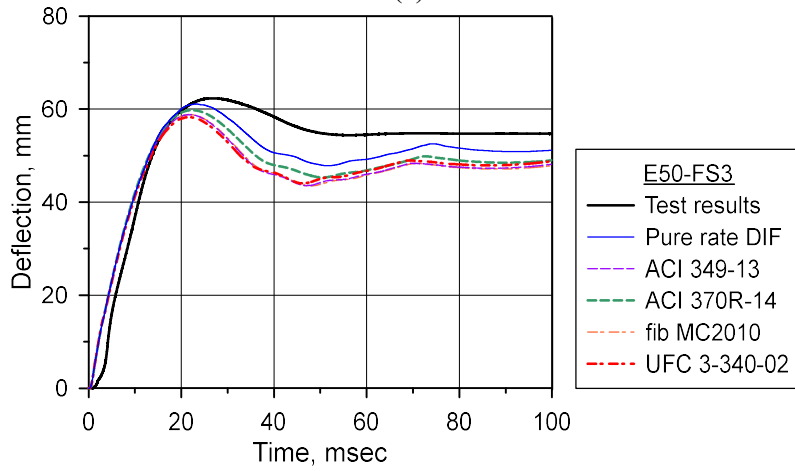
(c)



(d)



(e)



(f)

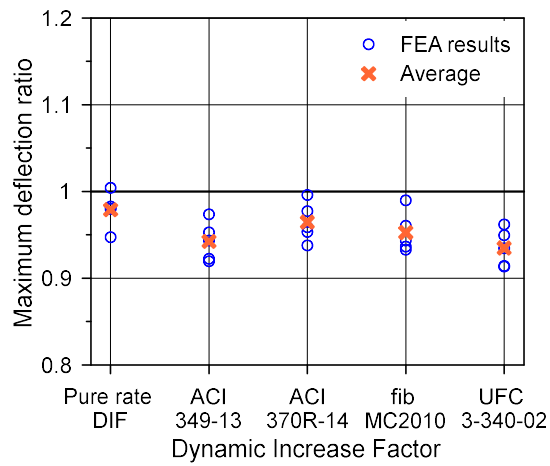
Figure 5.28 Central deflection time history (a) E30-FS1; (b) E50-FS1;
(c) E30-FS2; (d) E50-FS2; (e) E30-FS3; (f) E50-FS3

For quantitative analysis, the ratios of the maximum and residual deflections of the FEA to those of the tests were calculated using Equations (5.11) and (5.12), respectively, as shown in Figure 5.29. The mean and COV of the deflection ratios were calculated, and they are listed in Tables 5.13 and 5.14.

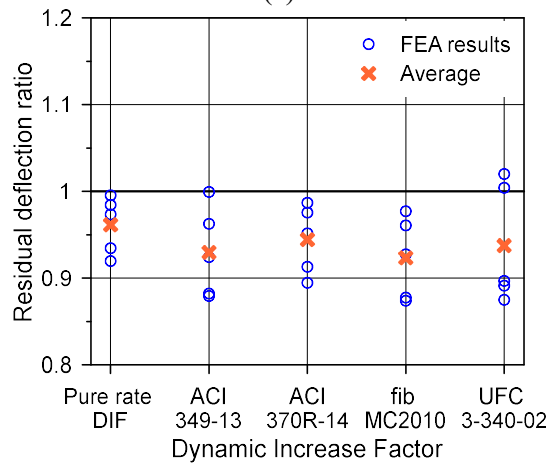
$$R_{d,max} = \Delta_{FEA,max} / \Delta_{test,max} \quad (5.11)$$

$$R_{d,residual} = \Delta_{FEA,residual} / \Delta_{test,residual} \quad (5.12)$$

where $R_{d,max}$ and $R_{d,residual}$ denote the maximum and residual deflection ratios, respectively; $\Delta_{test,max}$ and $\Delta_{test,residual}$ are the maximum and residual deflections in the tests, respectively; and $\Delta_{FEA,max}$ and $\Delta_{FEA,residual}$ are the maximum and residual deflections in the FEA, respectively. The FEA using the pure rate DIF model predicted the maximum and residual deflections with high accuracies of about 98% and 96% on average, respectively. Moreover, the COV values were about 2% and 3% for the maximum and residual deflection ratios, respectively, which means that the prediction accuracies were consistent. On the other hand, the predictive accuracies decreased in the FEA cases using the other DIF models compared to the FEA using the pure rate DIF, as mentioned earlier. Inaccurate DIF models caused overestimations of the concrete strength under impact loadings, thereby leading to overestimations of the impact resistances of the RC beams. Consequently, it was confirmed that the impact behavior of concrete structures can be predicted appropriately using the proposed pure rate DIF model.



(a)



(b)

Figure 5.29 Distribution of deflection ratios; (a) Maximum defection ratio;
(b) Residual deflection ratio

Table 5.13 Mean and COV values of the maximum deflection ratios

	Pure rate DIF	ACI 349- 13	ACI 370R-14	fib MC2010	UFC 3- 340-02
Mean	0.979	0.942	0.965	0.953	0.935
COV	0.019	0.021	0.021	0.022	0.021

Table 5.14 Mean and COV values of the residual deflection ratios

	Pure rate DIF	ACI 349- 13	ACI 370R-14	fib MC2010	UFC 3- 340-02
Mean	0.961	0.930	0.944	0.923	0.937
COV	0.031	0.050	0.038	0.046	0.066

5.3. Concluding remarks

In this chapter, a series of numerical analyses were conducted to verify and apply the pure rate DIF model proposed in Chapter 4. In Section 5.1, numerical simulations of the conventional SHPB test in Chapter 4 were performed to verify the pure rate DIF model. Both pure rate and apparent DIF models suggested in Chapter 4 were considered in the FEA. The apparent DIF–effective deviatoric strain rate relationship, as well as the apparent strength, was obtained as the analysis results. The FEA results indicated that the apparent DIF–effective deviatoric strain rate relationship of the FEA using the pure rate DIF coincided with the apparent DIF model observed in the conventional SHPB test. This means that the dynamic compressive behavior of concrete can be predicted with high accuracy using the pure rate DIF model. Therefore, the pure rate DIF model was found to be valid. On the other hand, when the apparent DIF model was used for the FEA, the apparent DIF of the FEA showed higher values than the apparent DIF model of the tests. In other words, the concrete dynamic strength was overestimated with the apparent DIF model.

In Section 5.2, a numerical example of the drop-weight impact tests for RC beams was introduced to apply the pure rate DIF to an FEA. In this example, the various DIF models in design codes and guidelines as well as the pure rate DIF model were considered in the FEA models. The FEA results were compared with the test results in terms of the crack patterns, local damages and central deflections. The FEA results indicated that the impact behavior, such as crack patterns, local damages and deflection time histories,

was well captured in the FEA using the pure rate DIF. Therefore, it was found that the impact behavior and resistance of concrete structures can be well predicted using the pure rate DIF model. On the other hand, the local damages and central deflections were underestimated in the FEA using the DIF models of the design codes and guidelines. This means that using the DIF models obtained from the conventional SHPB test might lead to an overestimation of impact resistance of concrete structures.

In conclusion, the suggested methodology for evaluating the pure rate DIF and the proposed pure rate DIF model were found to be valid. Therefore, the findings of this study are expected to be applied to the various studies on the material and structural behavior under extreme loadings.

6. Conclusions

6.1. Summary and major findings of this study

This study performed a systematic investigation to propose the methodology for evaluation of the pure rate DIF and to suggest the pure rate DIF model through the confined SHPB test for concrete.

First of all, this study investigated concrete compressive behavior with lateral confinements using a numerical model. From the result of the strain-rate-independent case, two characteristics of the compressive behavior of concrete under lateral confinements were observed; (1) the loading path was in contact with the failure surface at a failure point, and (2) the stress state of the specimen was below the failure surface except for the failure point. The methodology to evaluate pure rate DIF was proposed with the assumption that these two characteristics are valid in the strain-rate-dependent cases, and its implementing procedure was also suggested based on the bisection method. Then, the input DIF values were estimated using the proposed methodology for the FEA results of the strain-rate-dependent cases. The estimation results indicated that the proposed methodology was valid.

Secondly, three kinds of experiments were performed: the conventional SHPB test, static confined compressive test, and confined SHPB test. The conventional SHPB test was performed to obtain the apparent DIF data and to compare it with the pure rate DIF data. Moreover, the static confined compressive test was conducted to determine the static failure surface of the

specimens. In the static confined compressive test, the loading path of the specimens showed a similar tendency to that of the strain-rate-independent case in Chapter 3. The determined static failure surface was used for the assessment of the pure rate DIF. Subsequently, the confined SHPB test was conducted to obtain the pure rate DIF–effective deviatoric strain rate data. The specimens showed similar behavior to that of the strain-rate-dependent cases in Chapter 3. The test results indicated that the pure rate DIF exhibited smaller values than the apparent DIF of the conventional SHPB test, which means using the apparent DIF results in unsafe design and analysis of concrete structures under extreme loadings. As final results of the experimental work, the apparent and pure rate DIF models were suggested based on the conventional and confined SHPB test results, respectively.

Lastly, two kinds of numerical analyses were performed to verify and implement the pure rate DIF model proposed in Chapter 4: FEA on the conventional SHPB tests and drop-weight impact tests for RC beams. Numerical analysis results on the conventional SHPB test indicated that the FEA using the pure rate DIF predicted the apparent DIF–effective deviatoric strain rate relationship with good accuracy. Therefore, the proposed pure rate DIF was found to be valid. However, the FEA using the apparent DIF showed higher values than the apparent DIF model, as expected. Numerical analysis results on the drop-weight impact tests indicated that the FEA using the pure rate DIF model well captured the crack pattern, local damage, and deflection time history of the RC beams. Therefore, it was found that the behavior of concrete structures under extreme loadings can be well predicted with FEA

using the proposed pure rate DIF model. However, the FEA using the DIF models in the design codes and guidelines showed less prediction accuracy.

6.2. Recommendations for further studies

For widespread application and extension of the findings of this study, the following topics are recommended for further studies.

- Since this study was focused on the suggestion and verification of the methodology to evaluate the pure rate DIF, the research was conducted with only one type of concrete specimen without consideration of the important parameters such as strength, water contents, and aggregate characteristics. In particular, this study tested only saturated specimens to control shrinkage and to ensure a snug fit. Therefore, the effect of important parameters on the pure rate DIF needs to be investigated for the development of a complete pure rate DIF model of concrete.
- For the same reason as above, this study considered only concrete, instead of covering various cementitious materials. It is recommended to investigate the strain-rate-dependent characteristics of various high-performance cementitious materials developed for protective structures against extreme loadings employing the findings of this study.
- A standard confined SHPB test procedure should be developed to obtain and accumulate consistent test data. As part of this, the effects of test conditions on the test results, such as frictional effect or size effect, need to be investigated.

- Conventional SHPB tests have the advantage of being more convenient and less expensive compared to confined SHPB tests. Therefore, it is recommended to develop the methodology for converting the apparent DIF data to the pure rate DIF data by investigating a correlation between the conventional and confined SHPB test results.
- This study investigated the strain-rate-dependency mainly focusing on strength and failure surfaces. However, because a delay in damage accumulation is also an important strain-rate-dependent characteristic, it is worth investigating the strain-rate-dependency of damage accumulation using the static and dynamic confined compressive tests.
- Structural elements subjected to extreme loadings are under various triaxial stress states due to phase change and superposition of stress waves. However, this study considered only the loading path under the uniaxial strain state due to a limitation of the test apparatus, so it is not verified that the suggested pure rate DIF model can be applied to various stress states. Therefore, the effect of loading paths on the strain-rate-dependency of concrete needs to be investigated using active-confined SHPB tests or three-dimensional SHPB tests.
- The behavior of various concrete structures subjected to extreme loadings needs to be investigated through FEA with the proposed pure rate DIF model. Furthermore, studies on the development of design or rehabilitation techniques for concrete structures against extreme loadings are necessary.

Reference

- ACI Committee 349. Code Requirements for Nuclear Safety-Related Concrete Structures (ACI 349-13) & Commentary. American Concrete Institute. Farmington Hills, MI, U.S. 2014.
- ACI Committee 370. Report for the Design of Concrete Structures for Blast Effects. American Concrete Institute. Farmington Hills, MI, U.S. 2014.
- Ahn, H. Effect of flexural stiffness on impact behavior of RC beam subjected to low-velocity impact loading. MS thesis. Department of Civil & Environmental Engineering, Seoul National University. Seoul, South Korea. 2021.
- ASTM A182. Standard Specification for Forged or Rolled Alloy and Stainless Steel Pipe Flanges, Forged Fittings, and Valves and Parts for High-Temperature Service. ASTM International. West Conshohocken, PA, U.S. 2020.
- ASTM A370. Standard Test Methods and Definitions for Mechanical Testing of Steel Products. ASTM International. West Conshohocken, PA, U.S. 2019.
- ASTM C192. Standard Practice for Making and Curing Concrete Test Specimens in the Laboratory. ASTM International. West Conshohocken, PA, U.S. 2019.

- ASTM C39. Standard test method for compressive strength of cylindrical concrete specimens. ASTM International. West Conshohocken, PA, U.S. 2020.
- Borrvall, T. and W. Riedel. The RHT concrete model in LS-DYNA. Proceedings of the 8th European LS-DYNA User Conference. 2011.
- Chen, W.W. and B. Song. Split Hopkinson (Kolsky) bar: design, testing and applications. Springer Science & Business Media, New York, NY, U.S. 2010.
- Chun, B., W. Shin, T. Oh, and D.-Y. Yoo. Dynamic compressive and flexural behaviors of ultra-rapid-hardening mortar containing polyethylene fibers. Archives of Civil and Mechanical Engineering, 2021. 21, 75.
- Fang, Q. and H. Wu. Concrete Structures Under Projectile Impact, Springer, Beijing, China. 2017.
- fib Bulletin 65. Model Code 2010 Final draft Volume 1. fib Fédération internationale du béton, Lausanne, Switzerland. 2012.
- fib Bulletin 66. Model Code 2010 Final draft Volume 2. fib Fédération internationale du béton, Lausanne, Switzerland. 2012.
- fib Bulletin 70. Code-type models for concrete behaviour, Background of MC2010. fib Fédération internationale du béton, Lausanne, Switzerland. 2013.

- Flores-Johnson, E.A. and Q.M. Li. Structural effects on compressive strength enhancement of concrete-like materials in a split Hopkinson pressure bar test. *International Journal of Impact Engineering*, 2017. 109: p. 408-418.
- Forquin, P., E. Piotrowska, and G. Gary. Dynamic testing of concrete under high confined pressure. Influence of saturation ratio and aggregate size. *EPJ Web of Conferences*. 2015.
- Forquin, P., G. Gary, and F. Gatuingt. A testing technique for concrete under confinement at high rates of strain. *International Journal of Impact Engineering*, 2008. 35(6): p. 425-446.
- Forquin, P., K. Safa, and G. Gary. Influence of free water on the quasi-static and dynamic strength of concrete in confined compression tests. *Cement and Concrete Research*, 2010. 40(2): p. 321-333.
- Forrestal, M., T. Wright, and W. Chen. The effect of radial inertia on brittle samples during the split Hopkinson pressure bar test. *International Journal of Impact Engineering*, 2007. 34(3): p. 405-411.
- Frew, D., M.J. Forrestal, and W. Chen. Pulse shaping techniques for testing brittle materials with a split Hopkinson pressure bar. *Experimental Mechanics*, 2002. 42(1): p. 93-106.
- Gebbeken, N., and M. Ruppert. A new material model for concrete in high-dynamic hydrocode simulations. *Archive of Applied Mechanics*, 2000. 70(7): p. 463-478.

- Gebbeken, N., and S. Greulich. A new material model for SFRC under high dynamic loadings. Proceedings 11th International Symposium. Interaction of the Effects of Munitions with Structures (ISIEMS), Mannheim, Germany. 2003.
- Gong, J.C. and L.E. Malvern. Passively confined tests of axial dynamic compressive strength of concrete. *Experimental Mechanics*, 1990. 30(1): p. 55-59.
- Grassl, P. and M. Jirásek. Damage-plastic model for concrete failure. *International Journal of Solids and Structures*, 2006. 43(22): p. 7166-7196.
- Grassl, P., D. Xenos, U. Nyström, R. Rempling, and K. Gylltoft. CDPM2: A damage-plasticity approach to modelling the failure of concrete. *International Journal of Solids and Structures*, 2013. 50(24): p. 3805-3816.
- Grassl, P., U. Nyström, R. Rempling, and K. Gylltoft. A damage-plasticity model for the dynamic failure of concrete. *Proceedings of 8th International Conference on Structural Dynamics*, Belgium. 2011.
- Grote, D.L., S.W. Park, and M. Zhou. Dynamic behavior of concrete at high strain rates and pressures: I. experimental characterization. *International Journal of Impact Engineering*, 2001. 25(9): p. 869-886.

- Hao, Y., H. Hao, G.P. Jiang, and Y. Zhou. Experimental confirmation of some factors influencing dynamic concrete compressive strengths in high-speed impact tests. *Cement and Concrete Research*, 2013. 52: p. 63-70.
- Heard, W.F., B.E. Martin, X. Nie, and T. Slawson. Annular pulse shaping technique for large-diameter Kolsky bar experiments on concrete. *Experimental Mechanics*, 2014. 54(8): p. 1343-1354.
- Holmquist, T.J., G.R. Johnson, and W.H. Cook. A computational constitutive model for concrete subjected to large strains, high strain rate, and high pressures. *Proceedings of 14th International Symposium on Ballistics*. 1993.
- Kim, D.J., K. Sirijaroonchai, S. Ek-Tawil, and A.E. Naaman. Numerical simulation of the split Hopkinson pressure bar test technique for concrete under compression. *International Journal of Impact Engineering*, 2010. 37(2): p. 141-149.
- Kim, K.-M., S. Lee, and J.-Y. Cho. Effect of maximum coarse aggregate size on dynamic compressive strength of high-strength concrete. *International Journal of Impact Engineering*, 2019. 125: p. 107-116.
- Kim, K.-M., S. Lee, and J.-Y. Cho. Influence of friction on the dynamic increase factor of concrete compressive strength in a split Hopkinson pressure bar test. *Cement and Concrete Composites*, 2022. 129: 104517.

- Kolsky, H. An investigation of the mechanical properties of materials at very high rates of loading. *Proceedings of the Physical Society*, 1949. 62(11): p. 676-700.
- Kong, X.Q. Fang, Q.M. Li, H. Wu, and J.E. Crawford. Modified K&C model for cratering and scabbing of concrete slabs under projectile impact. *International Journal of Impact Engineering*, 2017. 108: p.217-228.
- Lee, S., K.-M. Kim, J. Park, and J.-Y. Cho. Pure rate effect on the concrete compressive strength in the split Hopkinson pressure bar test. *International Journal of Impact Engineering*, 2018. 113: p. 191-202.
- Li, Q.M. and H. Meng. About the dynamic strength enhancement of concrete-like materials in a split Hopkinson pressure bar test. *International Journal of Solid Structures*, 2003. 40: p. 343-360.
- Li, Q.M., Y. Lu, and H. Meng. Further investigation on the dynamic compressive strength enhancement of concrete-like materials based on split Hopkinson pressure bar tests. Part II: numerical simulations. *International Journal of Impact Engineering*, 2009. 36(12): p. 1335-1345.
- Liu, F. and Q.M. Li. Strain-rate effect on the compressive strength of brittle materials and its implementation into material strength model. *International Journal of Impact Engineering*, 2019. 130: p. 113-123.
- Lok, T., X.B. Li, D. Liu, and P.J. Zhao. Testing and response of large diameter brittle materials subjected to high strain rate. *Journal of Materials in Civil Engineering*, 2002. 14(3): p. 262-269.

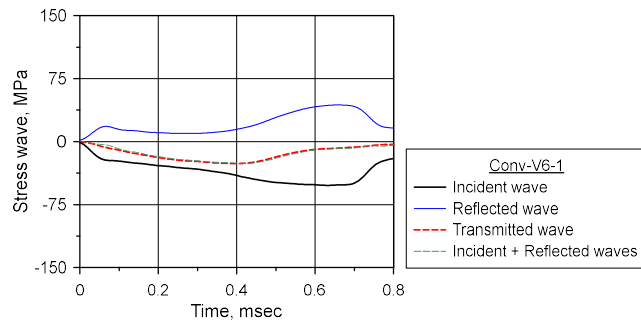
- Lu, Y.B. and Q.M. Li. A correction methodology to determine the strain-rate effect on the compressive strength of brittle materials based on SHPB testing. *International Journal of Protective Structures*, 2011. 2(1): p. 127-138.
- Magallanes, J.M., Y. Wu, L.J. Malvar, and J.E. Crawford. Recent improvements to release III of the K&C concrete model. *Proceedings of 11th International LS-DYNA Users Conference*, Livermore Software Technology Corporation, Livermore, CA. 2010.
- Malvar, L.J. and J.E. Crawford. Dynamic increase factors for steel reinforcing bars. 28th DDESB Seminar. Orlando, USA. 1998.
- Malvar, L.J. Review of static and dynamic properties of steel reinforcing bars. *ACI Materials Journal*, 1998. 95(5): p. 609-616.
- Malvar, L.J., J.E. Crawford, J.W. Wesevich, and D. Simons. A plasticity concrete material model for DYNA3D. *International Journal of Impact Engineering*, 1997. 19(9-10): p. 847-873.
- Markovich, N., E. Kochavi, and G. Ben-Dor. An improved calibration of the concrete damage model. *Finite Elements in Analysis and Design*, 2011. 47(11): p. 1280-1290.
- Murray, Y.D. *Users Manual for LS-DYNA Concrete Material Model 159*. FHWA-HRT-05-062, McLean, VA, U.S. 2007

- Murray, Y.D., A. Abu-Odeh, and R. Bligh. Evaluation of LS-DYNA Concrete Material Model 159. FHWA-HRT-05-063, McLean, VA, U.S. 2007
- Ottosen, N. A failure criterion for concrete. *Journal of Engineering Mechanics*, 1977. 103: p. 527-535.
- Pham, T.M., W. Chen, and H. Hao. Review on impact response of reinforced concrete beams: Contemporary understanding and unsolved problems. *Advances in Structural Engineering*, 2021. 24(10): p. 2282-2303.
- Piotrowska, E., P. Forquin, and Y. Malecot. Experimental study of static and dynamic behavior of concrete under high confinement: Effect of coarse aggregate strength. *Mechanics of Materials*, 2016. 92: p. 167-174.
- Riedel, W., N. Kawai, and K.-i. Kondo. Numerical assessment for impact strength measurements in concrete materials. *International Journal of Impact Engineering*, 2009. 36(2): p. 283-293.
- Ross, C.A., J.W. Tedesco, and S.T. Kuennen. Effects of strain rate on concrete strength. *ACI Materials Journal*, 1995. 92(1): p. 37-47.
- Schwer, L. The Winfrith Concrete Model : Beauty or beast? Insights into the Winfrith concrete model. *Proceedings of 8th European LS-DYNA Users Conference*, Strasbourg. 2011
- Timoshenko, S.P. and J.N. Goodier. *Theory of Elasticity*. McGraw-Hill. Singapore. 1987.

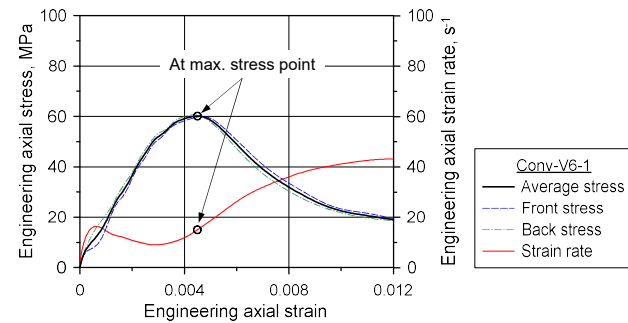
- Unified Facilities Criteria (UFC) 3-340-02. Structures to Resist the Effects of Accidental Explosions. Department of Defense. Washington D.C., U.S. 2008.
- Wu, Y. and J.E. Crawford. Numerical modeling of concrete using a partially associative plasticity model. *Journal of Engineering Mechanics*, 2015. 141(12): 04015051.
- Xu, H. and H.M. Wen. Semi-empirical equations for the dynamic strength enhancement of concrete-like materials. *International Journal of Impact Engineering*, 2013. 60: p. 76-81.
- Yu, Y., S. Lee, and J.-Y. Cho. Deflection of reinforced concrete beam under low-velocity impact loads. *International Journal of Impact Engineering*, 2021. 154: 103878.
- Zhang, M., H.J. Wu, Q.M. Li, and F.L. Huang. Further investigation on the dynamic compressive strength enhancement of concrete-like materials based on split Hopkinson pressure bar tests. Part I: experiments. *International Journal of Impact Engineering*, 2009. 36(12): p. 1327-1334.

Appendix A

Experimental Results of Conventional SHPB Tests

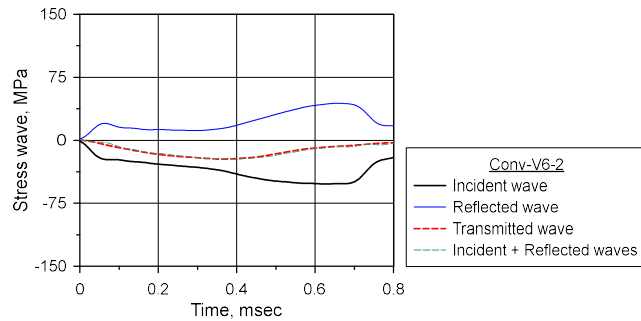


(a)

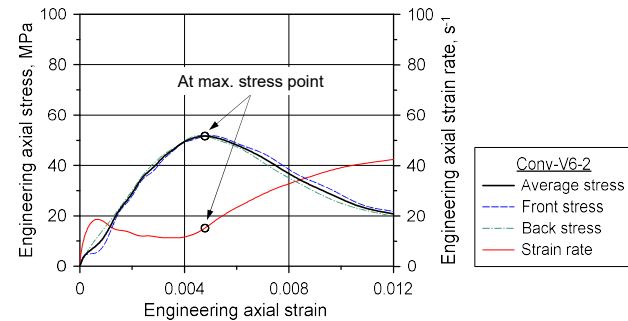


(b)

Figure A.1 Test results of Conv-V6-1; (a) Stress waves; (b) Axial stress–strain curve

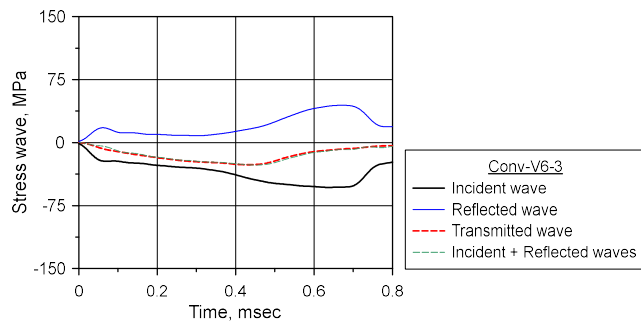


(a)

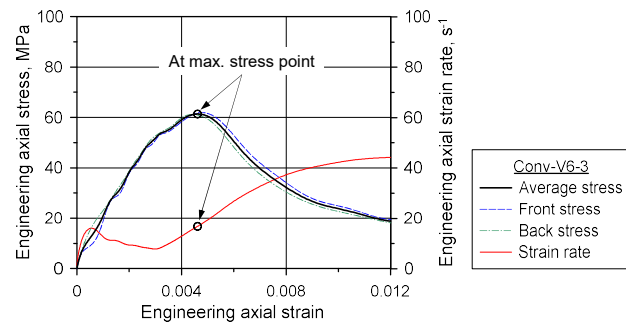


(b)

Figure A.2 Test results of Conv-V6-2; (a) Stress waves; (b) Axial stress–strain curve

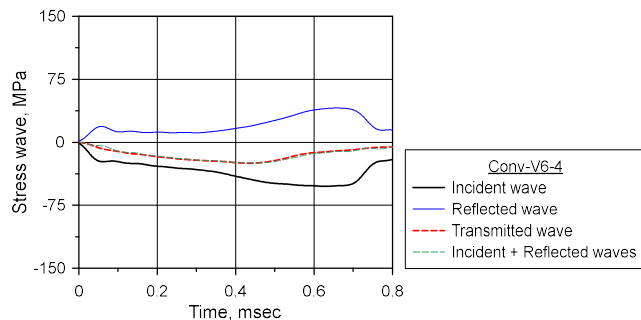


(a)

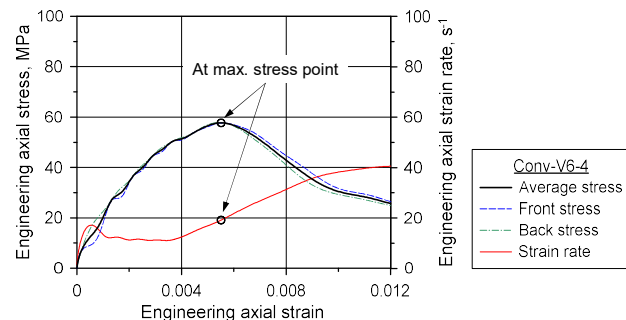


(b)

Figure A.3 Test results of Conv-V6-3; (a) Stress waves; (b) Axial stress–strain curve

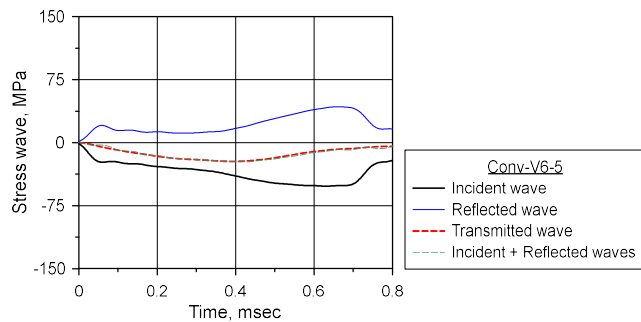


(a)

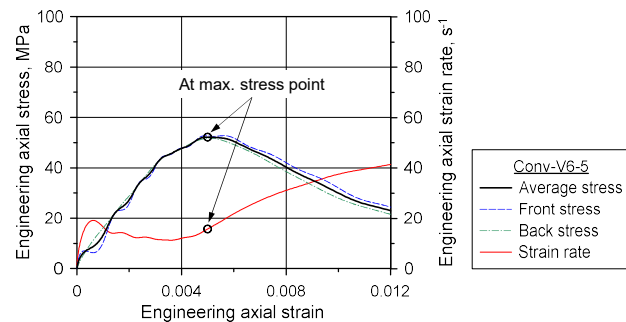


(b)

Figure A.4 Test results of Conv-V6-4; (a) Stress waves; (b) Axial stress–strain curve

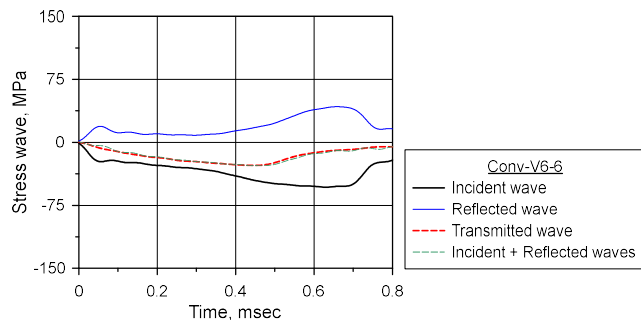


(a)

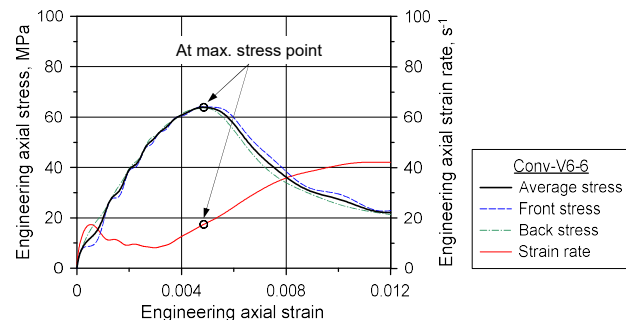


(b)

Figure A.5 Test results of Conv-V6-5; (a) Stress waves; (b) Axial stress–strain curve

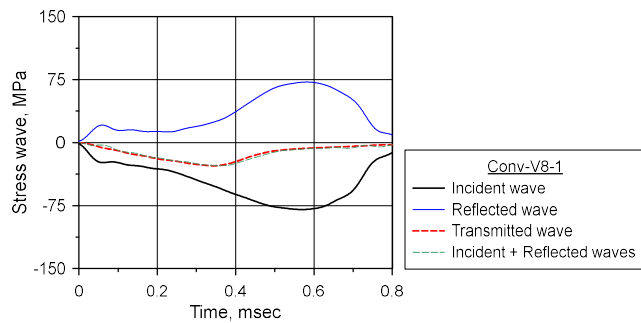


(a)

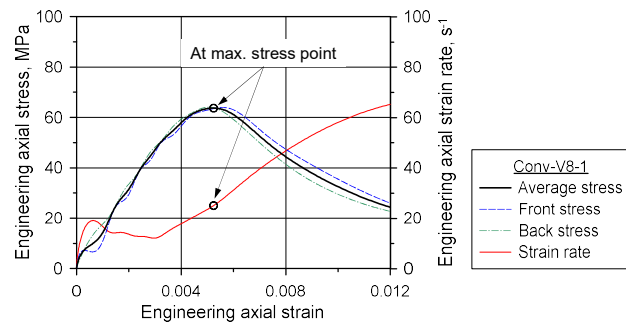


(b)

Figure A.6 Test results of Conv-V6-6; (a) Stress waves; (b) Axial stress–strain curve

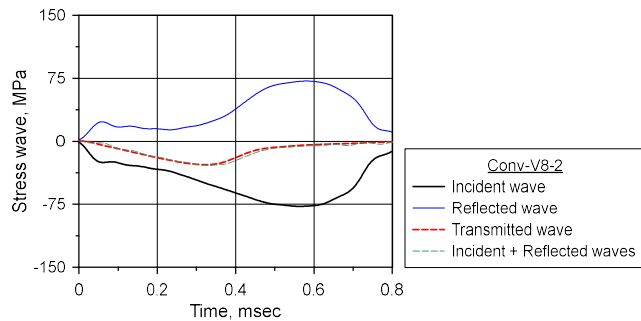


(a)

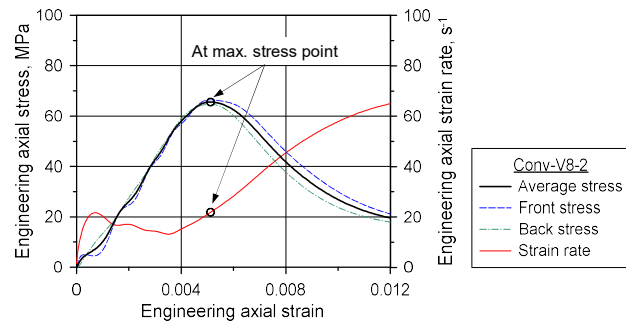


(b)

Figure A.7 Test results of Conv-V8-1; (a) Stress waves; (b) Axial stress–strain curve

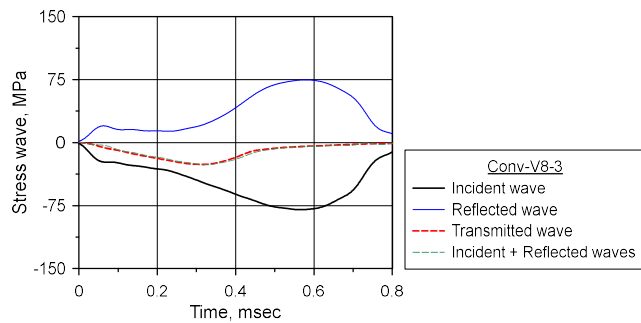


(a)

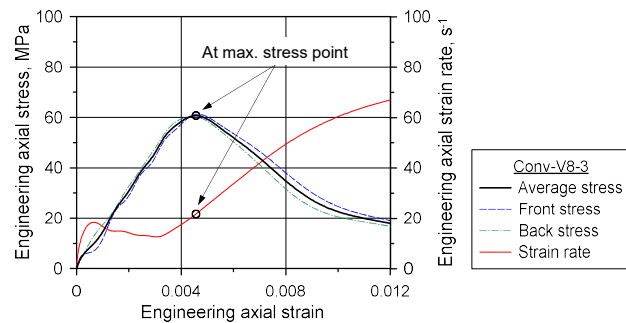


(b)

Figure A.8 Test results of Conv-V8-2; (a) Stress waves; (b) Axial stress–strain curve

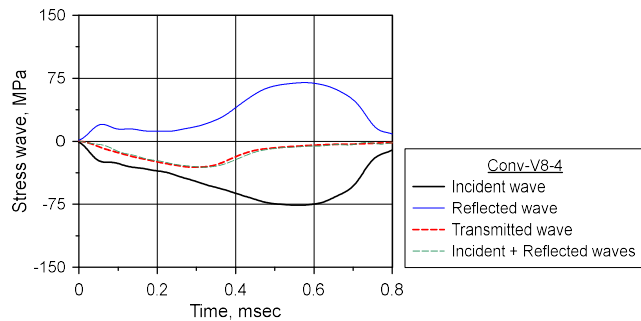


(a)

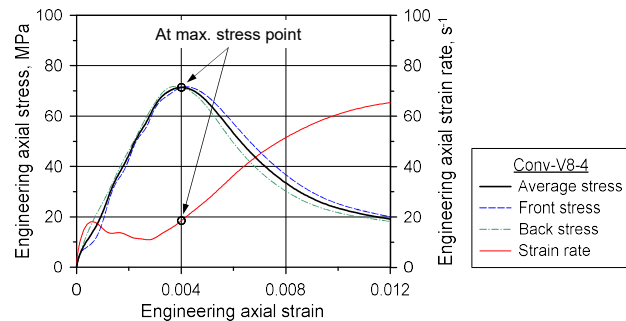


(b)

Figure A.9 Test results of Conv-V8-3; (a) Stress waves; (b) Axial stress–strain curve

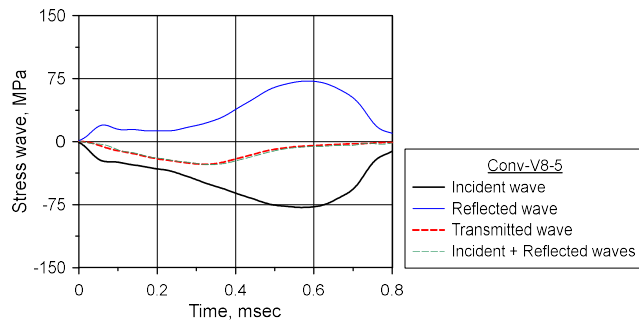


(a)

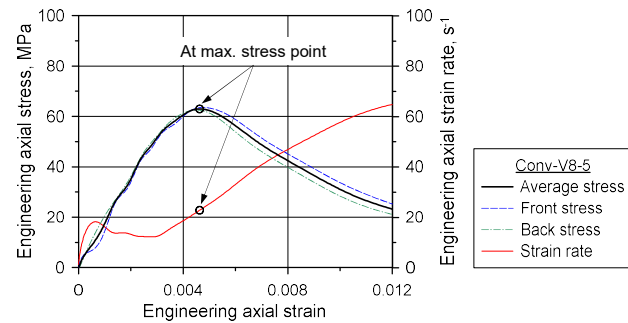


(b)

Figure A.10 Test results of Conv-V8-4; (a) Stress waves; (b) Axial stress–strain curve

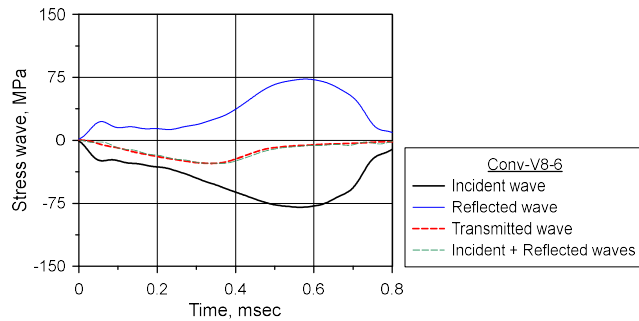


(a)

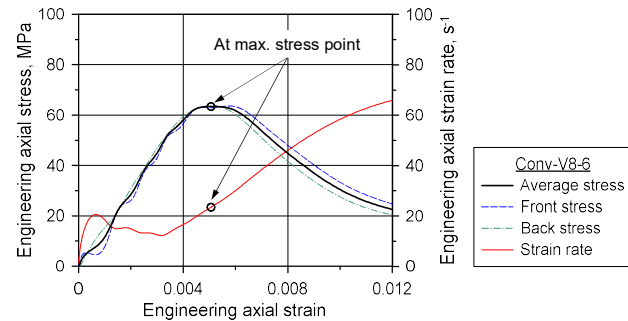


(b)

Figure A.11 Test results of Conv-V8-5; (a) Stress waves; (b) Axial stress–strain curve

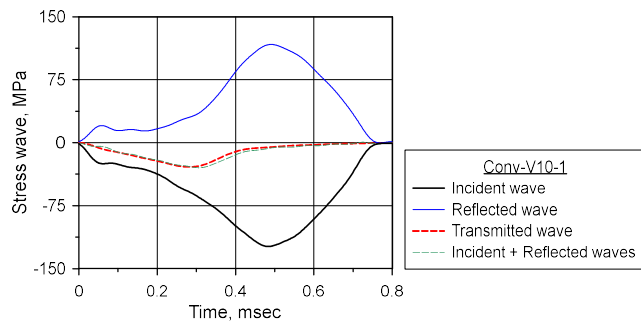


(a)

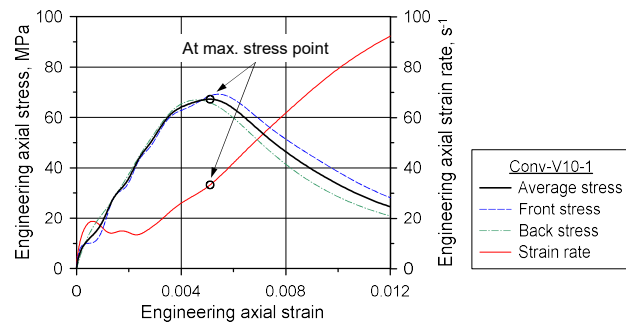


(b)

Figure A.12 Test results of Conv-V8-6; (a) Stress waves; (b) Axial stress–strain curve

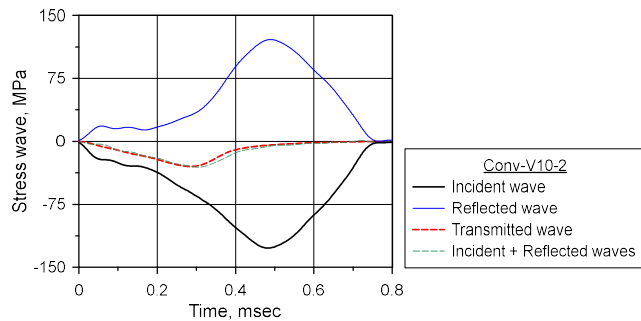


(a)

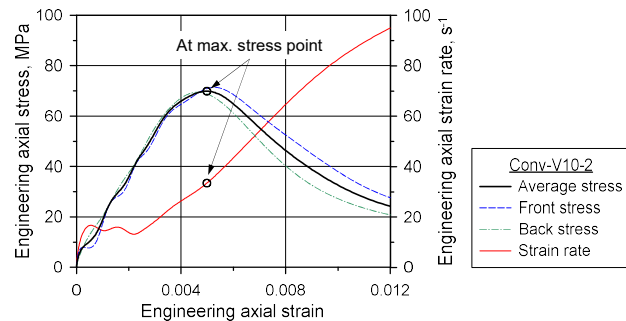


(b)

Figure A.13 Test results of Conv-V10-1; (a) Stress waves; (b) Axial stress–strain curve

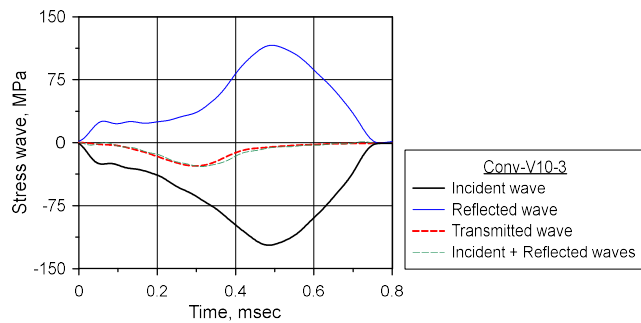


(a)

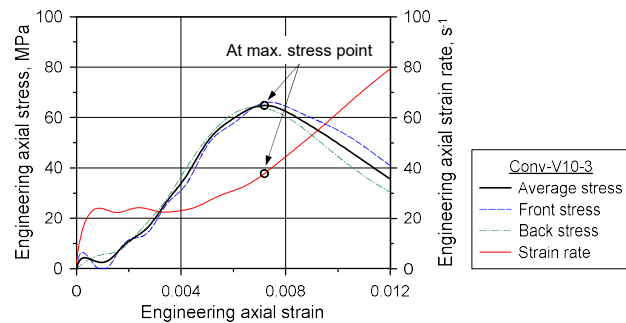


(b)

Figure A.14 Test results of Conv-V10-2; (a) Stress waves; (b) Axial stress–strain curve

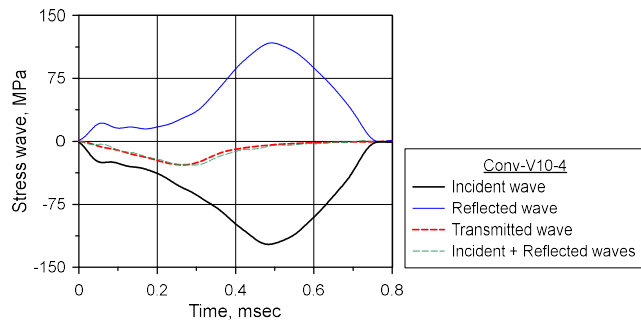


(a)

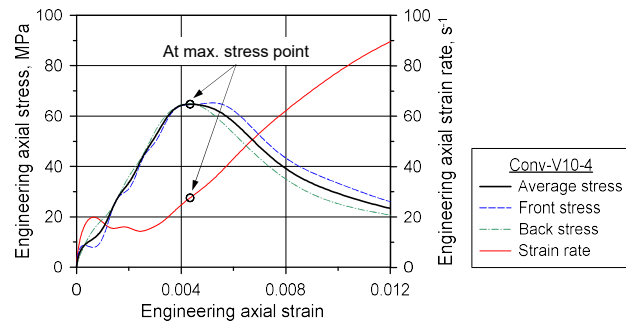


(b)

Figure A.15 Test results of Conv-V10-3; (a) Stress waves; (b) Axial stress–strain curve

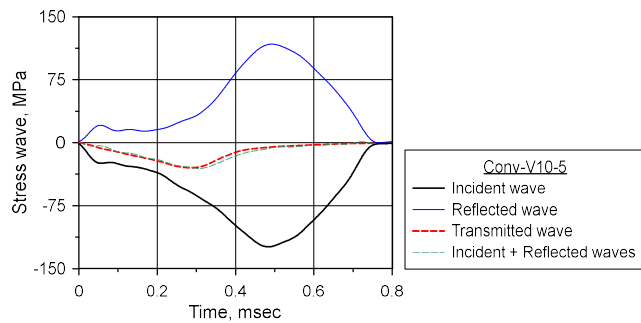


(a)

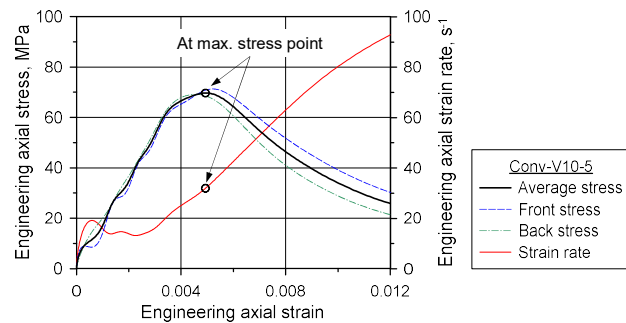


(b)

Figure A.16 Test results of Conv-V10-4; (a) Stress waves; (b) Axial stress–strain curve

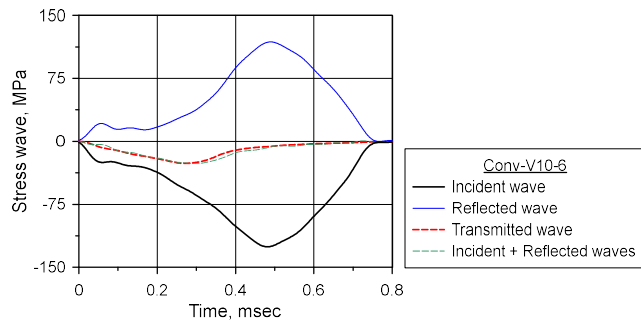


(a)

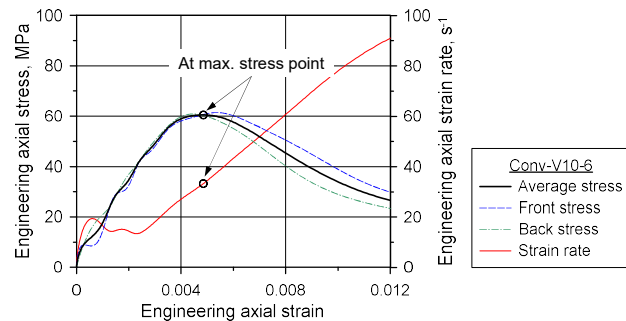


(b)

Figure A.17 Test results of Conv-V10-5; (a) Stress waves; (b) Axial stress–strain curve

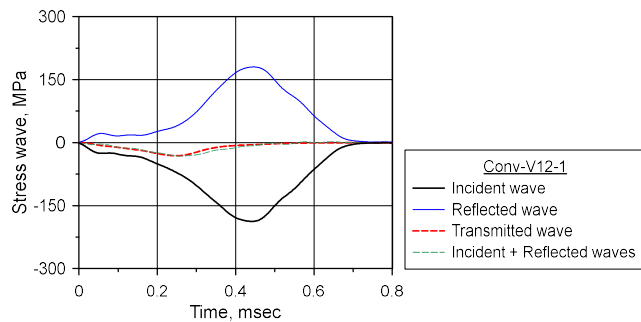


(a)

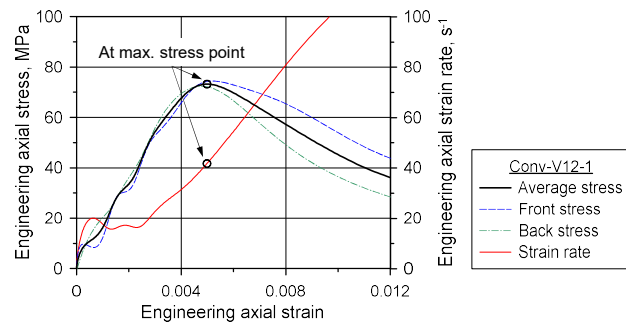


(b)

Figure A.18 Test results of Conv-V10-6; (a) Stress waves; (b) Axial stress–strain curve

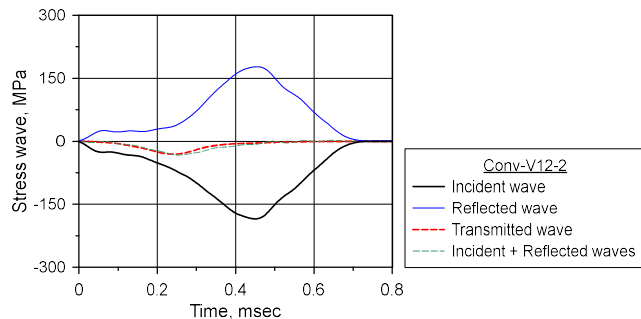


(a)

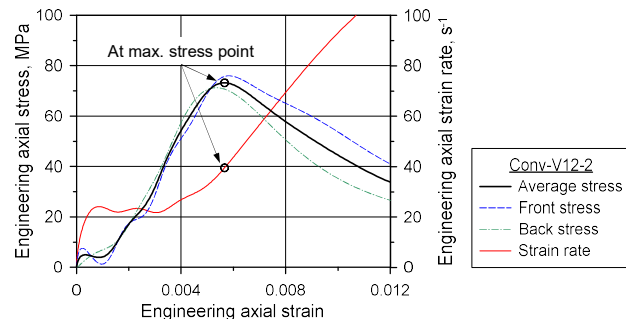


(b)

Figure A.19 Test results of Conv-V12-1; (a) Stress waves; (b) Axial stress–strain curve

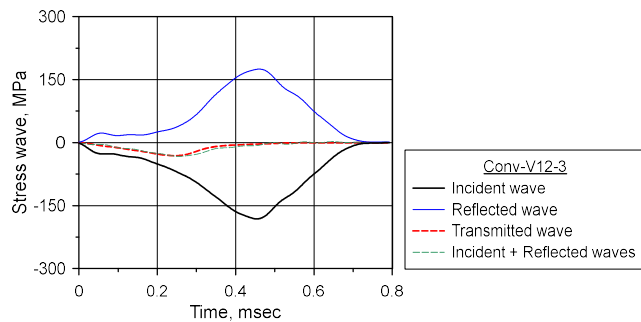


(a)

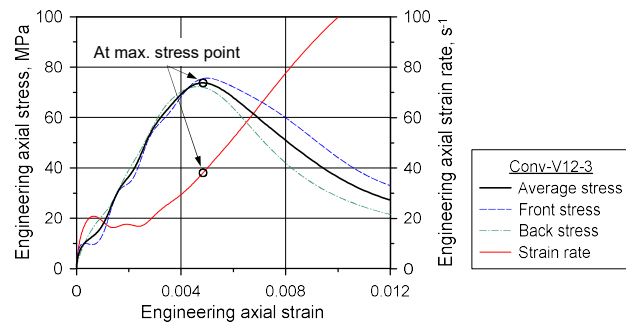


(b)

Figure A.20 Test results of Conv-V12-2; (a) Stress waves; (b) Axial stress–strain curve

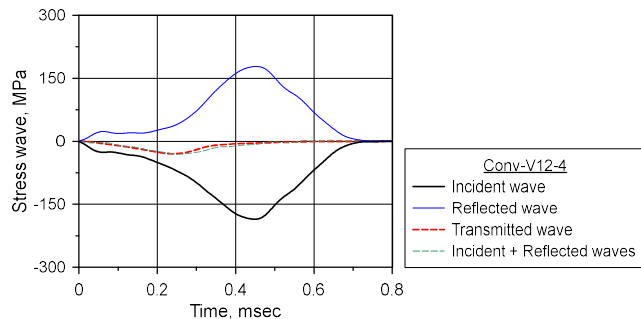


(a)

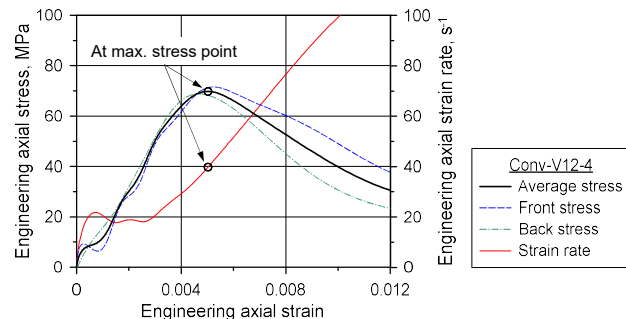


(b)

Figure A.21 Test results of Conv-V12-3; (a) Stress waves; (b) Axial stress–strain curve

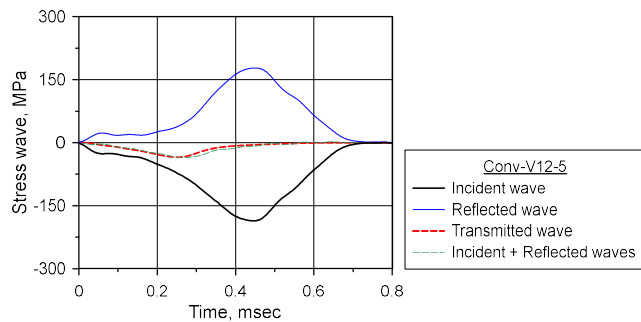


(a)

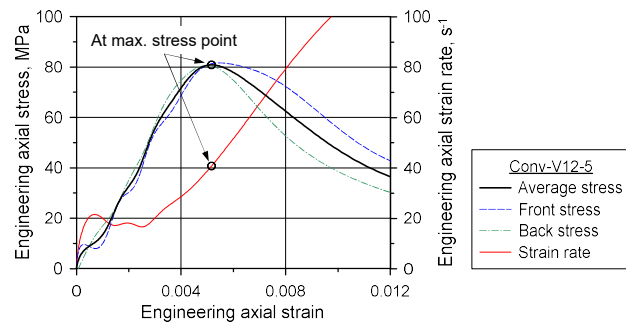


(b)

Figure A.22 Test results of Conv-V12-4; (a) Stress waves; (b) Axial stress–strain curve

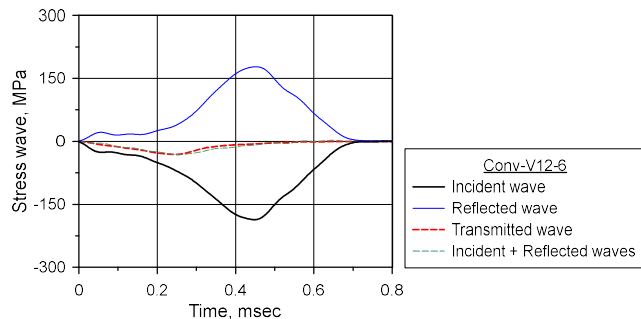


(a)

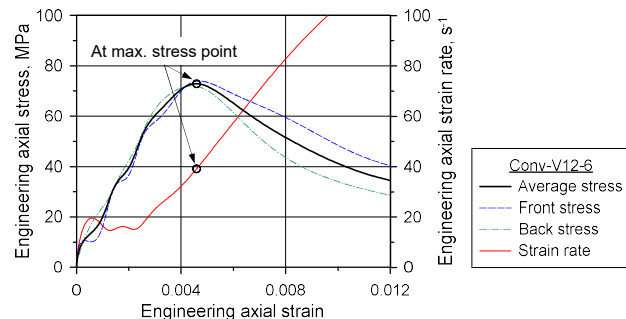


(b)

Figure A.23 Test results of Conv-V12-5; (a) Stress waves; (b) Axial stress–strain curve

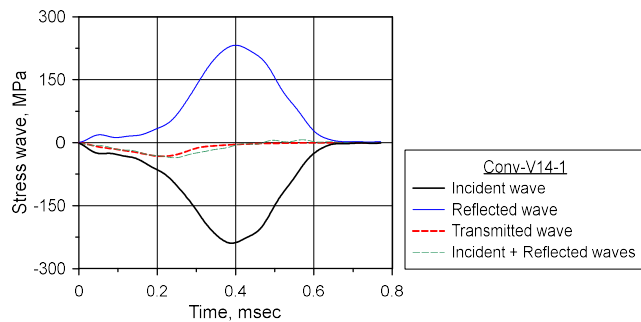


(a)

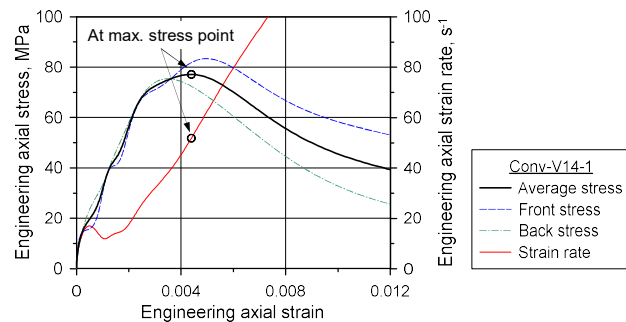


(b)

Figure A.24 Test results of Conv-V12-6; (a) Stress waves; (b) Axial stress–strain curve

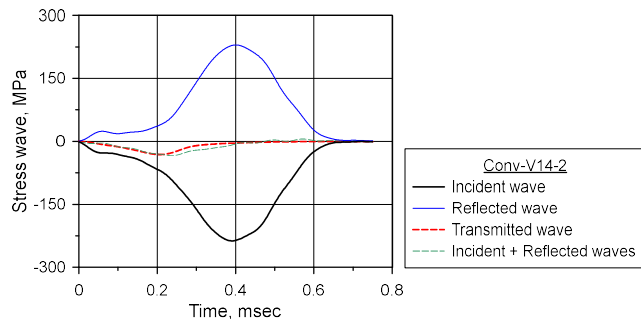


(a)

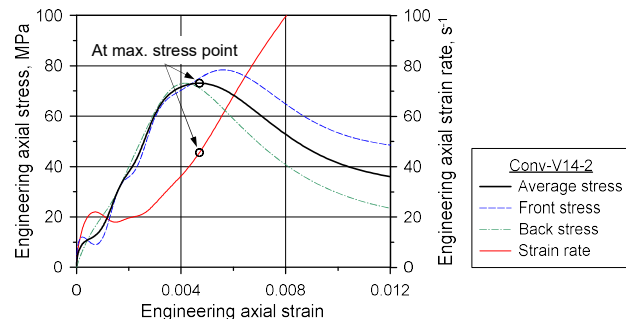


(b)

Figure A.25 Test results of Conv-V14-1; (a) Stress waves; (b) Axial stress–strain curve

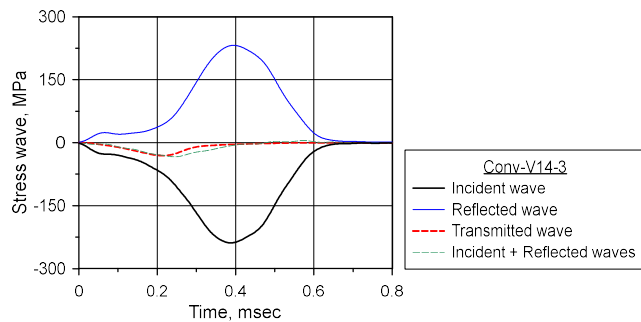


(a)

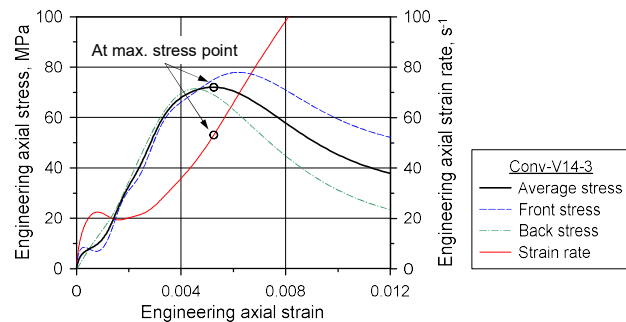


(b)

Figure A.26 Test results of Conv-V14-2; (a) Stress waves; (b) Axial stress–strain curve

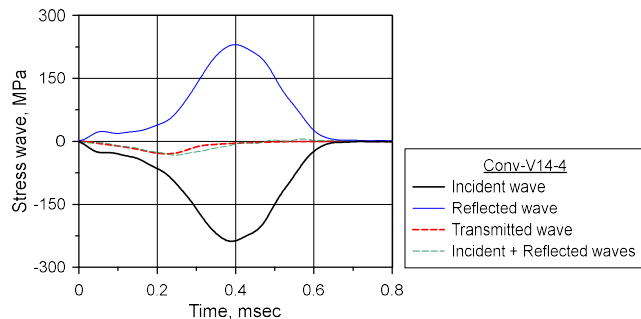


(a)

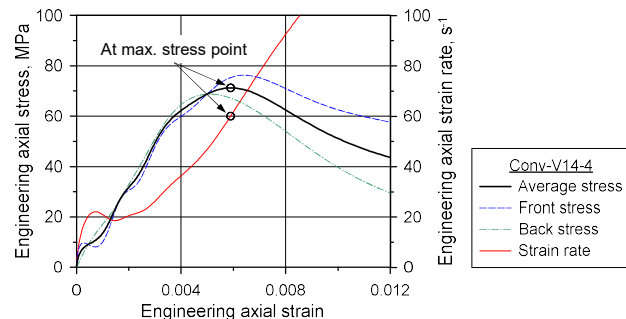


(b)

Figure A.27 Test results of Conv-V14-3; (a) Stress waves; (b) Axial stress–strain curve

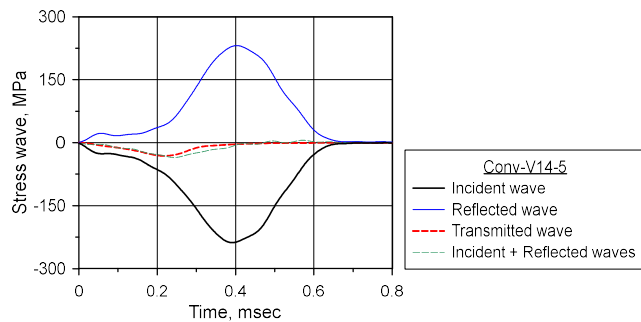


(a)

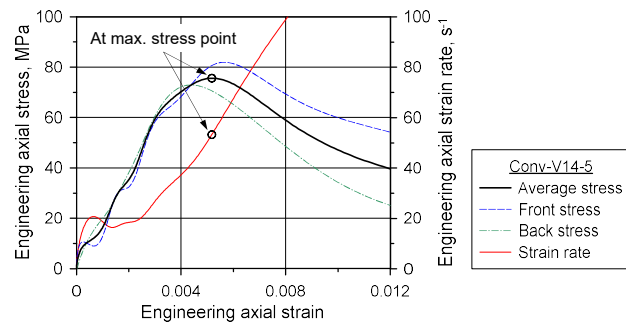


(b)

Figure A.28 Test results of Conv-V14-4; (a) Stress waves; (b) Axial stress–strain curve

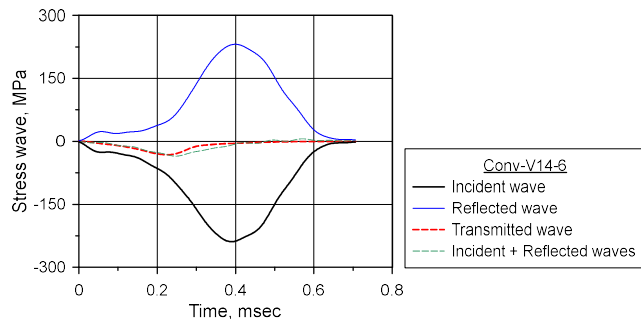


(a)

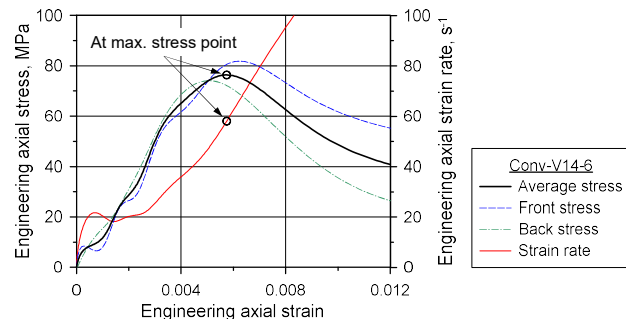


(b)

Figure A.29 Test results of Conv-V14-5; (a) Stress waves; (b) Axial stress–strain curve



(a)



(b)

Figure A.30 Test results of Conv-V14-6; (a) Stress waves; (b) Axial stress–strain curve

Appendix B

Experimental Results of Confined SHPB Tests

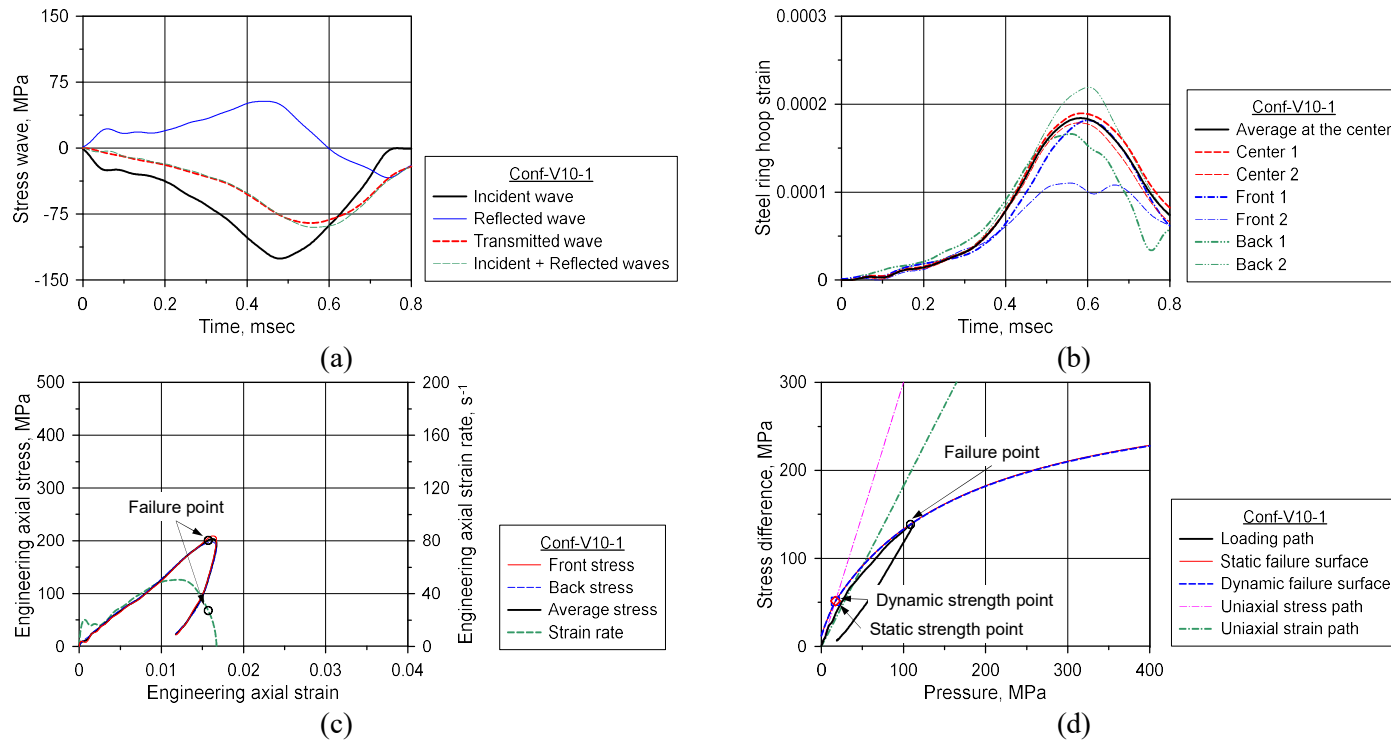


Figure B.1 Test results of Conf-V10-1; (a) Stress waves; (b) Circumferential strain of steel ring;
(c) Axial stress–strain curve; (d) Loading path and dynamic failure surface

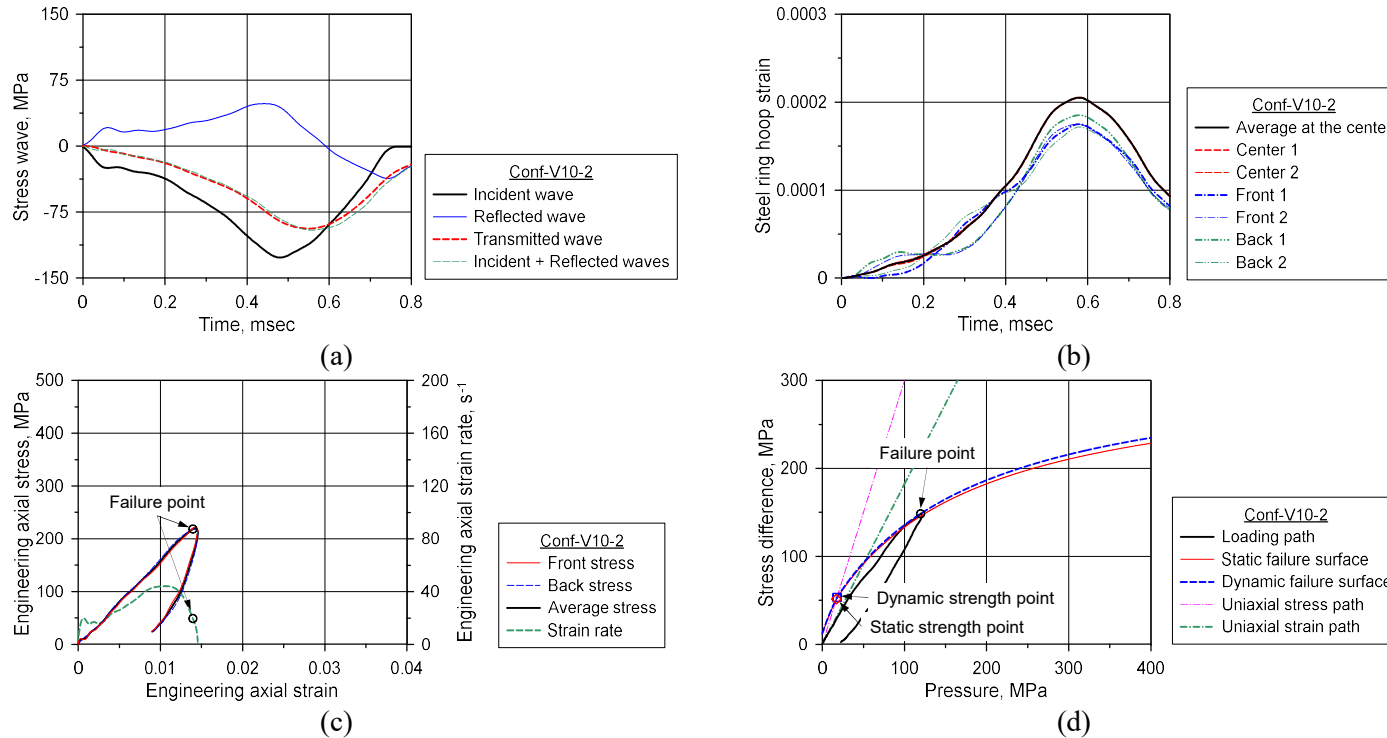


Figure B.2 Test results of Conf-V10-2; (a) Stress waves; (b) Circumferential strain of steel ring;
(c) Axial stress–strain curve; (d) Loading path and dynamic failure surface

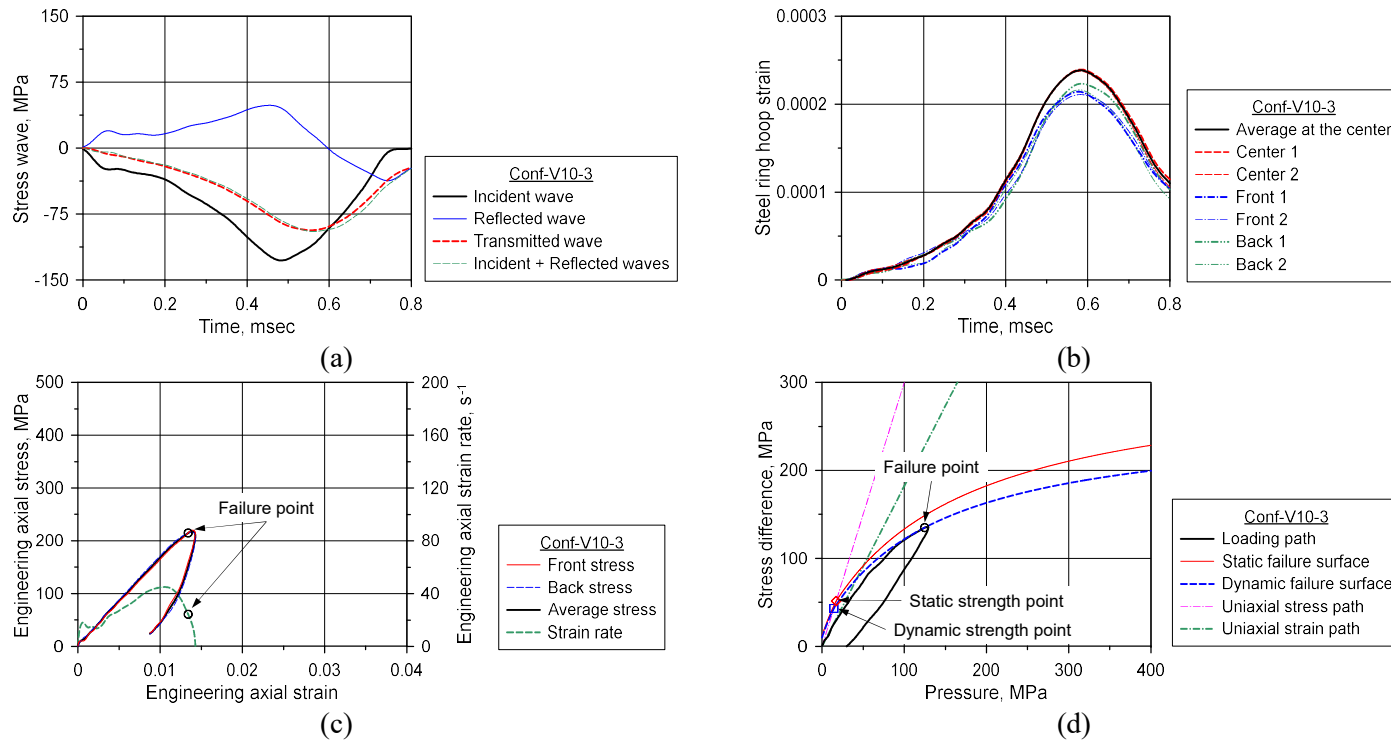


Figure B.3 Test results of Conf-V10-3; (a) Stress waves; (b) Circumferential strain of steel ring;
(c) Axial stress–strain curve; (d) Loading path and dynamic failure surface

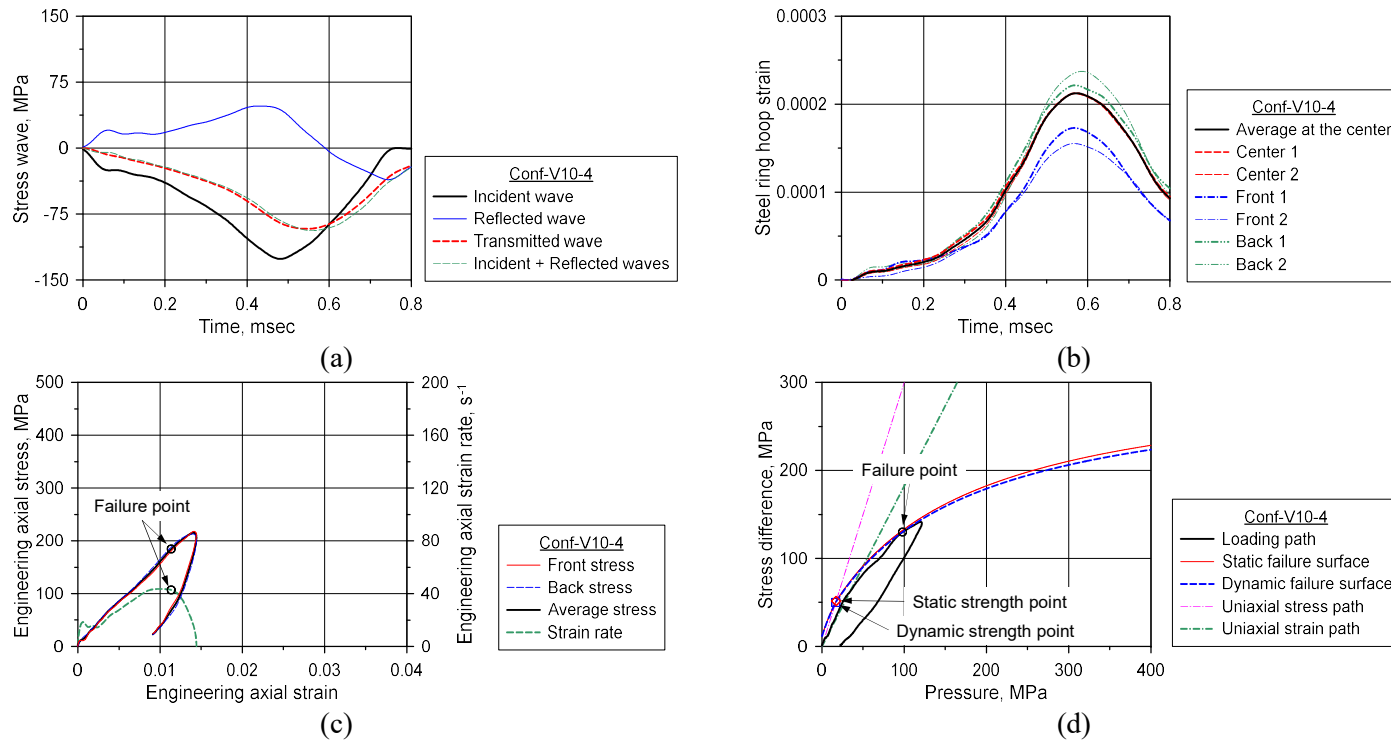


Figure B.4 Test results of Conf-V10-4; (a) Stress waves; (b) Circumferential strain of steel ring;
(c) Axial stress–strain curve; (d) Loading path and dynamic failure surface

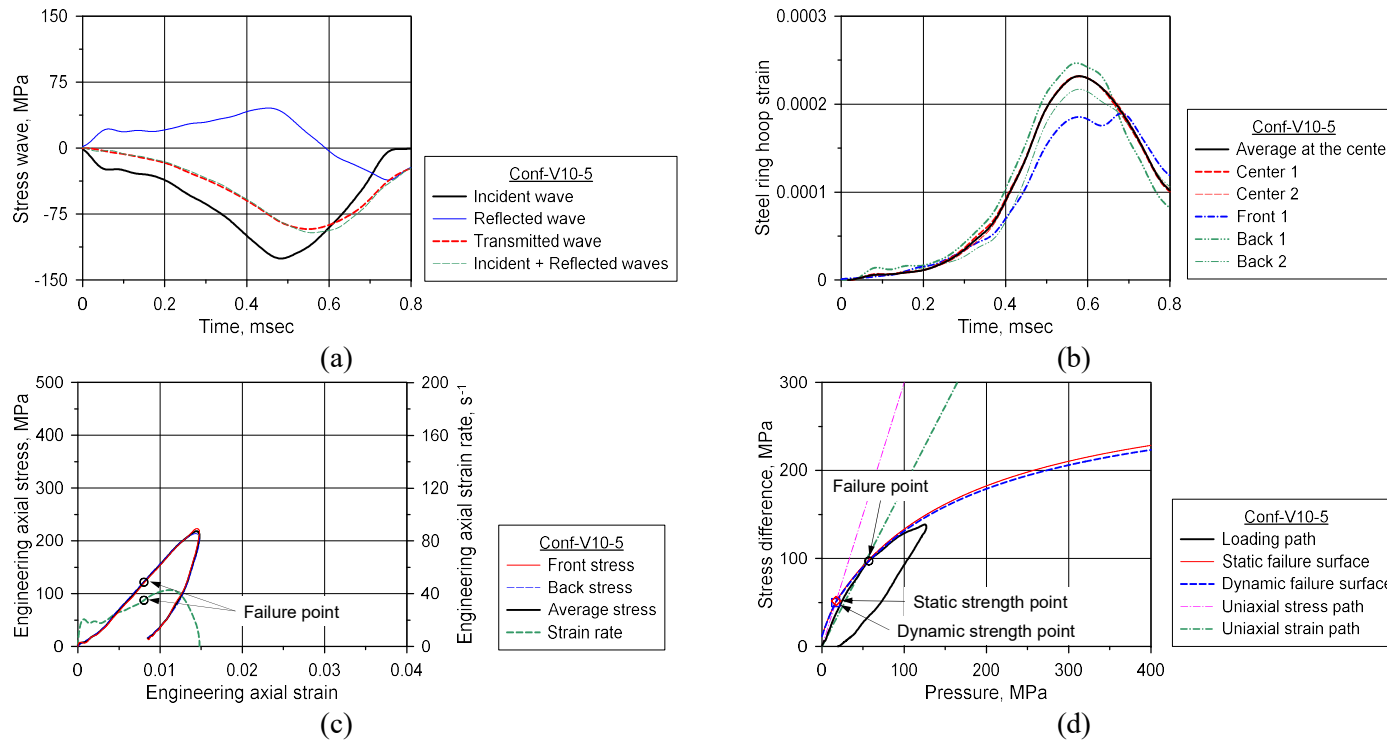


Figure B.5 Test results of Conf-V10-5; (a) Stress waves; (b) Circumferential strain of steel ring;
(c) Axial stress–strain curve; (d) Loading path and dynamic failure surface

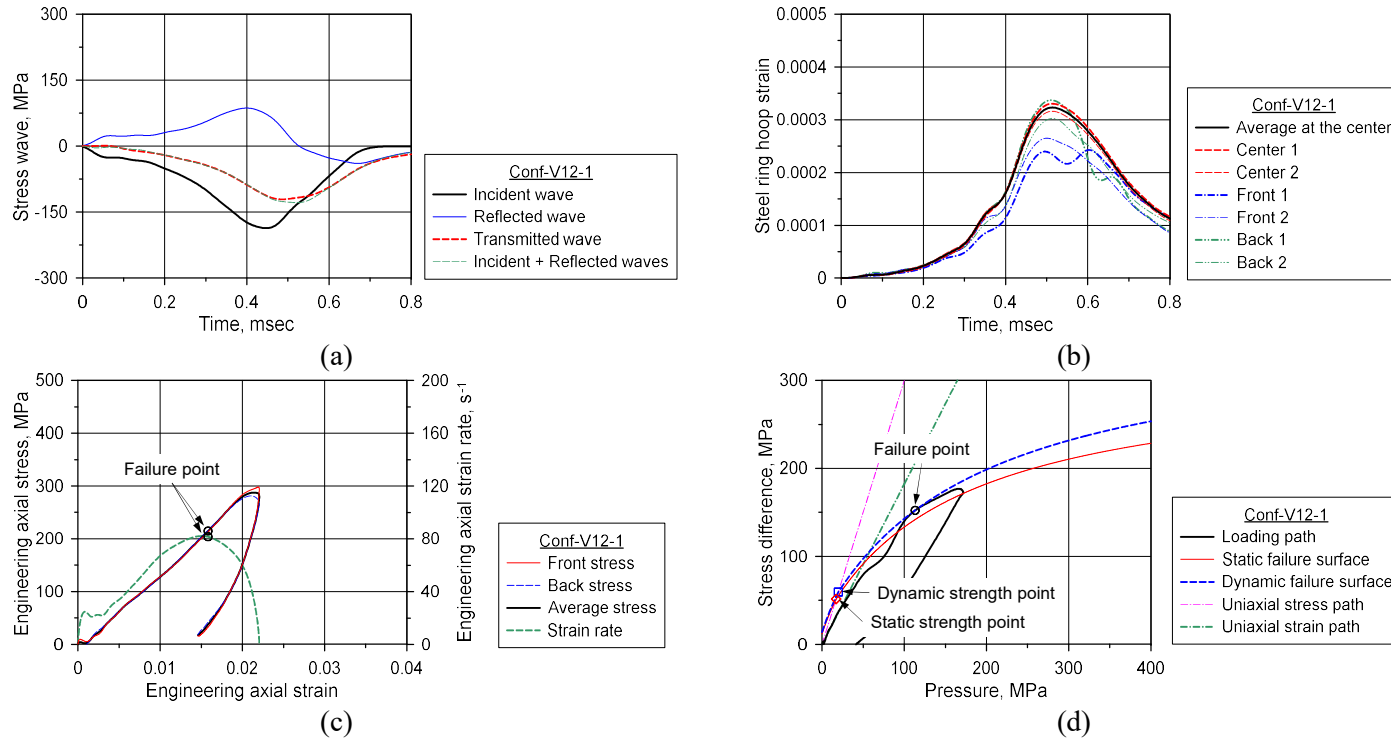


Figure B.6 Test results of Conf-V12-1; (a) Stress waves; (b) Circumferential strain of steel ring;
(c) Axial stress–strain curve; (d) Loading path and dynamic failure surface

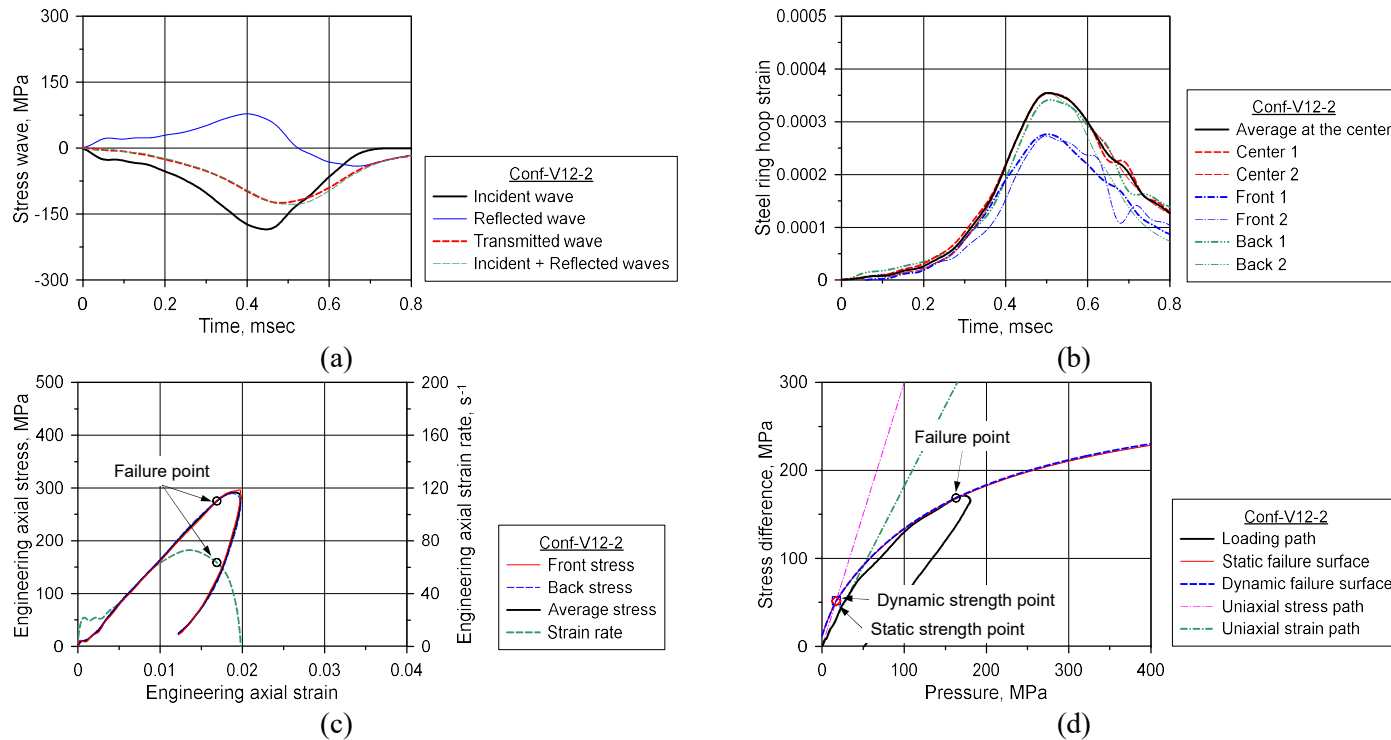


Figure B.7 Test results of Conf-V12-2; (a) Stress waves; (b) Circumferential strain of steel ring;
(c) Axial stress–strain curve; (d) Loading path and dynamic failure surface

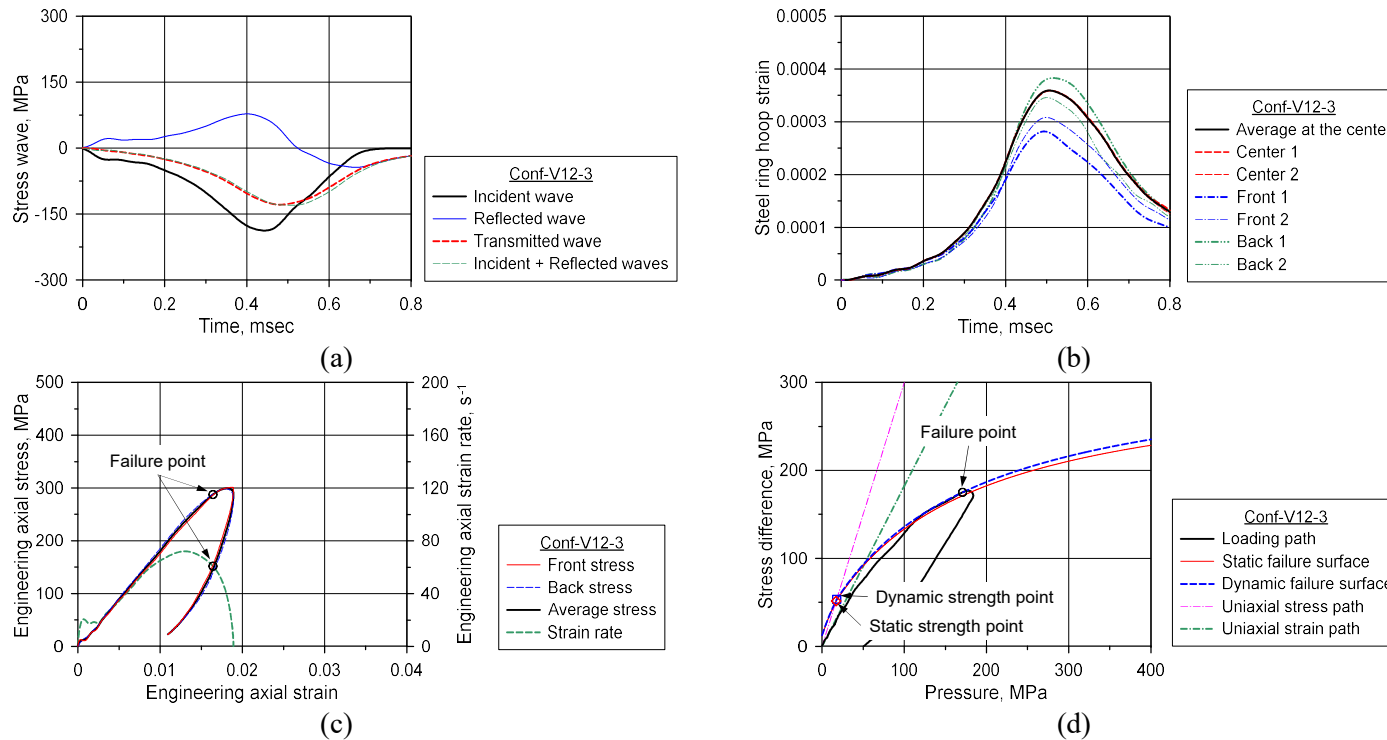


Figure B.8 Test results of Conf-V12-3; (a) Stress waves; (b) Circumferential strain of steel ring;
(c) Axial stress–strain curve; (d) Loading path and dynamic failure surface

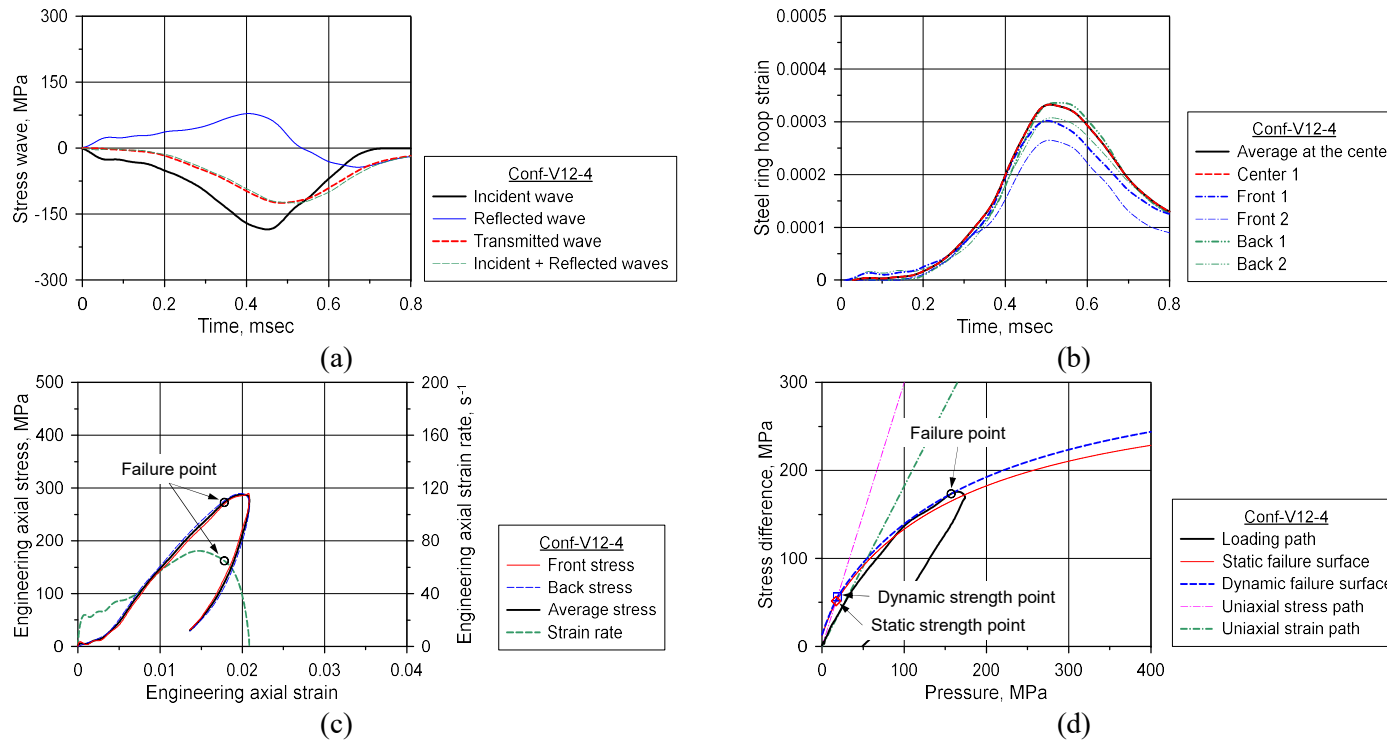


Figure B.9 Test results of Conf-V12-4; (a) Stress waves; (b) Circumferential strain of steel ring;
(c) Axial stress–strain curve; (d) Loading path and dynamic failure surface

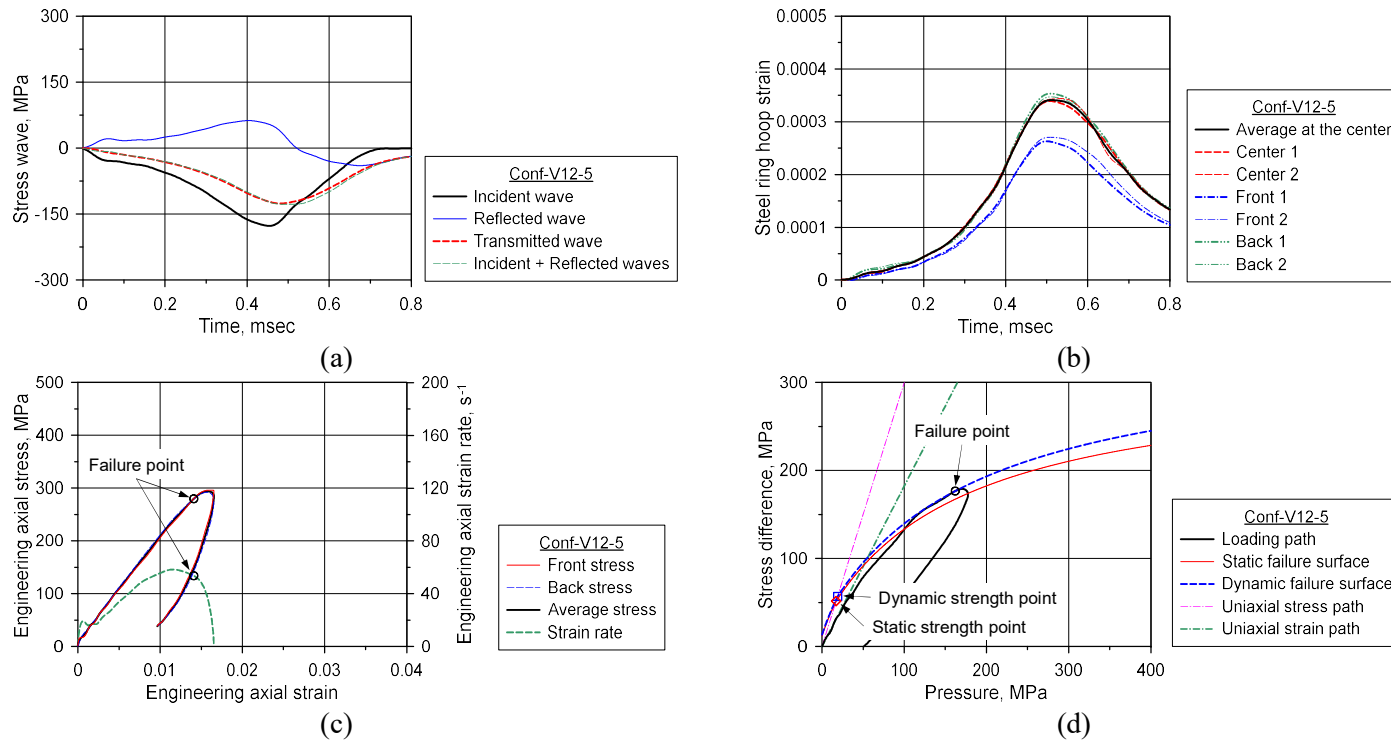


Figure B.10 Test results of Conf-V12-5; (a) Stress waves; (b) Circumferential strain of steel ring; (c) Axial stress–strain curve; (d) Loading path and dynamic failure surface

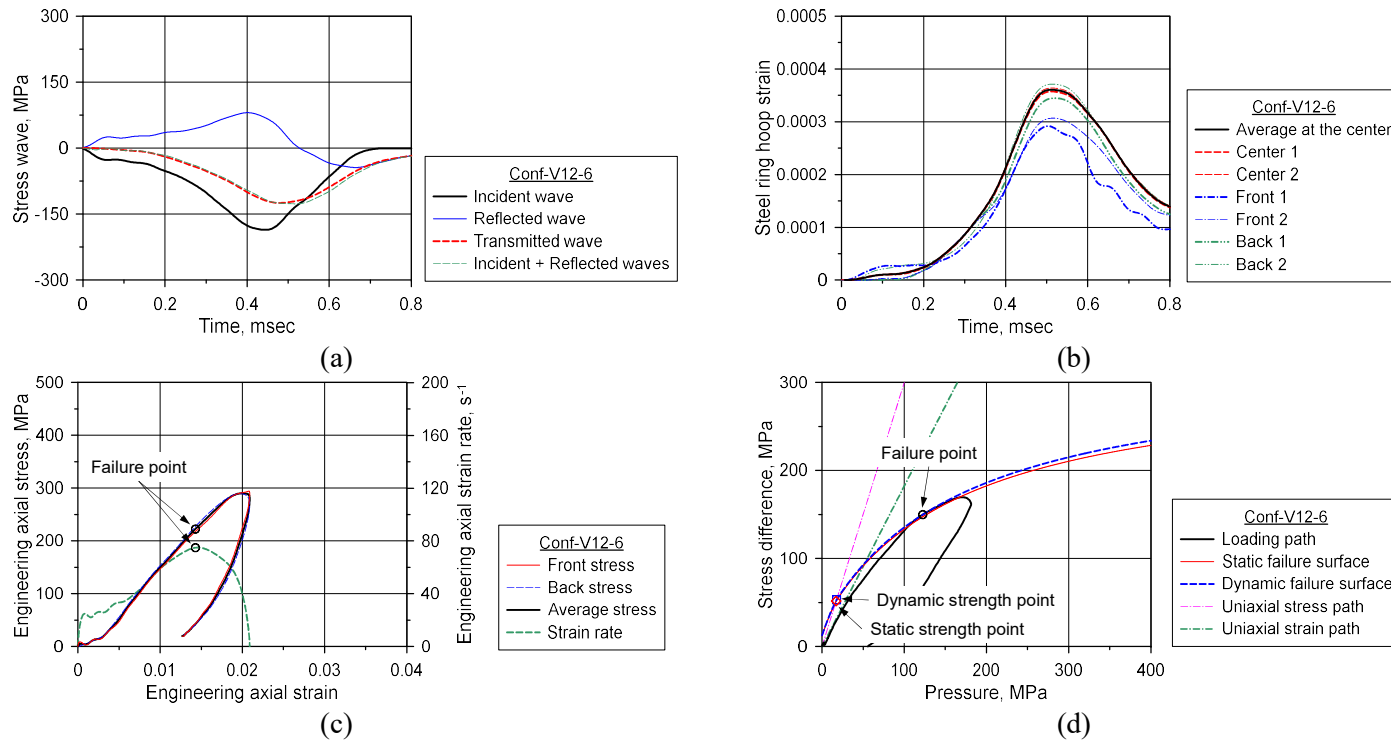


Figure B.11 Test results of Conf-V12-6; (a) Stress waves; (b) Circumferential strain of steel ring; (c) Axial stress–strain curve; (d) Loading path and dynamic failure surface

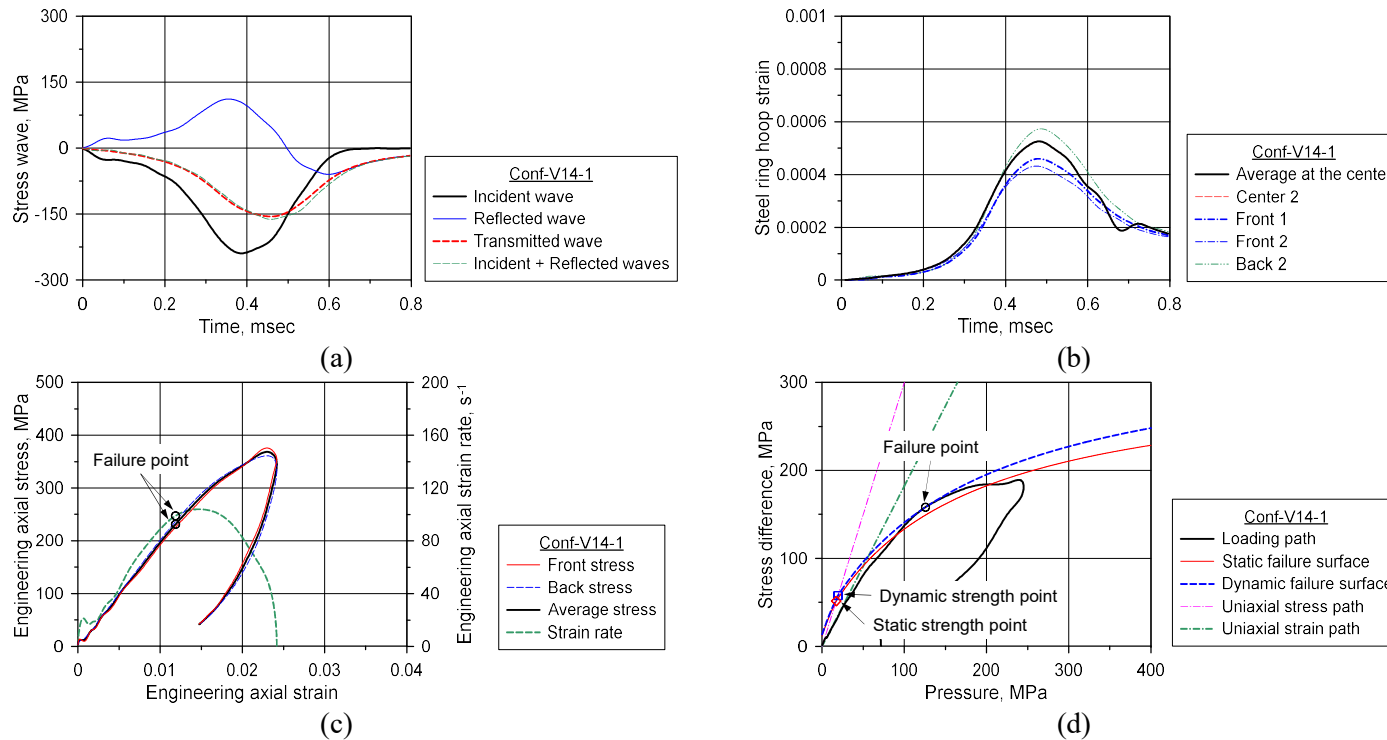


Figure B.12 Test results of Conf-V14-1; (a) Stress waves; (b) Circumferential strain of steel ring;
(c) Axial stress–strain curve; (d) Loading path and dynamic failure surface

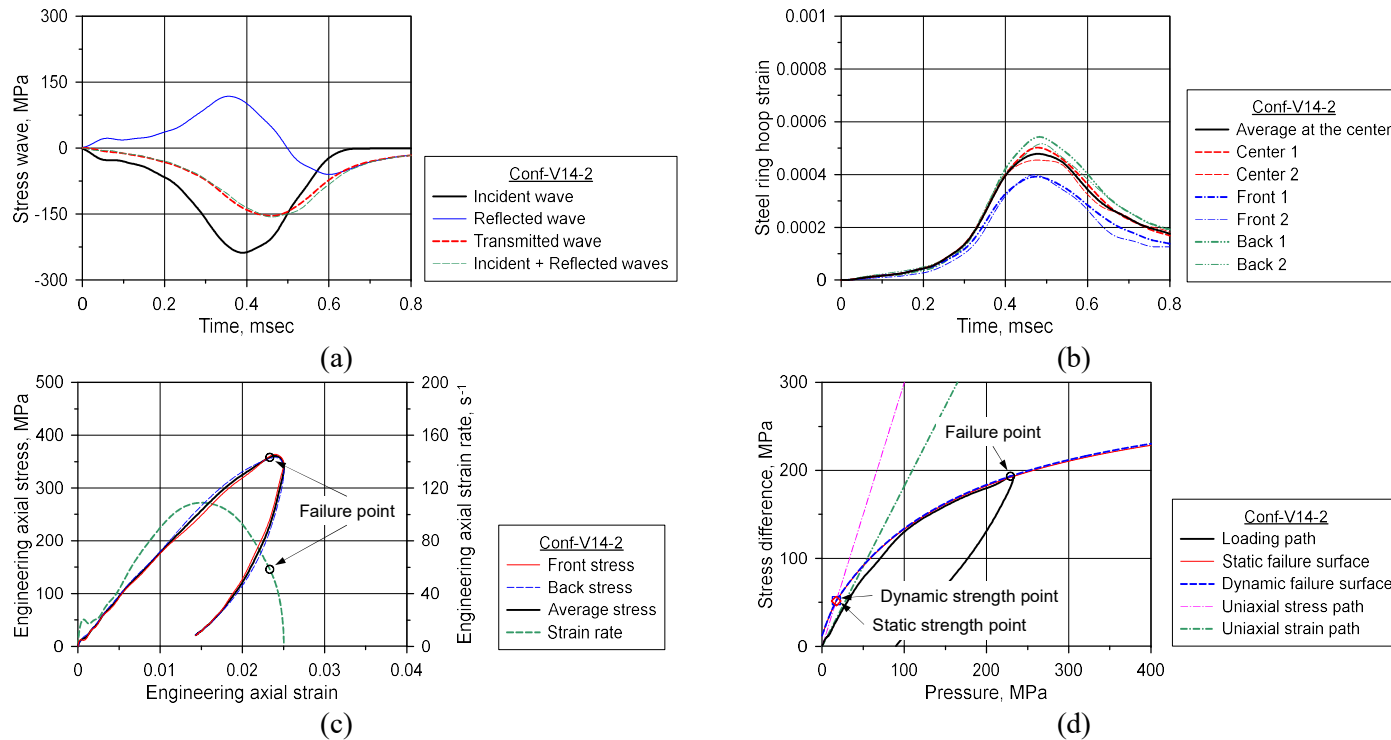


Figure B.13 Test results of Conf-V14-2; (a) Stress waves; (b) Circumferential strain of steel ring; (c) Axial stress–strain curve; (d) Loading path and dynamic failure surface

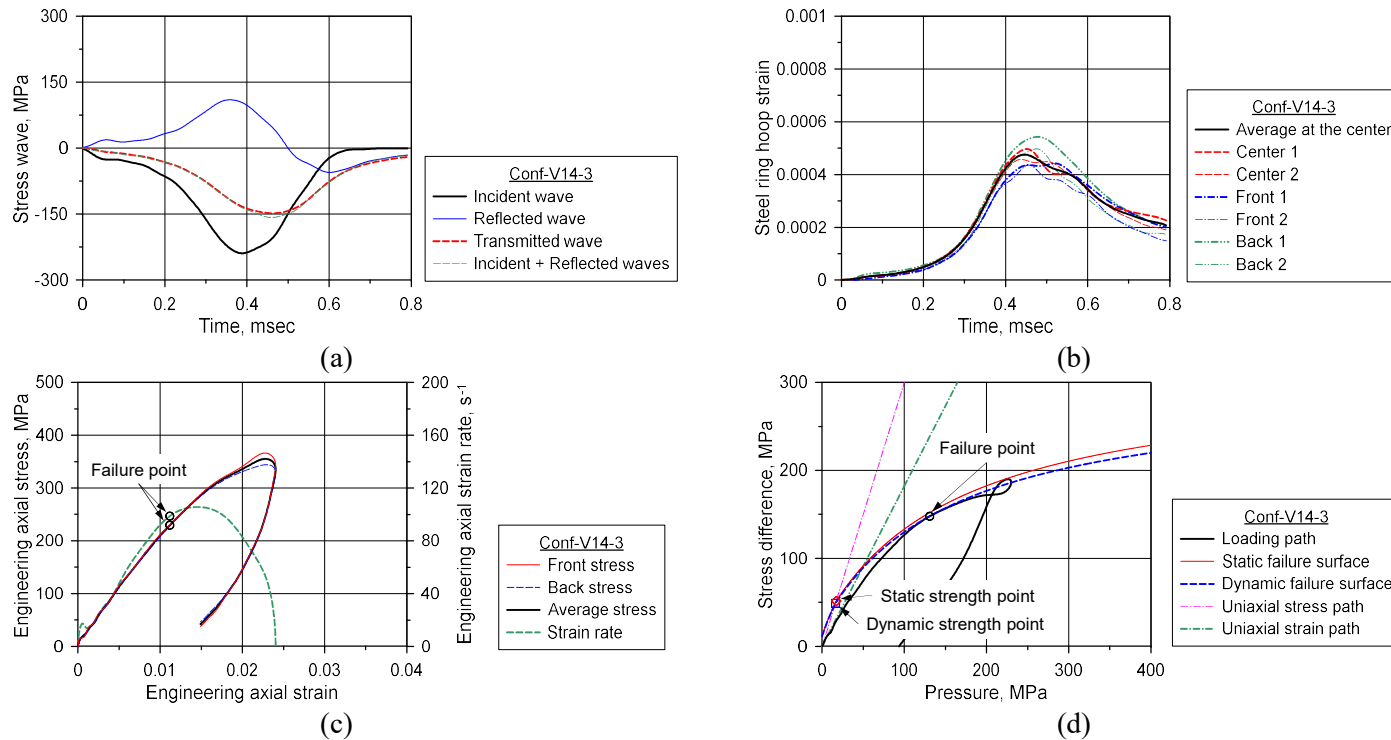


Figure B.14 Test results of Conf-V14-3; (a) Stress waves; (b) Circumferential strain of steel ring; (c) Axial stress–strain curve; (d) Loading path and dynamic failure surface

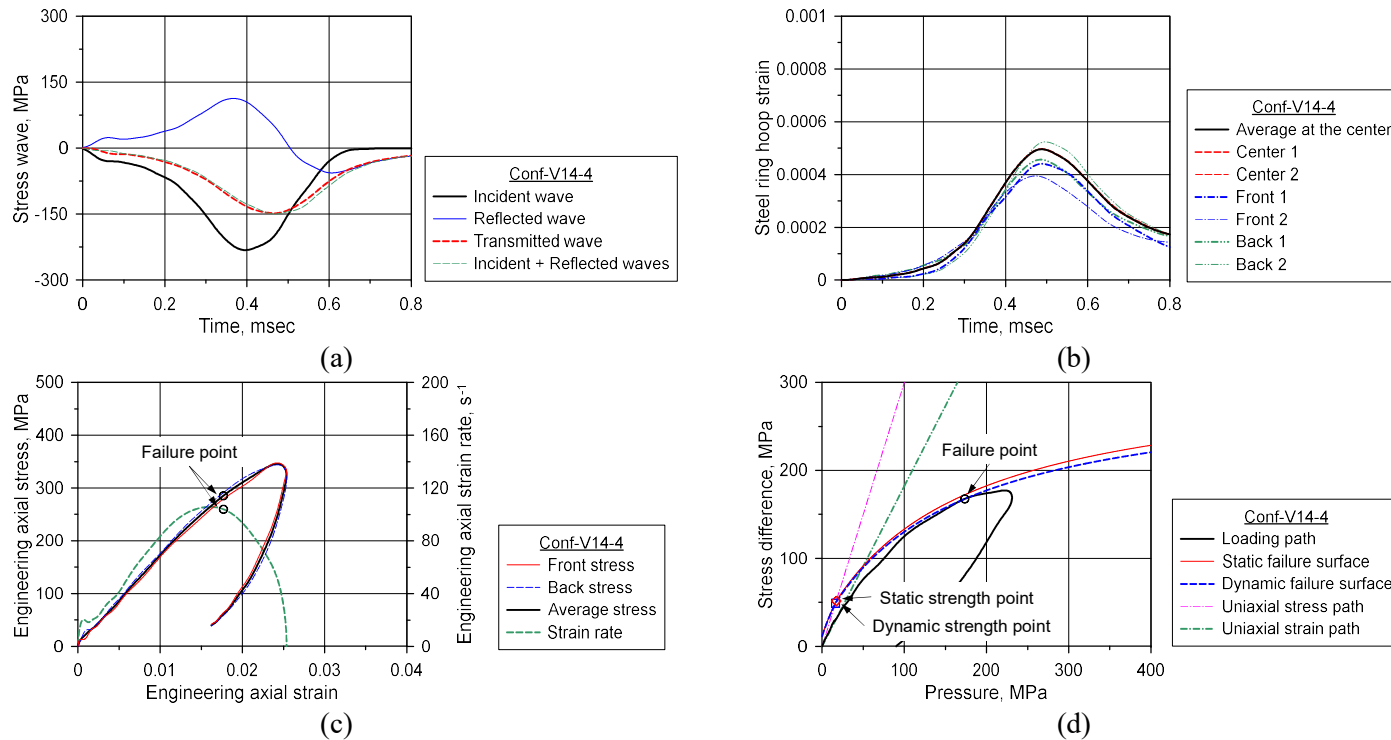


Figure B.15 Test results of Conf-V14-4; (a) Stress waves; (b) Circumferential strain of steel ring; (c) Axial stress–strain curve; (d) Loading path and dynamic failure surface

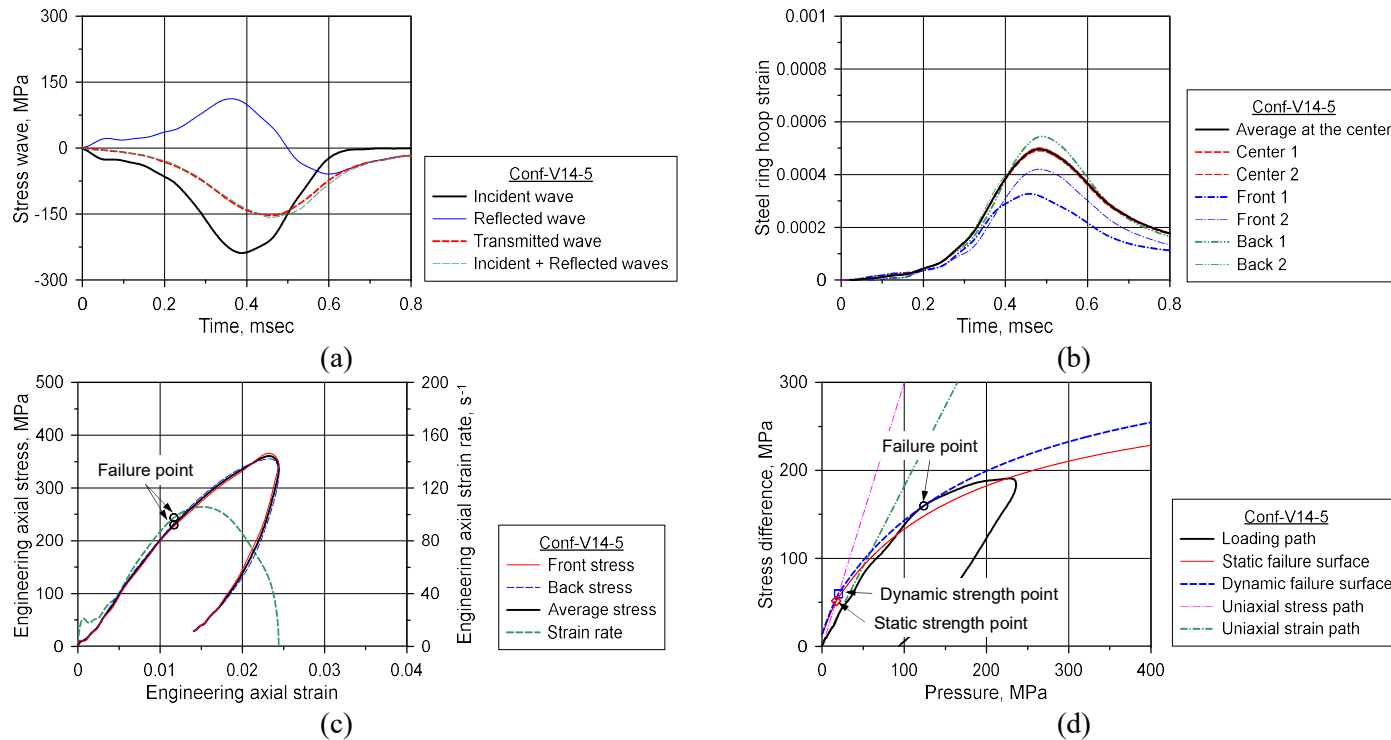


Figure B.16 Test results of Conf-V14-5; (a) Stress waves; (b) Circumferential strain of steel ring;
(c) Axial stress–strain curve; (d) Loading path and dynamic failure surface

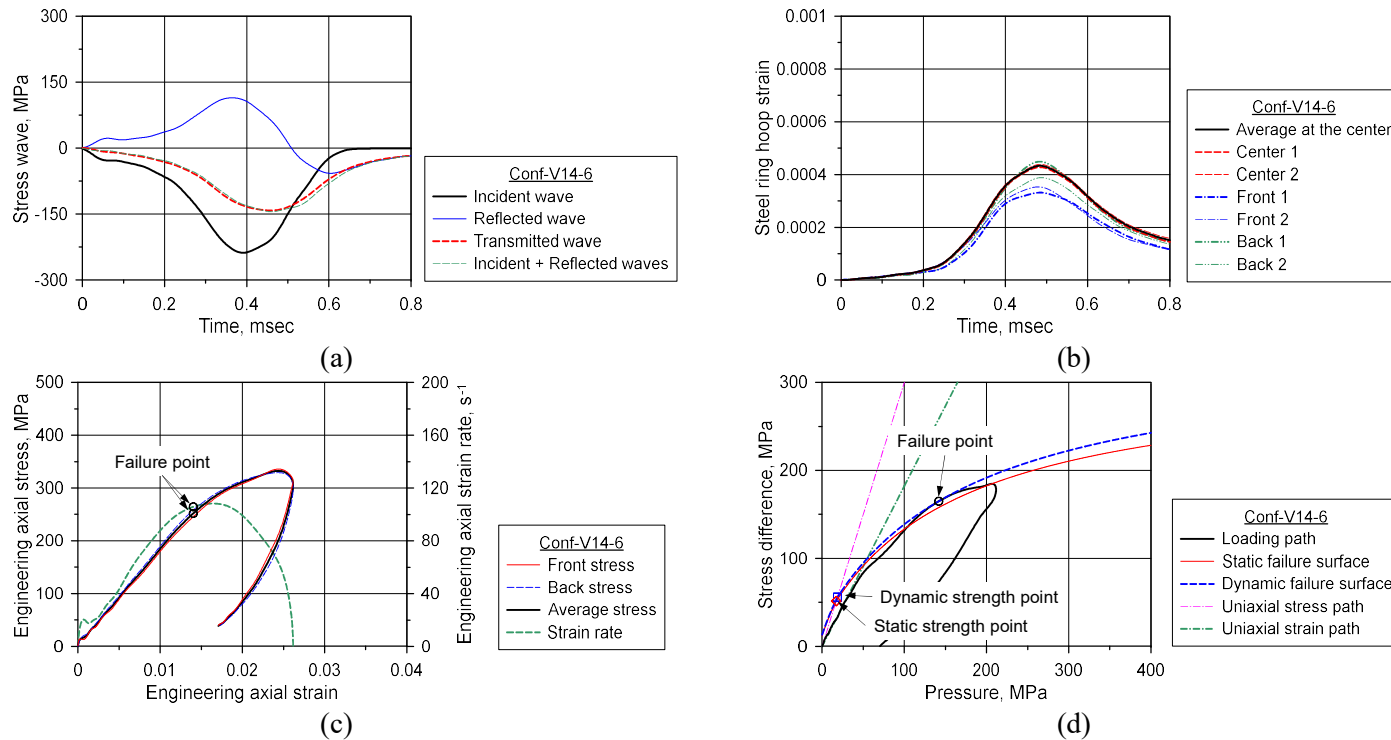


Figure B.17 Test results of Conf-V14-6; (a) Stress waves; (b) Circumferential strain of steel ring;
(c) Axial stress–strain curve; (d) Loading path and dynamic failure surface

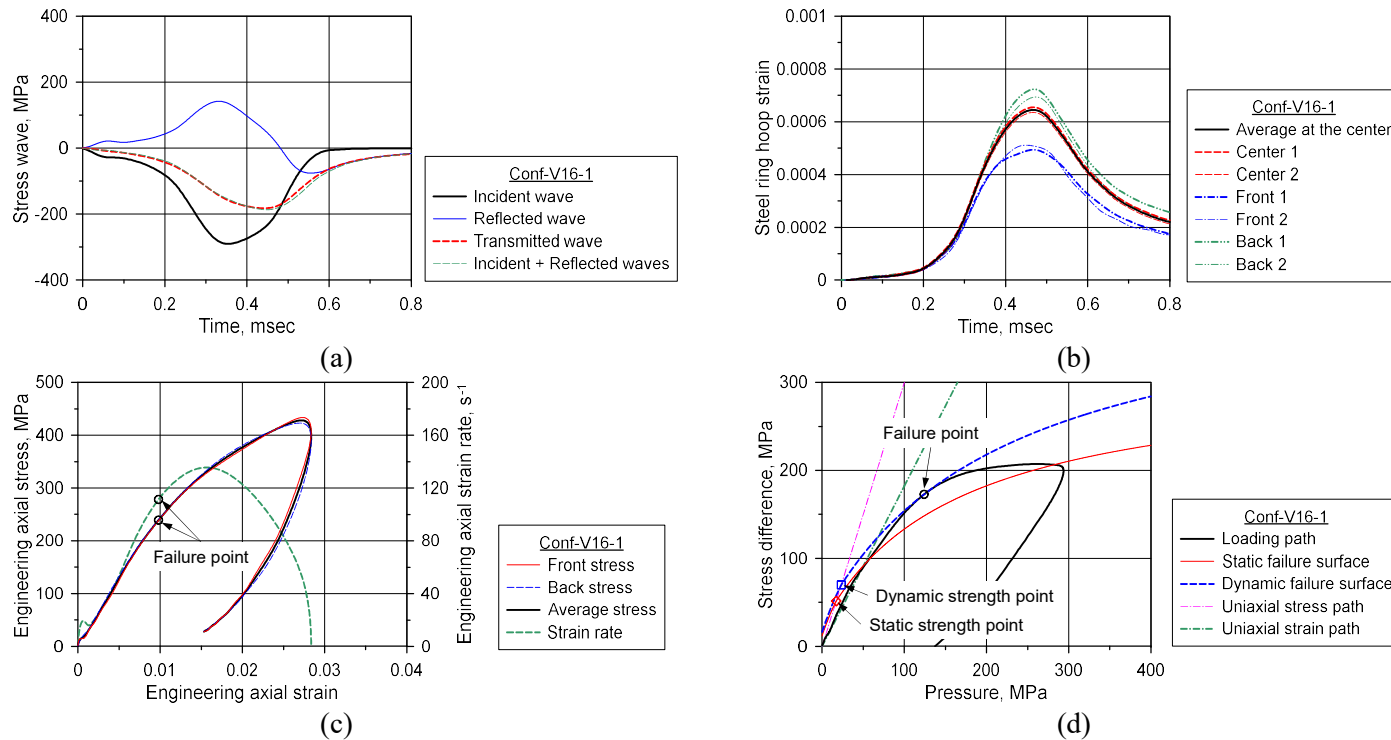


Figure B.18 Test results of Conf-V16-1; (a) Stress waves; (b) Circumferential strain of steel ring;
(c) Axial stress–strain curve; (d) Loading path and dynamic failure surface

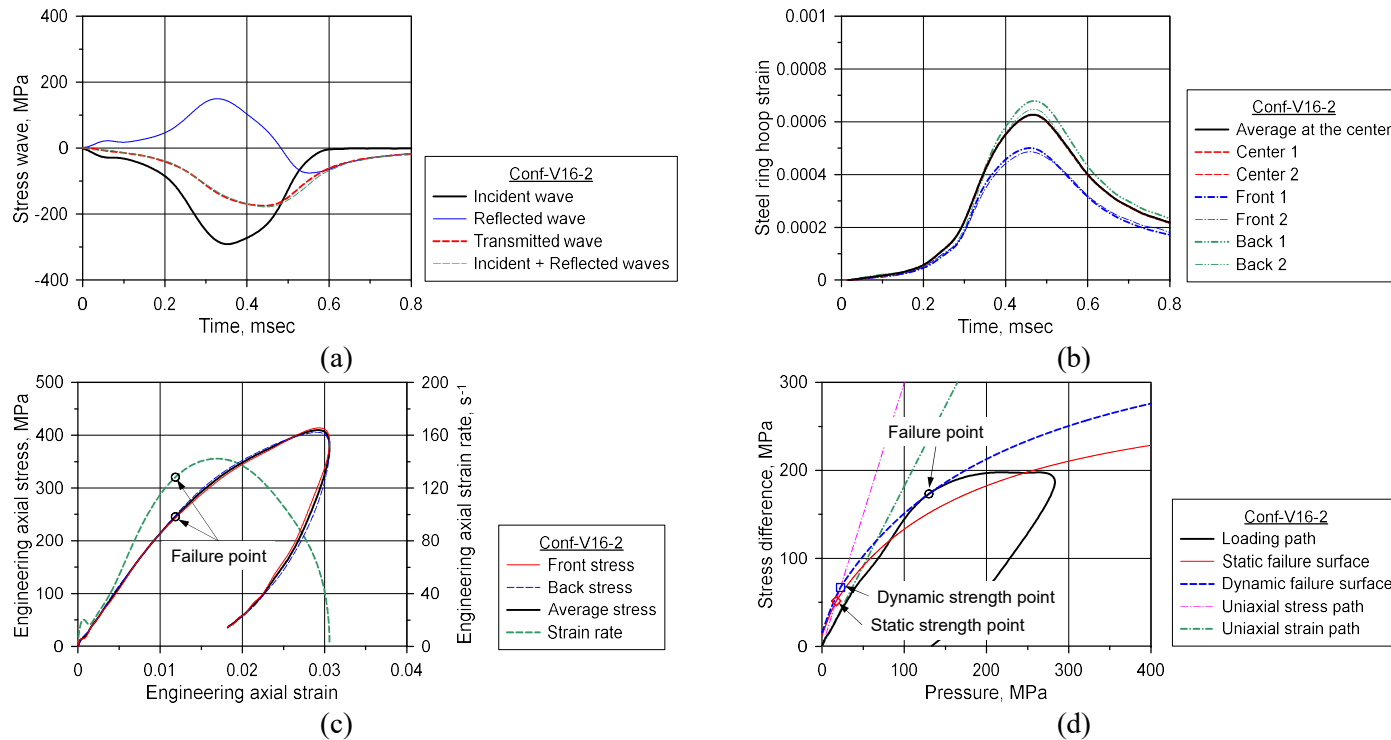


Figure B.19 Test results of Conf-V16-2; (a) Stress waves; (b) Circumferential strain of steel ring;
(c) Axial stress–strain curve; (d) Loading path and dynamic failure surface

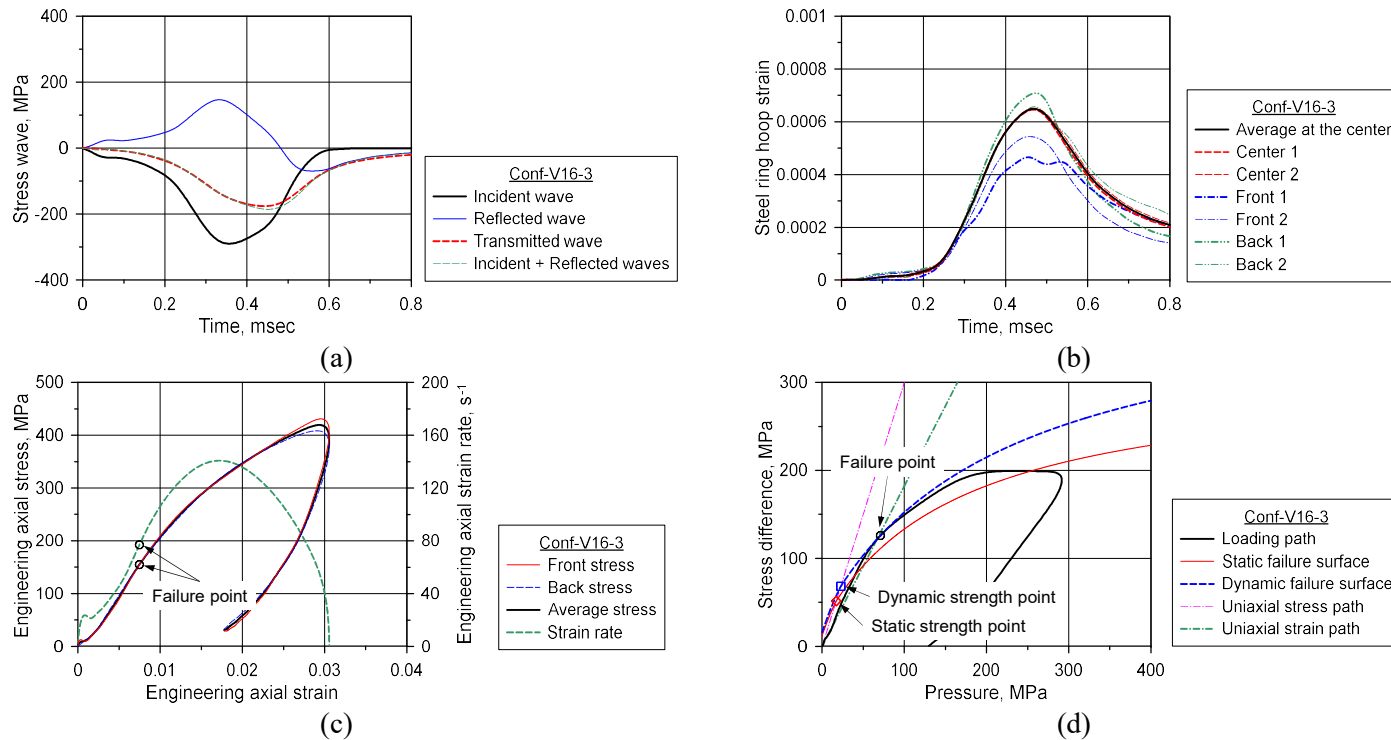


Figure B.20 Test results of Conf-V16-3; (a) Stress waves; (b) Circumferential strain of steel ring; (c) Axial stress–strain curve; (d) Loading path and dynamic failure surface

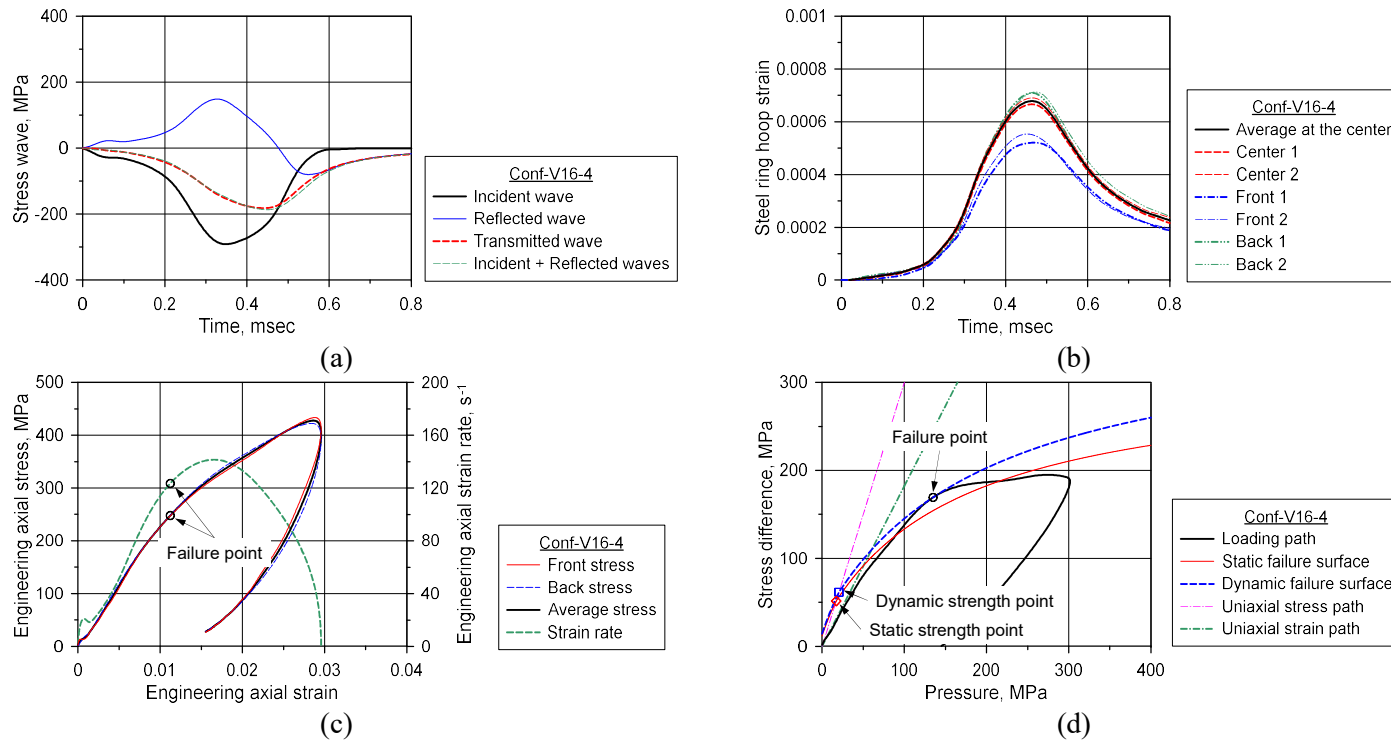


Figure B.21 Test results of Conf-V16-4; (a) Stress waves; (b) Circumferential strain of steel ring;
(c) Axial stress–strain curve; (d) Loading path and dynamic failure surface

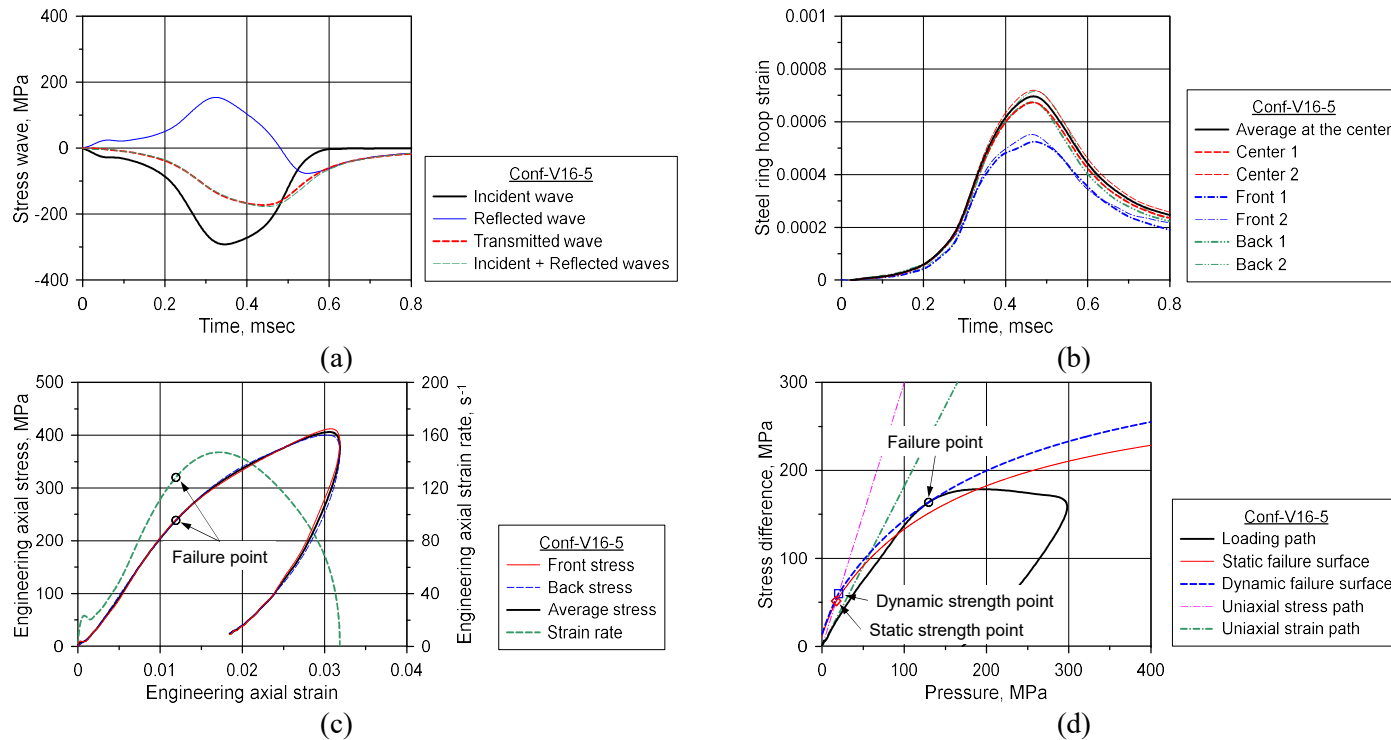


Figure B.22 Test results of Conf-V16-5; (a) Stress waves; (b) Circumferential strain of steel ring;
(c) Axial stress–strain curve; (d) Loading path and dynamic failure surface

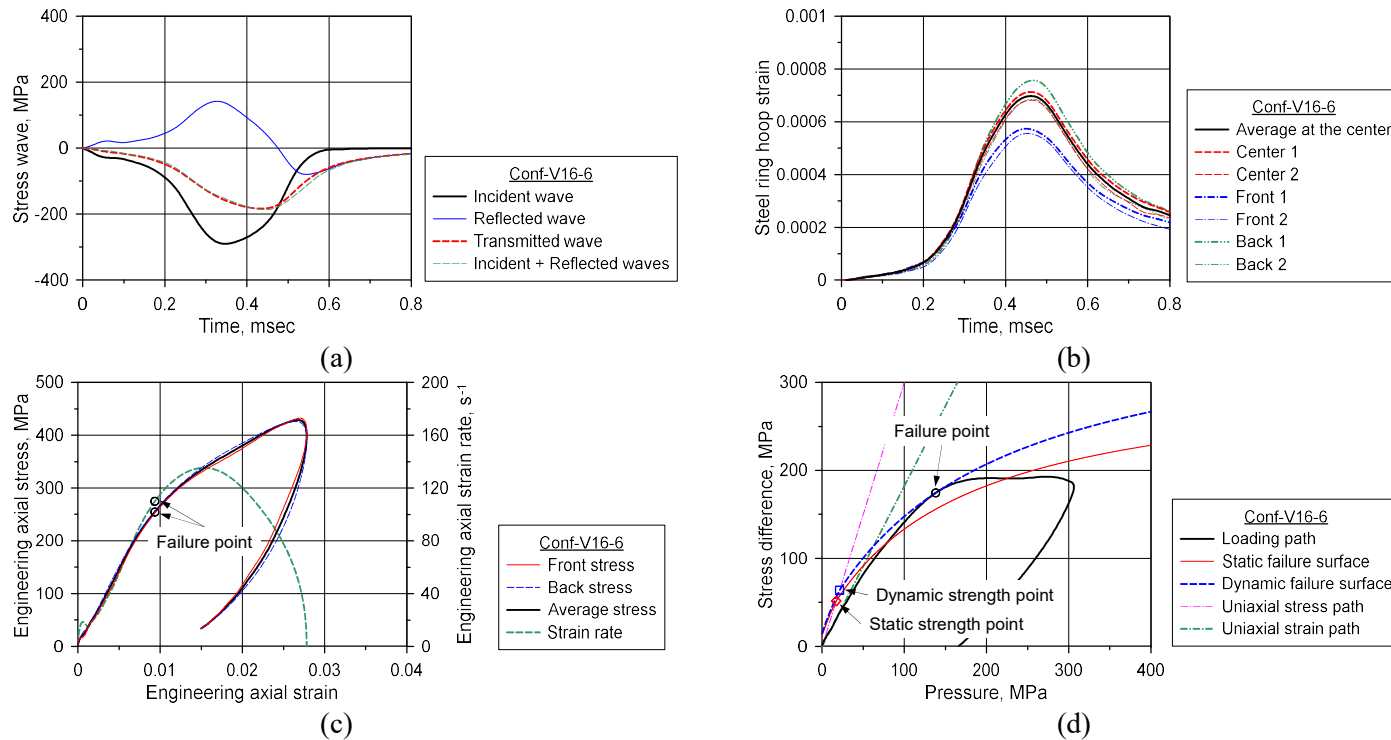


Figure B.23 Test results of Conf-V16-6; (a) Stress waves; (b) Circumferential strain of steel ring;
(c) Axial stress–strain curve; (d) Loading path and dynamic failure surface

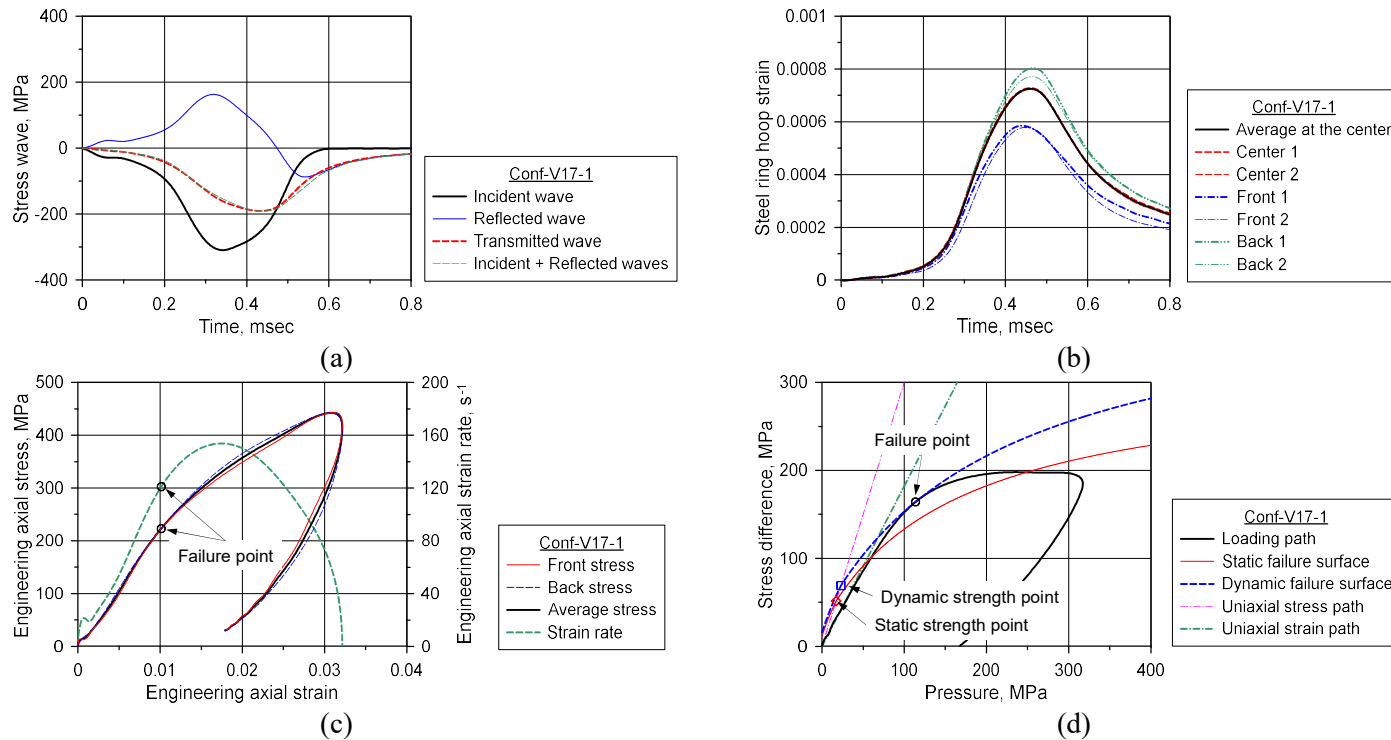


Figure B.24 Test results of Conf-V17-1; (a) Stress waves; (b) Circumferential strain of steel ring;
(c) Axial stress–strain curve; (d) Loading path and dynamic failure surface

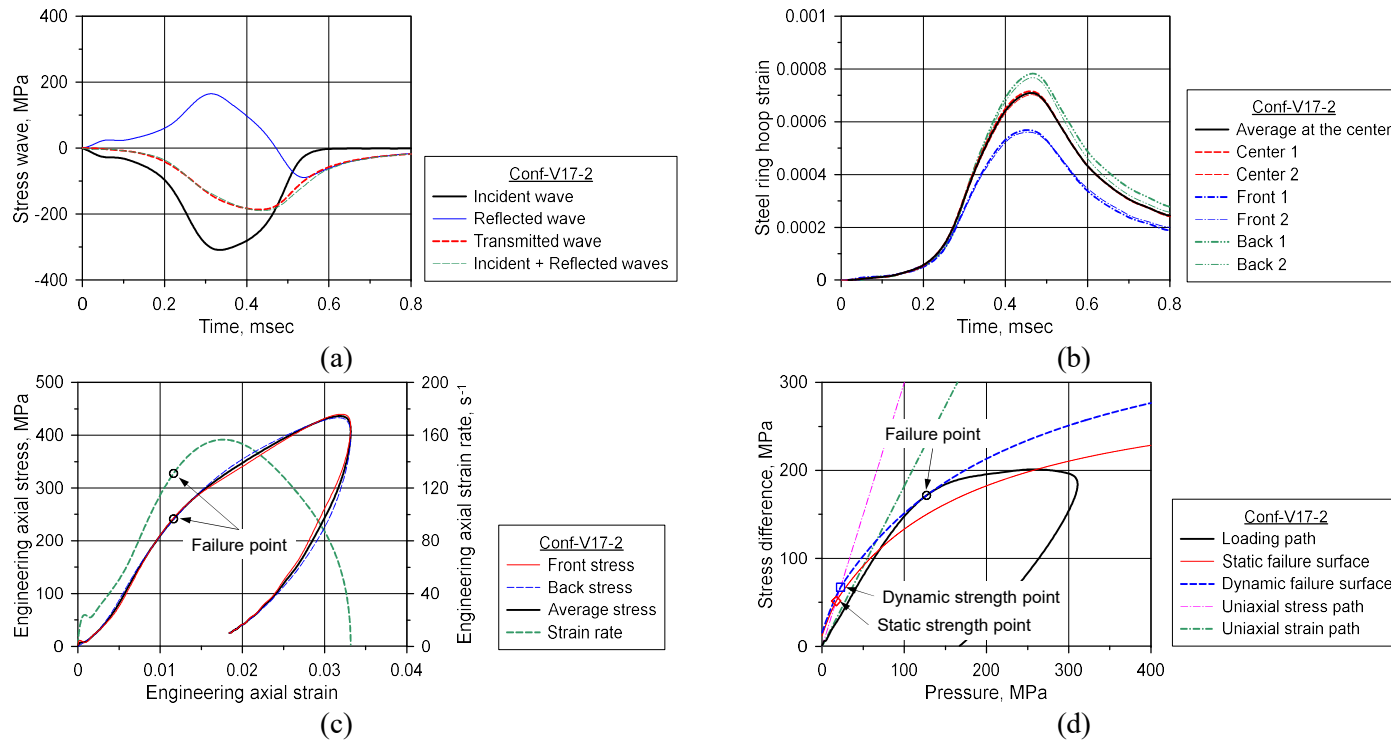


Figure B.25 Test results of Conf-V17-2; (a) Stress waves; (b) Circumferential strain of steel ring;
(c) Axial stress–strain curve; (d) Loading path and dynamic failure surface

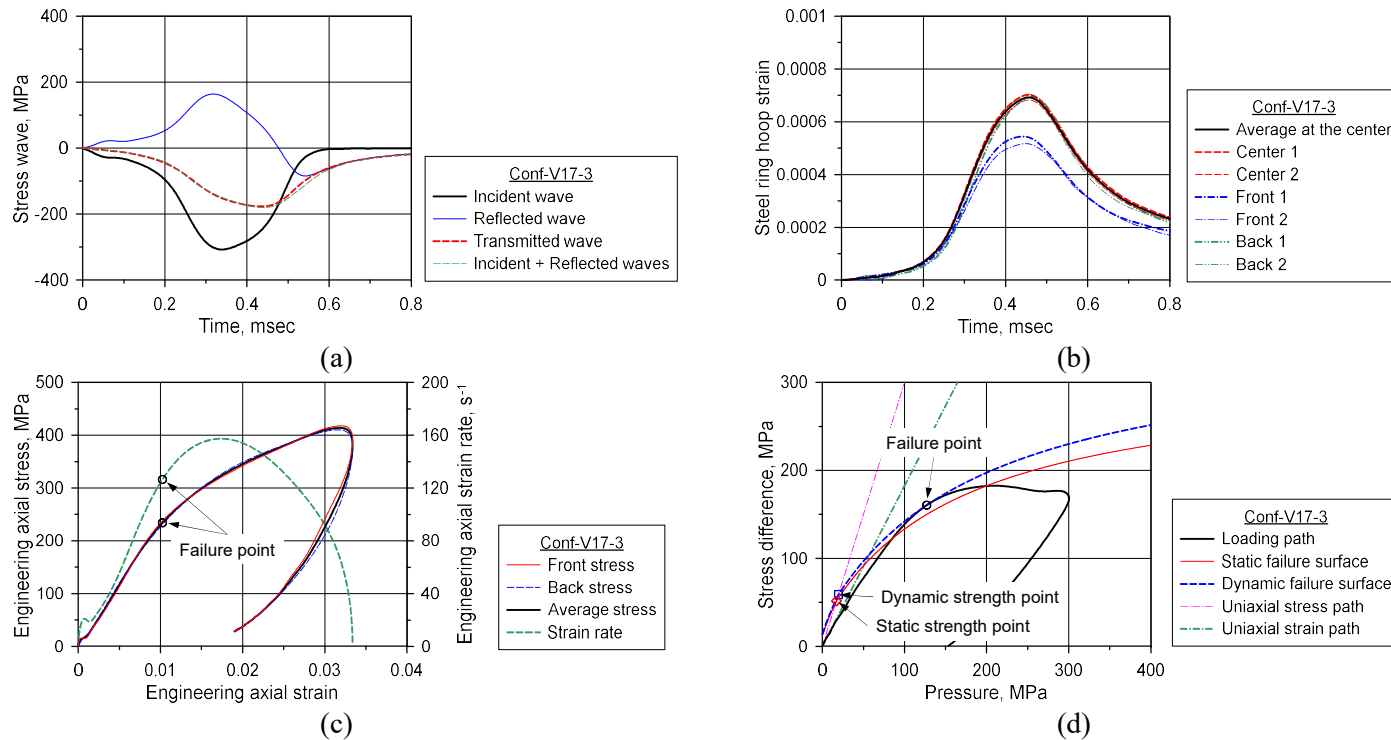


Figure B.26 Test results of Conf-V17-3; (a) Stress waves; (b) Circumferential strain of steel ring;
(c) Axial stress–strain curve; (d) Loading path and dynamic failure surface

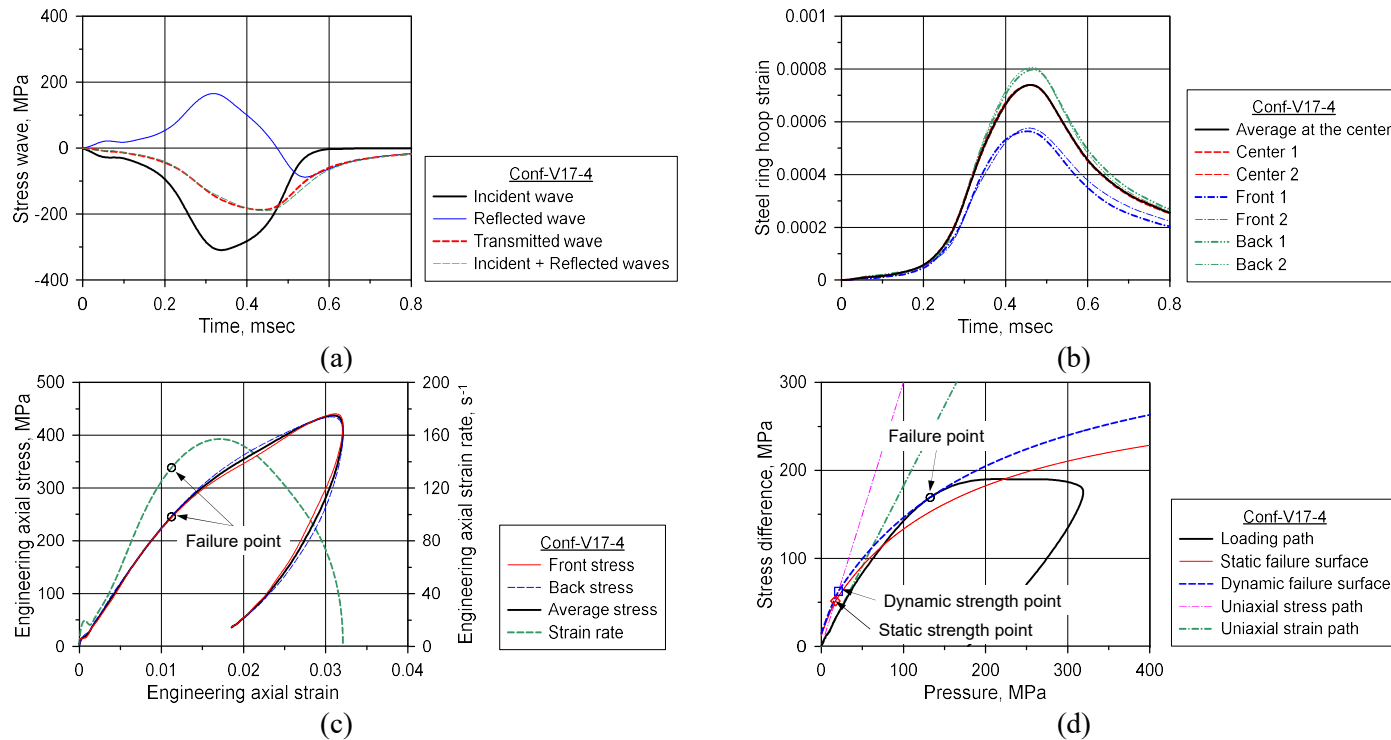


Figure B.27 Test results of Conf-V17-4; (a) Stress waves; (b) Circumferential strain of steel ring; (c) Axial stress–strain curve; (d) Loading path and dynamic failure surface

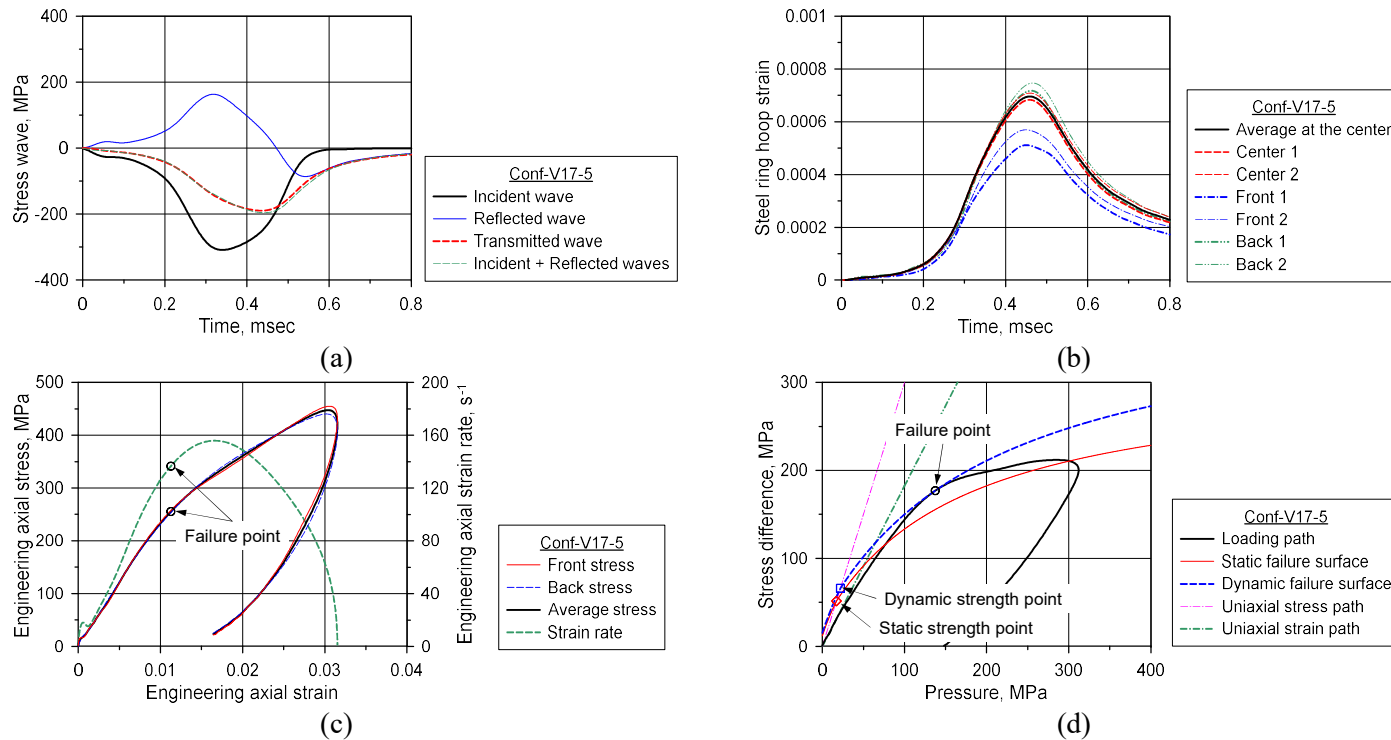


Figure B.28 Test results of Conf-V17-5; (a) Stress waves; (b) Circumferential strain of steel ring;
(c) Axial stress–strain curve; (d) Loading path and dynamic failure surface

국문초록

구속 Split Hopkinson Pressure Bar 실험에서의 콘크리트 압축강도에 대한 순수 변형속도 효과

이 상 호

높은 변형률 속도에서 콘크리트의 압축강도는 증진된다. 따라서 충돌 및 폭발하중과 같은 극한하중 하에서 콘크리트 구조물의 경제적인 설계 및 거동에 대한 정확한 평가를 위해서는 콘크리트의 동적압축특성을 적절히 고려해야 한다. 현재 콘크리트 압축강도에 대한 변형속도효과를 해석에 반영하기 위해 정적압축강도에 대한 동적압축강도의 비로 정의되는 동적증가계수가 활용되고 있으며, 콘크리트 압축강도에 대한 동적증가계수는 주로 split Hopkinson pressure bar (SHPB) 실험에 의해 조사되어 왔다.

그러나 SHPB 실험으로부터 획득한 동적증가계수를 유한요소해석에 적용하는 것에는 문제점이 있다. 바로 SHPB 실험에서 획득하는 변형률 속도 및 응력 정보가 불충분하다는 것이다. 전통적 SHPB 실험에서 시편에는 축방향 변형률 및 응력뿐만 아니라 푸아송 효과에 의한 횡방향 변형률 및 응력 또한 발생한다. 하지만 전통적 SHPB 실험에서는 오직 축방향 변형률 속도 및 응력만을 계측하고, 축방향 변형률 속도 및 겉보기

동적증가계수의 관계를 획득하게 된다. 반면에 대부분의 3 차원 유한요소해석에 사용되는 콘크리트 구성 모델에서는 유효 변형률 속도, 혹은 유효 편차 변형률 속도와 같이 여섯 방향의 변형률 속도 성분에 대한 함수로 동적증가계수를 고려하고 있으며, 동적증가계수 또한 일축응력상태를 기반으로 한 순수 변형속도 동적증가계수를 사용하고 있다. 결과적으로 전통적 SHPB 실험에서 획득한 겉보기 동적증가계수 및 축방향 변형률 속도 관계는 유한요소해석에 적용할 수 없으며, 유한요소해석을 위해서는 모든 변형률 속도 및 응력 성분에 대한 정보를 획득하여 유효 변형률 속도 및 순수 변형속도 동적증가계수의 관계를 획득해야 한다.

구속 SHPB 실험은 전통적 SHPB 실험의 문제를 해결하기 위한 대안이 될 수 있다. 구속 SHPB 실험은 재료의 다축응력상태에서의 동적특성을 조사하기 위한 실험기법으로, 구속 SHPB 실험에서는 모든 변형률 속도 및 응력 성분을 계측할 수 있다. 하지만 현재까지 구속 SHPB 실험을 통해 콘크리트의 순수 변형속도 동적증가계수가 연구된 사례는 거의 없으며, 순수 변형속도 동적증가계수를 획득하기 위한 방법론도 정립되지 않은 상황이다.

이 연구는 구속 SHPB 실험기법을 이용하여 순수 변형속도 효과에 의한 강도 증진을 평가할 수 있는 방법론을 제안하고 순수 변형속도 동적증가계수 모델을 개발하기 위해 일련의 수치해석 및 실험 연구를 수행하였다. 먼저 수치해석을 통해 횡구속을 받는 콘크리트의 동적압축거동에 대해 조사하였으며 이를 바탕으로 구속

SHPB 실험에서 순수 변형속도 동적증가계수를 획득하기 위한 방법론을 제안 및 검증하였다. 그리고 순수 변형속도 동적증가계수 데이터를 획득하기 위해 구속 SHPB 실험을 수행하였으며, 이와의 비교를 목적으로 전통적 SHPB 실험도 수행하였다. 전통적 SHPB 실험으로부터 획득한 겉보기 동적증가계수는 구속 SHPB 실험결과로부터 얻은 순수 변형속도 동적증가계수보다 높은 값을 나타내어 겉보기 동적증가계수를 극한하중을 받는 구조물의 설계 및 해석에 사용할 경우에는 비안전측 결과를 얻을 수 있음을 확인하였다. 그리고 구속 SHPB 실험 데이터에 대한 회귀분석을 수행하여 순수 변형속도 동적증가계수 모델을 제안하였다. 마지막으로 제안된 동적증가계수 모델을 검증 및 활용하기 위해 수치해석 연구를 수행하였다. 전통적 SHPB 실험 및 철근 콘크리트 보에 대한 자유낙하 충격실험에 대해 유한요소해석을 수행하였으며, 콘크리트 압축강도에 대한 동적증가계수가 해석 변수로 고려되었다. 해석결과는 이 연구의 순수 변형속도 동적증가계수를 적용한 유한요소해석이 콘크리트의 동적압축거동 및 콘크리트 구조물의 충격거동을 적절히 예측할 수 있음을 나타냈으며, 이로부터 제안된 순수 변형속도 동적증가계수 모델이 타당함을 확인하였다.

주요어: 동적증가계수, 변형속도 효과, 관성효과, 일축 변형률 상태, split Hopkinson pressure bar, 콘크리트 동적압축강도

학번: 2017-39671